THE UNIVERSITY OF CHICAGO

STUDY OF VACUUM RF BREAKDOWN IN STRONG MAGNETIC FIELDS

A DISSERTATION SUBMITTED TO
THE FACULTY OF THE DIVISION OF THE PHYSICAL SCIENCES
IN CANDIDACY FOR THE DEGREE OF
DOCTOR OF PHILOSOPHY

DEPARTMENT OF PHYSICS

BY
ALEXEY KOCHEMIROVSKIY

CHICAGO, ILLINOIS
AUGUST 2018

TABLE OF CONTENTS

LIST OF FIGURES

LIST OF TABLES

ACKNOWLEDGMENTS

I would like to acknowledge the help from many people who supported my research.

- Professor Young-Kee Kim, my academic advisor, for her support over my research projects and guidance in my academic life.
- Professor Yagmur Torun, the head of the MTA program, who's tremendous efforts enabled the experimental work this thesis is based on.
- Dr. Daniel Bowring, my research advisor at Fermilab, for his guidance and help with structuring this thesis.
- Dr. Mark Palmer and Dr. Peter Garbincius, Heads of the Muon Accelerator Program collaboration that supported this research and my professional development.
- Dr. Diktys Stratakis, Professor Yagmur Torun, Dr. Katsuya Yonehara and Dr. Alvin Tollestrup for the fruitful scientific discussions and valuable advice they provided over the course of my PhD program.
- Alan Bross, Ben Freemire, Ao Liu, Tianhuan Luo, Al Moretti, Dave Neuffer, Michael Backfish, Katsuya Yonehara, Yagmur Torun, Daniel Bowring, Terry Hart, Milorad Popovic for their help with taking experimental shifts on the Modular Cavity's high power runs.
- My wife Anna for her stoic support of my academic pursuits.
- My close friend and colleague Ilya Ivanov for his unquenchable optimism and long-standing moral support.

ABSTRACT

Muon accelerators have a potential to open new paths for advancing particle physics both in intensity and energy frontier. Short lifetime of muons requires the implementation of ionization cooling. Most contemporary designs of muon ionization cooling channels require high-performing normal-conducting RF cavities in external multi-tesla solenoidal magnetic fields. One of the limitations of evacuated cavities' performance is RF breakdown. It was experimentally shown that the presence of external magnetic field increases breakdown rate at a given gradient. Pulsed heating model of RF breakdown aims to explain the deterioration of cavity gradients in strong focusing magnetic fields. The model proposes that cyclic fatigue leads to the metal surface degradation and eventual breakdown. The cyclic fatigue is caused by the periodic bombardment of inner surfaces of the cavity by dark current electrons, emitted from local surface imperfections and focused by external magnetic field.

An 805 MHz pillbox cavity was designed to study the effect of external magnetic field on RF breakdown. Special "modular" design of the cavity allowed for control over sources of systematic error and frequent turnaround times for surface inspections. Frequent inner surface inspections are essential for the breakdown damage tracking and understanding the effect of different materials on RF breakdown. In this work I will discuss the results of high power tests of the Modular Cavity with copper and beryllium walls in the range of magnetic fields. Measured gradient performance is tested against predictions of pulsed heating model, modified for experimental conditions of the Modular Cavity.

CHAPTER 1

INTRODUCTION

1.1 Particle accelerators and colliders

Particle physics seeks to understand the most fundamental laws that govern energy and matter. To move forward, advances in the energy and intensity frontiers are essential. The majority of modern high-energy physics experiments use particle colliders as experimental platforms for research. Particle colliders are complex machines that use electromagnetic fields to accelerate, focus and guide the beam of particles to the collision location. Detectors around collision point are used to characterize the products of beam collision. Some of the colliders reach center of mass energy of TeV scale which opens paths to probing nature for new physics in particle interaction and fundamental laws of particle behavior.

1.2 Muon collider and neutrino factory

Muon accelerators aim to address some of the outstanding questions in modern high energy physics. Modern accelerators can be categorized as either hadron accelerators or lepton accelerators. Because muons are 200 times heavier than electrons, the muon's rest mass $m_u = 106$ MeV allows it to couple to the Higgs boson via the s-channel in Standard Model formalism [1]. This opens an opportunity for precision measurements of production and decay properties of the Higgs boson [2]. At the same time, the heavier mass of the muon also means orders of magnitude lower synchrotron radiation when accelerated in a curved trajectory. This can be seen from the formula for synchrotron radiation power loss for the charged particle moving in external magnetic field in Equation 1.1 [3]. Note that $\frac{P_e}{P_\mu} \propto \left(\frac{m_\mu}{m_e}\right)^4 = 1.9 \times 10^9$, means proportionally larger synchrotron radiation loss for electron beams compared to muon beams.

$$P = \frac{1}{6\pi\epsilon_0}\frac{e^4}{m^4c^5}B^2K^2, \tag{1.1}$$

where ϵ_0 is the permittivity of free space, e is electron charge, m is the mass of the particle, K is the particle's kinetic energy, c is the speed of light, and B is the external magnetic field.

Lower radiation loss by muons allows to increase the curvature of their quasi-circular trajectory by increasing the strength of bending magnetic field B. This advantage creates a possibility of building a circular muon accelerator on site of existing laboratories, i.e. Fermilab. Figure 1.1 illustrates one proposal for Neutrino Factory and Muon Collider facilities on the Fermilab site. The characteristic size of the whole accelerator complex is 5 km. Thus, a muon accelerator offers a significant reduction in size compared to designs of other next generation high energy colliders, such as CLIC, FCC and ILS [5, 6, 7]. For example, the planned length of accelerating channel in Compact Linear Collider (CLIC) is 42 km.

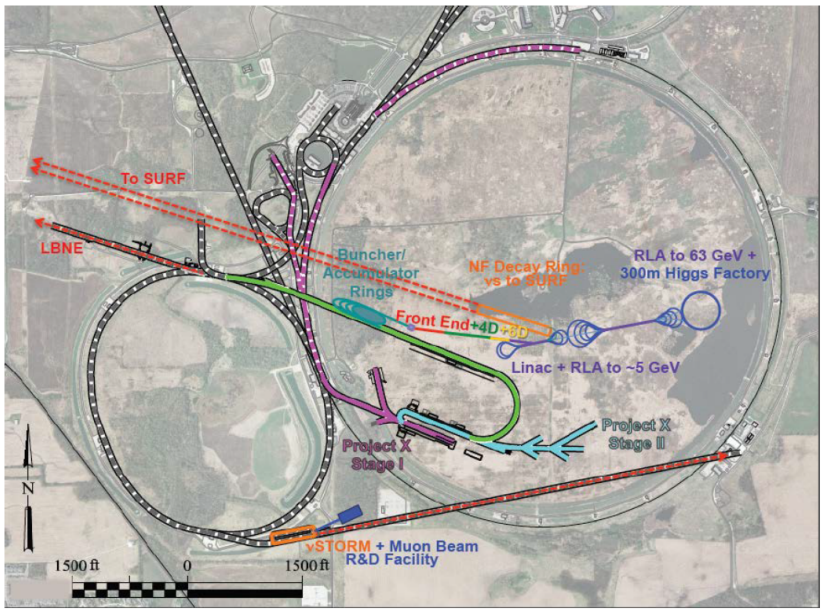

Figure 1.1: Possible layout of Neutrino factory and Muon Collider at Fermilab site [4].

Muon accelerators could also explore the physics of neutrino sector. A high-intensity neutrino beam can be produced from the decay of stored muons in a circular collider. A so-called "neutrino factory" is capable of creating a beam of well-defined properties and

low hadronic uncertainties in the energy spectrum [8]. This opens doors to high sensitivity studies of neutrino CP parity violation, the mass hierarchy problem and unitarity [9].

The muon, has a relatively short lifespan of 2.2 microseconds, compared to other typically accelerated particles. This makes muons more challenging to accelerate to high energies while simultaneously keeping the beam focused. Additionally, in the contemporary designs of muon collider and neutrino factory, muons are produced by the pion decay and have a large phase emittance ϵ. Beam emittance is defined as a beam spread in momentum-coordinate phase space. In order to fit the beam into an aperture of a typical accelerating channel, it is necessary to reduce the transverse size of the beam by several orders of magnitude. Similarly, muons must longitudinally fit in RF time bucket for proper acceleration. Most of the beam cooling methods that have been developed for electrons and protons are suitable for stable particles only. Standard cooling methods used in accelerator physics are stochastic cooling, laser cooling, synchrotron cooling and electron cooling. Below I will provide a short description of each method together with its limitations in the context of muon beam cooling.

- *Stochastic cooling* uses a feedback loop from beam position monitors to correct the motion of individual particles or groups of particles by introducing an additional voltage kick in the transverse direction [10]. Typically, these transverse corrections are applied for at least several seconds, corresponding to millions of beam periods in a ring, which makes the technique implementation challenging for short-lived muons. Another problem arises due to the strict emittance requirements of muon cooling channel designs, for which thermal noise becomes a significant limiting factor [11].

- *Laser cooling* uses the electromagnetic flat wave to excite ions [12]. The cooling is achieved by momentum loss of the ion emitting extra energy in the form of a photon. Laser cooling techniques are usually limited to ion beams.

- *Synchrotron radiation cooling* uses the synchrotron radiation of the moving particle to reduce transverse and longitudinal momentum spread. Due to earlier discussed mass

term in the power loss Equation 1.1, synchrotron radiation is most effective for light particles such as electrons and positrons.

- *Electron cooling* is implemented by injecting an electron beam parallel to the main beam of heavy particles [13]. It was shown that if velocities of two beams are closely matched, the temperatures of both systems in a common frame of reference reach equilibrium. As a result, the transverse motion in the heavy particle beam decreases. Typical cooling times exceed seconds, making this technique challenging for muon cooling. Additional limitations to this technique stem from required high electron density and emittance parameters of primary beam.

The short lifetime of muon and strict limitations imposed on the emittance reduction of the muon beam requires the development of a conceptually new approach to muon beam cooling. Ionization cooling is the only viable solution to the problem at this point.

1.3 Muon Ionization Cooling

Muon ionization cooling, first proposed in 1981, achieves cooling by introducing energy dissipative mechanism through particle ionization in medium, leading to ionization momentum loss [15]. The transverse phase volume of the muon beam is reduced by passing the beam through an absorber-RF cavity system. Muons lose both transverse and longitudinal momentum when they pass an absorber. The longitudinal component is then restored via an accelerating RF cavity. The net effect of passing the "absorber - RF cavity" system is a reduction of transverse emittance. To keep the beam contained and focused, both absorbers and RF cavities ought to be placed inside the solenoidal magnetic field [16]. Solenoidal fields as high as 20 tesla were considered for the end portion of vacuum cooling channel [17]. Figure 1.2 shows a conceptual diagram of the absorber-cavity system.

Transverse emittance reduction can be described by the following formula [18]:

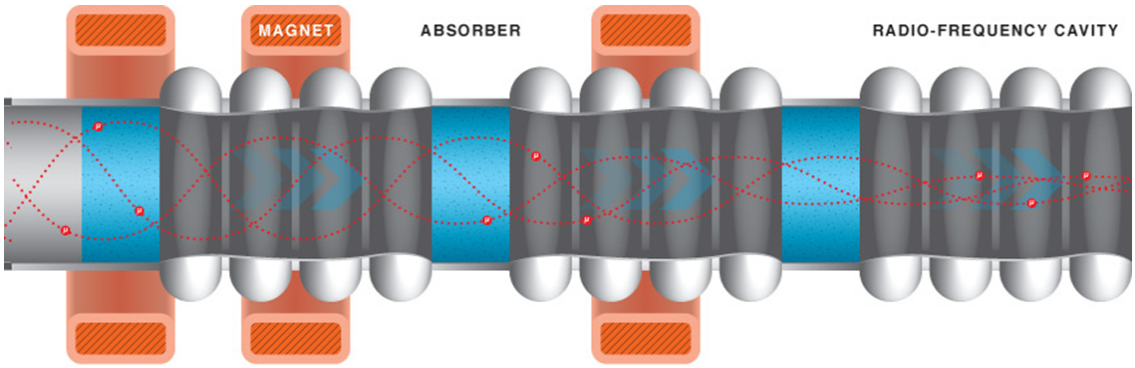

Figure 1.2: Conceptual diagram of the ionization cooling concept [14]. As the beam passes the RF cavity - absorber system, its transverse emittance is being reduced while longitudinal momentum is preserved.

$$\frac{d\varepsilon_\perp}{dz} = -\frac{d\varepsilon_\perp}{\beta^2 E}\frac{dE}{dx} + \frac{\beta_\perp K^2}{2\beta^3 L E m_\mu} \tag{1.2}$$

where $\varepsilon_\perp$ is the transverse emittance of the beam, $\beta_\perp$ is the betatron function calculated at the center of absorber, L is the radiation length of the material used in absorber, $\beta = \frac{v}{c}$ is the relativistic muon speed, E is energy of the muon and m_μ is the muon mass. The first term on the right hand side of the Equation 1.2 corresponds to ionization energy loss that leads to cooling; the second describes the multiple scattering that leads to the heating of the beam. Equilibrium emittance is achieved when heating and cooling terms cancel out, making net cooling effect zero. This imposes a hard limit on the maximum achievable cooling in given lattice. To minimize the equilibrium emittance, the heating effect needs to be minimized. In practical terms, it could be achieved by adjusting accelerator parameters to reduce β and choosing an absorber material with the largest L. To include longitudinal cooling, a reduction of longitudinal emittance is necessary. In practical designs this can be achieved through the mechanism of emittance exchange, in which the beam's longitudinal size is decreased by increasing its transverse dimensions, a more manageable task. One way of facilitating this mechanism is to use a dipole magnet that bends the beam so that the higher energy muons' trajectory has a longer path through the absorber. This creates a correlation

between momentum and the position within the beam. Passing such beam through a wedge shaped absorber leads to higher energy muons traversing a longer absorbing distance in the thick part of the material. Therefore, higher energy particles lose more energy, effectively decreasing the energy spread. However, the transverse size of the beam increases as a result. Implementation of this mechanism is demonstrated in Figure 1.3.

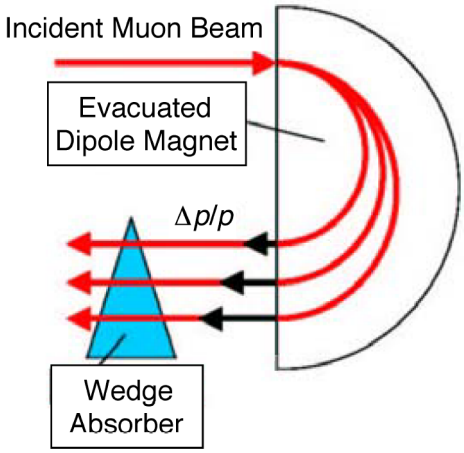

Figure 1.3: Emittance exchange mechanism: compact beam with longitudinal momentum spread passes through dipole magnet, creating dispersion in transverse position. The spread in transverse coordinate is converted to spread in longitudinal momentum as the beam passes through the wedge-shaped absorber [19].

The international Muon Ionization Cooling Experiment (MICE) at RAL is designed to demonstrate the proof-of-concept muon ionization cooling and establish the feasibility of building full-scale muon accelerators [20].

1.4 Muon acceleration - R&D efforts

Significant progress in advancing the technologies for building muon collider and neutrino factory has been made. The Muon Accelerator Program (MAP) was established in 2010 as a unified effort in the U.S. for technological development required for building Muon Collider and Neutrino Factory [21]. Figure 1.4 shows conceptual block diagrams of Neutrino Factory and Muon Collider [22].

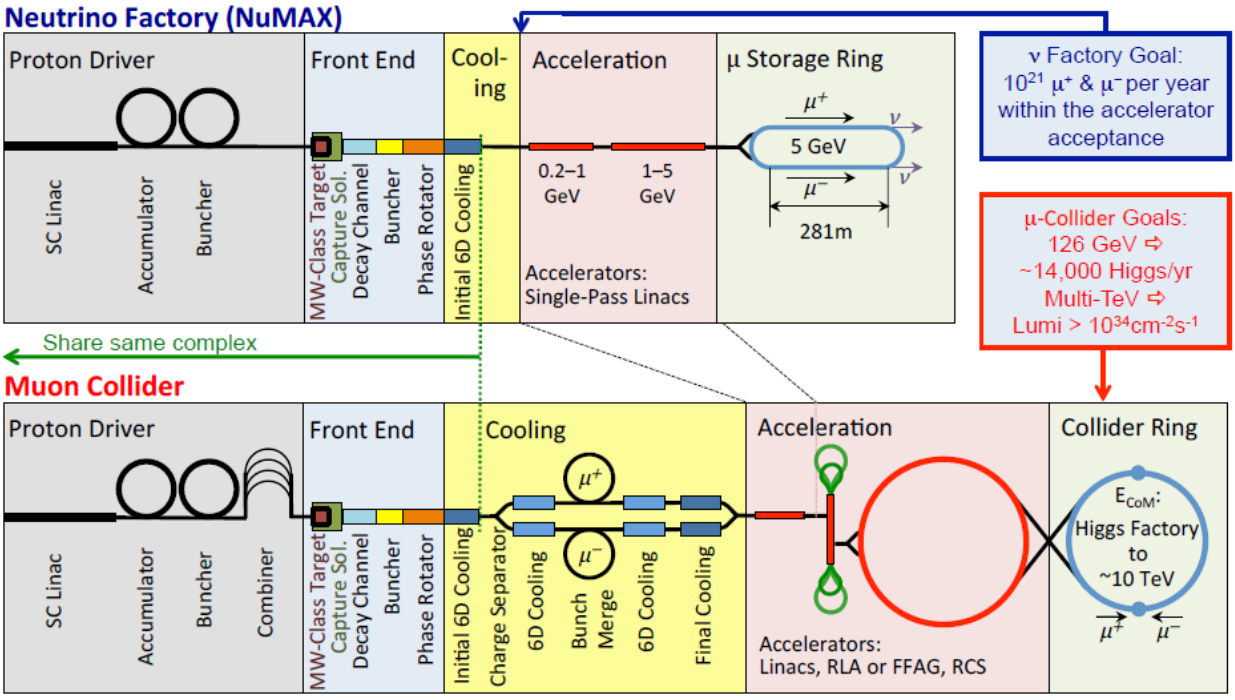

Figure 1.4: Schematic block diagram for conceptual designs of Neutrino Factory and Muon Collider [22].

Both designs incorporate common stages of the accelerating complex:

- *The proton driver* consists of superconducting Linac, Accumulator and Buncher to deliver an intense proton beam to the target for pion production.

- *The Front End* portion is responsible for creating high-intensity muon beam from pion decay, produced in the decay channel after the proton-target collision.

- *The Cooling* stage provides contained high brightness muon beam delivery to the final stages of the machine. It uses ionization cooling mechanism to reduce the beam emittance by a factor of $\sim 10^6$ and also includes the bunch merging section.

- *Muon Acceleration* is required to achieve high energies of the muon beams to provide physics at the relevant collider energies. This stage may include different accelerating sub-stages such as linear accelerator, recirculating linac or accelerating synchrotrons [23].

- *Storage rings* fulfill two different functions. Decay rings store decaying muons, providing intense, pure neutrino beams in a neutrino factory. Collider rings provide high luminosity muon collision at the TeV energy scale. The TeV-energy muon bunches are accumulated in the rings, increasing the number of colliding particles in a single collision event.

A high-brightness muon beam produced in the first two stages of the accelerator requires strong cooling. Figure 1.5 shows the simulated evolution of the transverse and longitudinal emittance of the beam in the designs of the ionization cooling stages [24]. The resulting beam must be acceptable for Neutrino physics applications. Therefore, ionization cooling stages are designed to reduce both space charge limited longitudinal emittance and transverse emittance. A final cooling stage would perform the emittance exchange between transverse and longitudinal component to achieve the required beam parameters for a multi-TeV collider operation with target luminosity of $10^{34} - 10^{35}\ cm^{-2}s^{-1}$ [22].

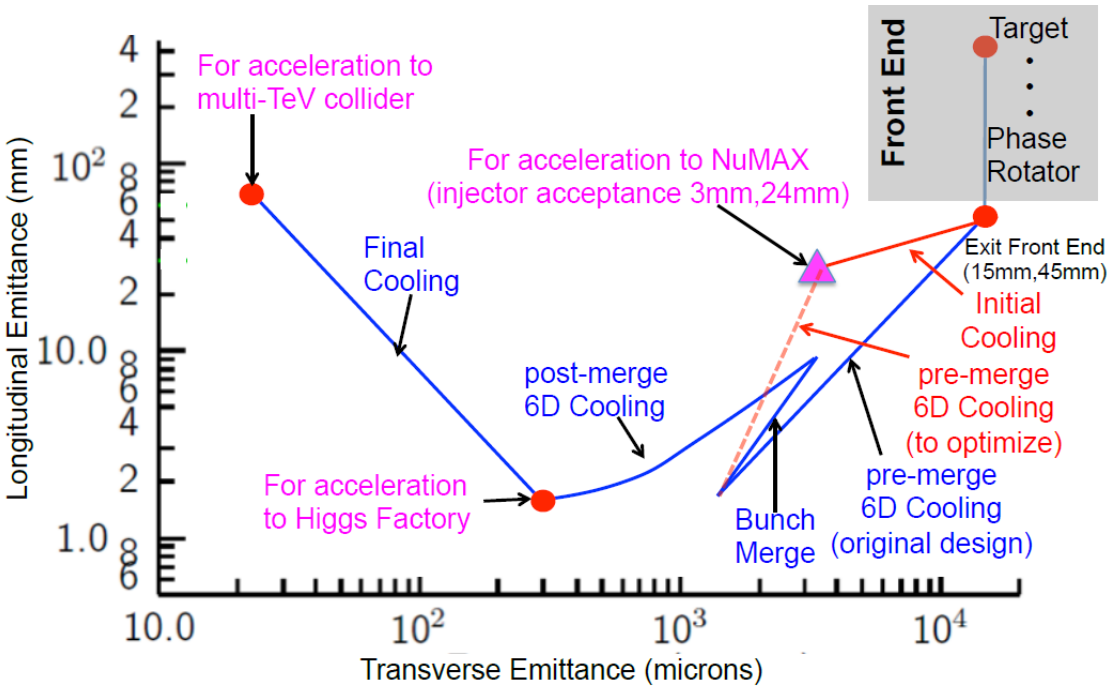

Figure 1.5: Simulated evolution of muon beam emittance for the muon accelerator program [22].

Each stage of the accelerator has R&D, technological and implementation challenges. The

most relevant for the purpose of this thesis is the requirement for RF cavity performance in the cooling stage. In particular, normal conducting RF cavities in the hundreds MHz frequency range must operate at high accelerating gradients in solenoidal magnetic fields of several tesla.

1.5 Problem of RF breakdown in accelerating cavities

1.5.1 Introduction to RF cavities

Early particle accelerators used electrostatic capacitors to achieve the high voltages needed for efficient beam acceleration. The Cockcroft-Walton accelerator is an example of such a machine [25]. Voltage multiplier construction consisted of high voltage transformer, diods and capacitors. However, the excessive static electric fields at the surface put a limit on the maximum achievable voltage. For open-air machines, the electric field must not exceed 3 MV/m to avoid spontaneous arc discharges, or DC breakdown.

Oscillating electric fields can be used instead of electrostatic potentials to overcome this limitation. The first RF linear accelerator was built by Wideroe in 1928 [26]. Since then, significant progress has been made in designing RF resonators, using both normal-conducting and super-conducting materials. The range of operating frequencies of RF cavities also varies significantly depending on the application, from tens of MHz to multi-GHz. RF cavities can be classified as standing wave structures and traveling wave structures. In standing wave cavities, incident and reflected electromagnetic waves create a stationary pattern where amplitude of the wave at a given point varies with time, but its phase is constant. This thesis considers normal-conducting standing-wave RF cavities with frequency of 805 MHz.

Essentially, an RF (also sometimes referred to as "microwave") cavity is a metallic structure capable of sustaining resonant electromagnetic modes in its interior volume. An RF cavity operating at a certain resonance mode can be modeled by an LRC circuit with very high quality factor, typically in the range of $10^4 - 10^5$ for normal conducting and $10^8 - 10^9$

for superconducting cavities. The electric field inside the cavity is oscillating and, when operated in an accelerator, is timed to give an appropriate momentum gain to the passing beam. Similar to electric field but with a $\pi/2$ phase shift, an oscillating magnetic field causes deflection to the passing particles but no acceleration.

1.5.2 Standing wave pillbox cavity

One of the simplest forms of resonant cavity is a cylindrical "pillbox" cavity. Its cylindrical shape admits simple closed-form solutions for the electromagnetic field inside the cavity volume. Figure 1.6 shows the schematic representation of the pillbox cavity of inner radius R and RF gap length L. This Section largely follows the formalism in [27]. Assuming that cavity is made of a perfect conductor, the electric field $\vec{E}$ and magnetic induction $\vec{H}$ must satisfy the boundary conditions:

$$\begin{aligned} \vec{n} \cdot \vec{H} &= 0 \\ \vec{n} \times \vec{E} &= 0, \end{aligned} \tag{1.3}$$

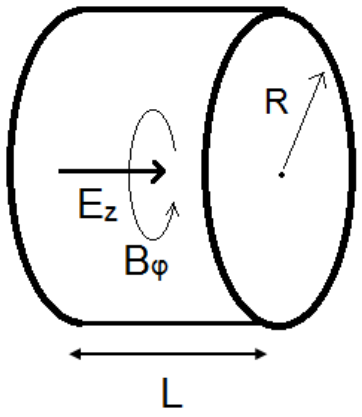

Figure 1.6: Schematic representation of the cylindrical "pillbox" cavity of inner radius R and RF gap length L, operating at resonant TM_{010} mode.

where $\vec{n}$ is the unit vector perpendicular to the conducting surface. Additionally, both fields must satisfy the electromagnetic wave equations:

$$\nabla^2 \vec{E} - \frac{1}{c^2}\frac{\partial^2 \vec{E}}{\partial t^2} = 0$$
$$\nabla^2 \vec{H} - \frac{1}{c^2}\frac{\partial^2 \vec{H}}{\partial t^2} = 0, \tag{1.4}$$

where c is the speed of light and the chosen unit system sets vacuum permeability to be unity. Two different families of solutions for Equation 1.4 exist. The *transverse electric* (TE) modes have a longitudinal component H_z and transverse component E_t that are non-zero, while $H_t = E_z = 0$. The *transverse magnetic* (TM) modes have non-zero longitudinal component E_z and transverse component H_t, while $H_z = E_t = 0$. For the cylindrical pillbox cavity of length L and radius R, the lowest-frequency TM mode solutions for Equation 1.4 take form [27]:

$$E_z = E_o \ J_o(\frac{2.405r}{R}) \ e^{-i\omega t}$$
$$H_\phi = -i\frac{E_0}{\eta} \ J_1(\frac{2.405r}{R}) \ e^{-i\omega t} \tag{1.5}$$

, where J_0 and J_1 are the zero- and first-order Bessel functions and $\eta = 377\ \Omega$ is the impedance of free space. The resonant frequency of the fundamental TM_{010} mode is derived from the boundary conditions in Equation 1.3.

$$\omega = \frac{2.405c}{R} \tag{1.6}$$

satisfies the requirement $H_\phi(r = R) = 0$. The lowest frequency TM mode is often referred to as the fundamental TM_{010} mode of the pillbox cavity. Figure 1.7 shows the vector field pattern of electric and magnetic fields inside the cavity volume. The longitudinal axis of the cavity becomes a convenient avenue for beam acceleration, as longitudinal magnetic and transverse electric field components are always zero in TM modes. Additionally, the longitudinal electric field is maximized in the center providing the most efficient acceleration, while transverse particle deflection due to the magnetic field is minimized. TE modes, on the other hand, have no longitudinal electric field component and therefore are of little interest

for the purposes of beam acceleration.

For a real accelerating cavity, the pillbox geometry needs to be modified to allow a for beam pipe and power input. Disturbed ideal pillbox geometry makes it impossible to calculate fields inside the cavity analytically. Commonly, numerical solving algorithms an computer codes are used to simulate accurate field distributions.

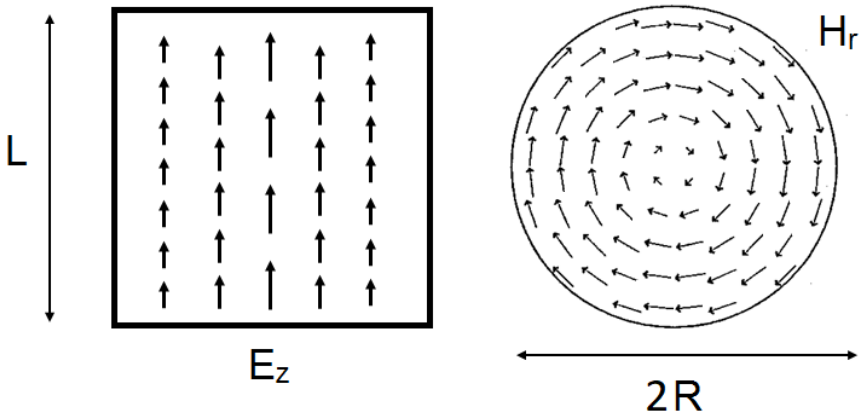

Figure 1.7: Vector plots of electric (left) and magnetic (right) fields in the pillbox cavity for fundamental TM_{010} mode. Left - longitudinal E_z component in the r-z plane, right - radial magnetic component H_r in the perpendicular plane.

The electromagnetic energy density in the cavity volume can be calculated as:

$$w = \frac{1}{2}[\epsilon_0 E(r,t)^2 + \frac{1}{\mu_0} B(r,t)^2] \tag{1.7}$$

where the full time-dependent fields can be expressed as

$$\begin{aligned} E(r,t) &= E(r)\cos(\omega t) \\ B(r,t) &= B(r)\sin(\omega t). \end{aligned} \tag{1.8}$$

Given the radial symmetry of the field solutions, the total stored energy can be calculated by integrating the field density over the whole cavity volume at $t = 0$ as

$$U = \int_0^L \int_0^R 2\pi r \; E^2(r) \; dz \; dr = \frac{L}{\mu_0} \int_0^R 2\pi r \; B^2(r) \; dr \tag{1.9}$$

Now, using Equation 1.5 one can find the expression for the stored energy in an ideal pillbox cavity operated at TM_{010} mode:

$$U = A_1 \ \frac{\pi R^2 \ L}{2\mu_0 c^2} \ E_0^2 \tag{1.10}$$

where $A_1 = J_1^2(2.405) \simeq 0.269$ and $\mu_0 = 4\pi \times 10^{-7}$ H/m is the permeability of vacuum.

So far the discussion in this section was applied to the case of *perfect* pillbox cavity, assuming perfectly conducting wall material. In reality, of course, metal has a finite resistance at a given RF frequency and wall currents result in dissipated energy in the form of heat. These Joule heating losses can be quantified:

$$p_s = \frac{1}{2}\sigma_s H^2(r,t) \tag{1.11}$$

where p_s is the dissipated power per unit area ds and σ_s is the sheet resistance of material. Typically, the value of sheet resistance for commonly used metals is in milliohm range. Because σ_s is so small, perturbation to the fields by the lossy material can be neglected.

For the TM_{010} mode the total power loss in cavity walls can be calculated as a sum of power dissipation in flat endplates and cylindrical body. Endplate is defined as a flat cylindrical wall of the pillbox cavity. Combining Equations 1.5 and 1.11 gives:

$$P_{loss} = \frac{\sigma_s E_0^2}{\eta^2} \ \left(\int_0^R 2\pi r \ J_1^2(\frac{2.405r}{R}) \ dr + A_1 \pi R L \right) \tag{1.12}$$

where the integral part of the equation represents the total loss in the cavity walls and the second term is power loss in the cylindrical body. The total power loss in the cavity with on-axis gradient E_0 takes the following form for the TM_{010} mode:

$$P_{loss} = \frac{A_1}{\eta^2} \ \sigma_s E_0^2 R(R+L) \tag{1.13}$$

A common figure of merit for accelerating cavities is the *quality factor*, defined as the

ratio of energy stored in a cavity volume to the energy lost per RF cycle:

$$Q_0 = \frac{\omega_0 U}{P} \tag{1.14}$$

where P is the total power dissipated by the cavity walls and ω_0 is the resonant frequency. Typical quality factors for normal conducting cavities are on the order of $10^4 - 10^5$. The closed-form equation for the quality factor of ideal pillbox cavity then becomes:

$$Q_0 = \frac{\epsilon_0 L R \eta^2}{2\sigma_s (R + L)} \tag{1.15}$$

Another commonly used figure of merit is called *geometry constant* or *geometry factor*:

$$G = \frac{\omega_0 \mu_0 \int_V H^2 \, dv}{\sigma_s \int_S H^2 \, ds} \tag{1.16}$$

The geometry factor is a useful quantity as it depends only on the cavity shape and does not depend on its absolute dimensions, making it easier to compare cavity structures irrespective of their size. For ideal pillbox cavity, the expression for geometry factor takes the form 1.17.

$$G = \frac{2.405 \; \eta \; \frac{L}{R}}{2(1 + \frac{L}{R})} \tag{1.17}$$

Another figure of merit often used to characterize RF cavities is *shunt impedance*. In accelerator physics shunt impedance is defined as:

$$R = \frac{V^2}{P_{loss}} \tag{1.18}$$

where V is the peak voltage drop across the cavity gap. Combining results from Equation 1.13 for TM_{010} mode in pillbox cavity, the expression for the shunt impedance becomes:

$$R = \frac{4 \; \eta^2 L^2}{A_1^2 \pi^2 \sigma_s R (R + L)} \tag{1.19}$$

Shunt impedance characterizes Joule heating losses in a cavity. In real accelerating structures it is favorable to maximize R so that the dissipated power is minimal.

Accelerating gradient of the RF cavity is defined as the maximum electric field E on the beam axis. In the case of pillbox cavity, accelerating gradient is just the electric field strength on its longitudinal axis.

1.5.3 Phenomenology of RF Breakdown

RF breakdown is a serious problem in the development and operation of RF structures for modern particle accelerators. The major issues arising from RF breakdown are limitation on the cavity's gradient performance and infliction of surface damage. RF breakdown can be defined as a spark inside the structure that abruptly shorts the cavity's electromagnetic field. The spark dissipates stored energy in the form of heat, radiation, and light, causing local melting on the surface and a spike in vacuum pressure. The energy released also varies greatly with the type of structure and stored energy in the resonator right before breakdown initiation. Generally, RF breakdown is accompanied by bursts of visible light, electron current emission, and radiation (mostly X-rays), increased vacuum activity, and distortion in RF transmitted and reflected power signals compared to normal operation. Figure 1.8 demonstrates an example of two typical RF pulses, one for a normal RF pulse and another for a pulse that triggers breakdown. Breakdowns are typically observed in areas of a cavity with strong surface electric fields. Breakdown-caused damage takes the form of melted material, often in the form of a crater or Lichtenberg figure [28].

The duration of breakdown events can vary from nanoseconds to microseconds, depending on the set of operating parameters. Among these parameters are resonant frequency of the structure, input RF power value, RF pulse length, geometry of the cavity, material and general conditions of the critical surfaces exposed to a high surface electric and magnetic field, vacuum pressure, operating temperature etc.

The range of magnitudes of these parameters and varying operating conditions make

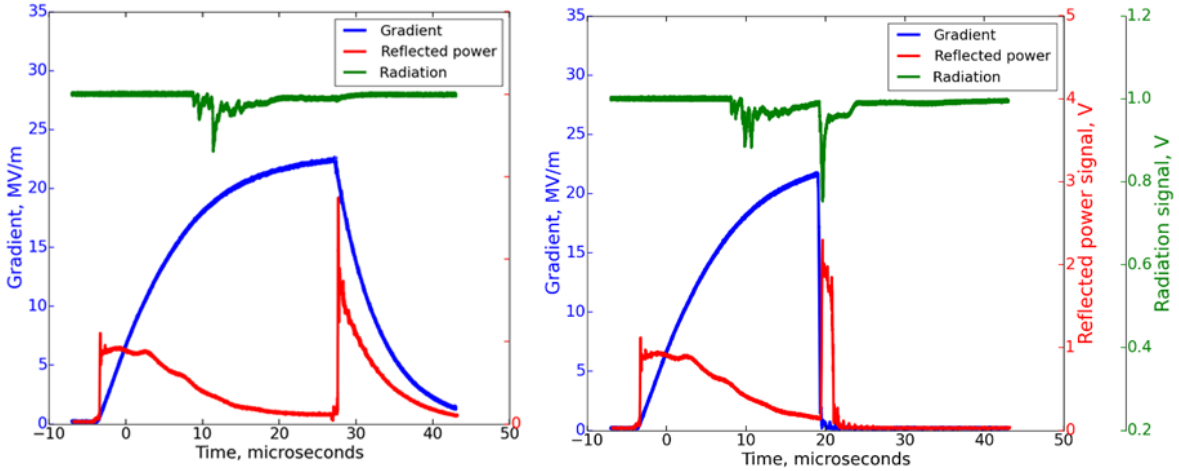

Figure 1.8: Envelope of pickup signal (blue), NaI radiation detector (green), reflected power (red) for normal event (left) and breakdown event (right). Note that decay time constant of the gradient (traced by pickup signal) is several times shorter for breakdown event.

the phenomenon of RF breakdown hard to study. In particular, short timescales and MW-scale power RF conditions make it very challenging to instrument comprehensive diagnostic systems on a microscopic level. Macroscopic studies of RF breakdown were performed extensively [29, 30, 31].

Another reason why RF breakdown is a challenging phenomenon to study is the mix of disciplines it touches upon: material science, surface effects, plasma physics, crystallography, molecular dynamics etc. are all relevant for understanding the full picture of breakdown physics. In this dissertation I will be discussing the RF breakdown in vacuum, i.e. the gaseous mean free collision path for electrons is greater than the characteristic dimensions of the resonator.

1.5.4 Common wisdom in the RF breakdown community

Several attempts have been made to consolidate breakdown observations into one comprehensive model. These models of RF breakdown can be classified by initiation mechanism. Mechanisms can be grouped as [32]:

- *Cathode models*, in which RF breakdown is triggered by the cathodic field emission

from microscopic protrusions on the surface [33, 34, 35]. It is important to note that in oscillating an RF electric field, the cathode and the anode reverse every RF cycle. Usually, the surface that emits electrons is referred to as the cathode while the surface that gets impacted by electrons is referred to as the anode.

- *Exchange models* that are based on the secondary emission of electrons and motion of ions between two electrodes [36]. Electrons emitted from the cathode are impacting on the anode, causing secondary electron emission. These electrons are in turn can be accelerated in the RF fields and impact on the anode surface creating the feedback loop between the anode and the cathode.

- *Anode models* that are based on ionization processes developing near anodes bombarded by electron currents coming from cathode [37].

There is no one commonly accepted theory describing all breakdown stages. However, there is a set of universally accepted observations about breakdown phenomena:

- *RF breakdown is preceded by increased dark current emission.* Dark current is the process of electron emission inside the cavity volume from the inner surfaces. X-ray radiation measurements and direct current measurements showed the presence of electron current in the accelerating gap of the cavity with no beam present [38, 39, 40]. Directly before the breakdown, dark current density increases sharply, which testifies to the crucial role that dark current electrons play in the process of breakdown triggering.

  There is a disagreement in the nature of dark current sources. Most models consider needle-like, microscopic surface protrusions that create an enhanced electric field region at the tip and can also potentially lower the work function of metal locally, facilitating stronger electron emission. The average field-emitted current density J_c can be calculated from the Fowler-Nordheim formula modified for the RF case [66]:

$$J_c = 5.7 \times 10^{-16} \ \frac{10^{4.52} \cdot \phi^{0.5}}{\phi^{1.75}} \ (\beta G_s)^{2.5} \ \exp\big(-\frac{6.53 \times 10^9 \phi^{1.5}}{\beta G_s}\big) \tag{1.20}$$

where J_c is in A/cm^2 , ϕ is the metal work function in eV, G_s is the maximum surface gradient expressed in MV/m and β is the local field enhancement factor that generally depends on the geometry of the emitter.

- *Breakdown depends on the frequency of RF structure.* Threshold breakdown electric field can be defined as the maximum surface electric with controlled breakdown rate. The threshold breakdown electric field increases with higher RF frequency. In 1957 Kilpatrick summarized known experimental data with a simple empirical criterion for the maximum electric field allowed for a given RF frequency [41]:

$$f = 1.64 \cdot E(\mathrm{MV/m})^2 \cdot \exp\left(-\frac{8.5}{E(\mathrm{MV/m})}\right)\mathrm{MHz} \tag{1.21}$$

  As can be seen from this expression, the threshold voltage is to proportional to the square root of applied RF frequency.

  Kilpatrick also pointed out that the threshold could be slightly raised by surface processing methods. Surface processing refers to improving surface quality by treatment techniques or operating in high electric field environment. Since 1957, several experimental groups achieved gradients exceeding limitations posed by Kilpatrick criterion. Notably, the CLIC group demonstrated stable operation above 100 MV/m peak field in 11.4 GHz cavities [42].

- *Breakdown causes surface damage.* One of the consequences of RF breakdown is surface damage in RF structures. The damage can take different forms, like melted craters, surface cracks, and/or morphological changes to the surface structure [43, 44, 45]. All these types of damage can potentially lead to a decrease in the stable operating gradient of an RF cavity. The magnitude of damage caused by breakdown depends on operating

conditions of the system, the most significant one being energy in the system available for breakdown arc dissipation.

- *Breakdown rate depends on RF pulse duration and cavity gradient.* Recent studies at CERN show empirical dependence of breakdown rate (BDR) on pulse length, with the breakdown rate defined as ratio of breakdown events per number of RF pulses. Specifically, they report BDR to be proportional to $E^{30}\tau^5$ at X-band RF frequencies (between 7 GHz and 12 GHz), where E is average gradient and τ is pulse length [46].

- *Breakdown rate depends on the surface treatment.* Breakdown is commonly considered as being triggered from local surface defects. Generally, surfaces with lower defects density and less pronounced shape irregularities perform better.

- *Breakdown is sensitive to the material.* Observations of surface damage suggests that material choice is one of the limiting factors for breakdown. The majority of RF cavities are made out of copper - a material with high RF and thermal conductivity, reasonable price, and easy machining properties. Other materials that have been studied include gold, stainless steel, tungsten. A general observed trend is that relatively soft materials, such as gold, are less susceptible to breakdown compared to hard materials, such as stainless steel or tungsten [47]. Common parameter of "softness" is the tensile strength of the material.

- *Breakdown events are accompanied by radiation, light and sound bursts.* Vacuum arcs are local plasma discharges near the surface, accompanied by quick rise in detected radiation and light signals in visible spectrum. Ion bombardment of the surface during the discharge also creates the vibration of the structure walls which can be picked up by sensitive acoustic detectors [79].

1.5.5 RF breakdown in external magnetic field

As was mentioned in the introductory section, the designs of vacuum ionization cooling channel require operating normal conducting RF cavities in multi-tesla external mangetic field. Compared to other cavity geometries, pillbox-type structures are able to provide gradients close to the maximum on-axis surface field. To allow for muon beam passage, cavity can be equipped with thin beryllium windows in the center of the cavity's flat walls [48].

Gradient performance of 805 MHz pillbox-like cavities in an external magnetic field was tested at Fermilab. Strong dependence was observed between maximum stable gradient and magnetic field strength. Additionally, damage on the flat walls in the form of pits and spraying of copper droplets indicated destructive nature of breakdown in testing conditions [50]. Moreover, it was noted that gradient performance of the cavity in external magnetic field deteriorated over time. Figure 1.9 shows the gradient dependence on the external axial magnetic field in pillbox-like cavity experiment.

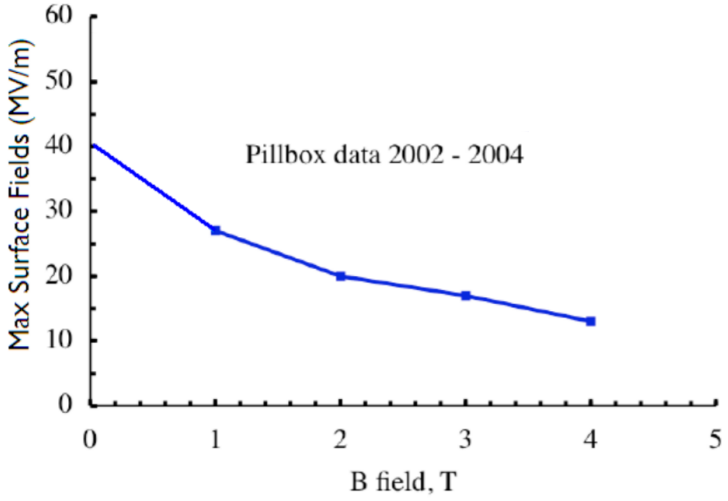

Figure 1.9: Breakdown gradients vs external magnetic field for pillbox-like 805 MHz cavity [50].

A similar experiment with a multicell 805MHz cavity tested in external magnetic field demonstrated deterioration in maximum operating gradient [49]. However, measured dark current and radiation were increased by a factor of 4 when operating in three tesla field. The

observed damage on the flat cavity window corresponded to the impact location of focused dark current beams emitted from an enhanced electric field region near the iris. Figure 1.10 shows the schematic of the multi-cell cavity, tested at lab G at the Fermilab.

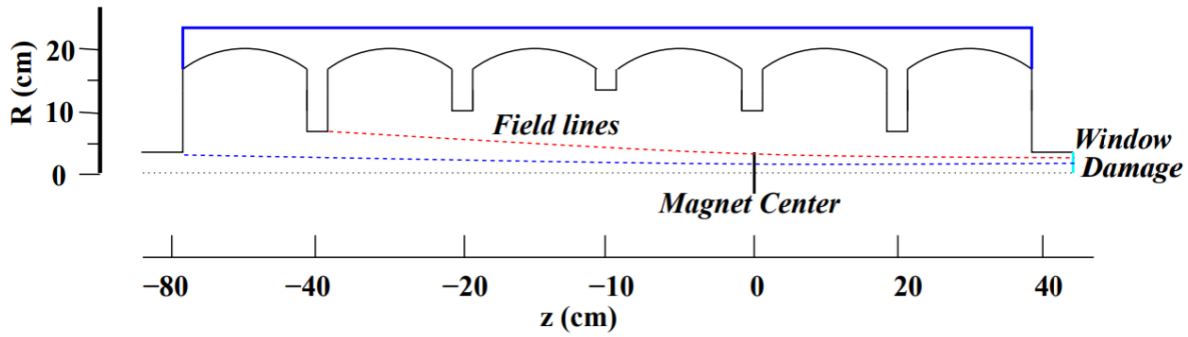

Figure 1.10: Schematic drawing for multi-cell cavity test. Red and blue dotted lines correspond to the hypothetical trajectories of electrons emitted from high-curvature irises [50].

Several cavities were tested at the Fermilab's MTA (see Section 2.1) studying their behavior in axial magnetic field. Summary and results of those experiments will be discussed in detail in Section 2.2.

CHAPTER 2

OVERVIEW OF EXPERIMENTAL PLATFORM

2.1 MTA experimental hall

Mucool Testing Area (MTA) is an experimental underground hall that was built at Fermilab to enable R&D efforts in RF structures for muon ionization cooling channels [51]. The goal of the facility is to develop high-gradient RF cavities capable of operating reliably in the environment of strong external magnetic fields and large radiation dosage generated by high gradient. The following capabilities and instrumentation are the part of the MTA:

- 12 x 6 meters experimental hall, shielded for X-rays with several feet of concrete block wall. The experimental hall is placed 3 meters underground with a labyrinth entrance and safety interlock doors for access.

- Spare 805 MHz Linac station is used to deliver power to the MTA experimental hall. The power is delivered through the 100 meter long WR-975 waveguide. 18 kV, 25 kW supply with modulator form RF pulse. The klystron, capable of producing a 12 MW RF signal with a maximum repetition rate of 15 Hz, is used as a power source. Pressurized waveguide equipped with Photo-Multiplication Tube (PMT) amplifier for breakdown detection and interlock system capable of shutting down the power to prevent damage is used to deliver the power to the MTA.

- A superconducting solenoid capable of generating a uniform magnetic field up to 5 T. The warm bore of the magnet is 44 cm and is large enough to fit 805 MHz cavity. Solenoid consists of two coils which can be energized with the common or opposing polarity. The magnet's 300 A, 7 V power supply is quench-protected.

- A cryogenic plant, providing liquid helium and nitrogen. A distribution system delivers gas for magnet cooling.

- Gas distribution and safety systems for operating cavities in the high-pressure gaseous environment.

- Turbo, ion and dry vacuum pumps to maintain cavity base pressures below 10^{-7} torr.

- A beamline capable of delivering 400 MeV H- beam from Fermilab's Linac with a maximum intensity of 7.5×10^{12} particles per pulse. The beamline is equipped with focusing magnets, beam profile monitors, and other supporting diagnostics. The purpose of testing RF cavities with external beam is to study the effect of beam on cavity performance and on RF breakdown in particular [52].

- A class 100 portable clean room that allows for local cavity assembly and inspection work.

- A Neslab HX500 water cooling system with temperature controlled circulator located in the cryoplant's compressor room. Water cooling allows for temperature regulation over RF cavities during high power operation.

- Extensive instrumentation and diagnostic tools for cavity operation and signal characterization (described in Section 2.5), for example, the ionization chamber for radiation detection.

2.2 Experimental programs in the MTA

Several 805 MHz and 201 MHz cavities were tested at Fermilab. The main goal of these tests was to converge on the optimal design for cavities used in the muon ionization cooling channels. RF breakdown in strong external magnetic field is a serious obstacle in using normal conducting cavities in proposed designs for ionization cooling channel. In this section I will discuss some significant results of operation of 805 MHz cavities in strong magnetic fields in Fermilab's MTA.

2.2.1 Pillbox cavity with grid windows

An 805 MHz pillbox-like cavity with RF gap length of 8.1 cm and 15.8 cm radius was tested in magnetic fields up to 5 tesla [53]. RF power is coupled through an aperture in the side wall of the cavity via a curved iris at the attachment point. Figure 2.1 shows the schematic of the cavity and simulated electric field distribution. The pillbox cavity was tested in several configurations of side walls: flat copper walls, copper walls with thin beryllium windows, copper and beryllium buttons in the center of the wall, and "grid" metal windows. I will discuss the motivation behind these configurations and main results of the high power tests.

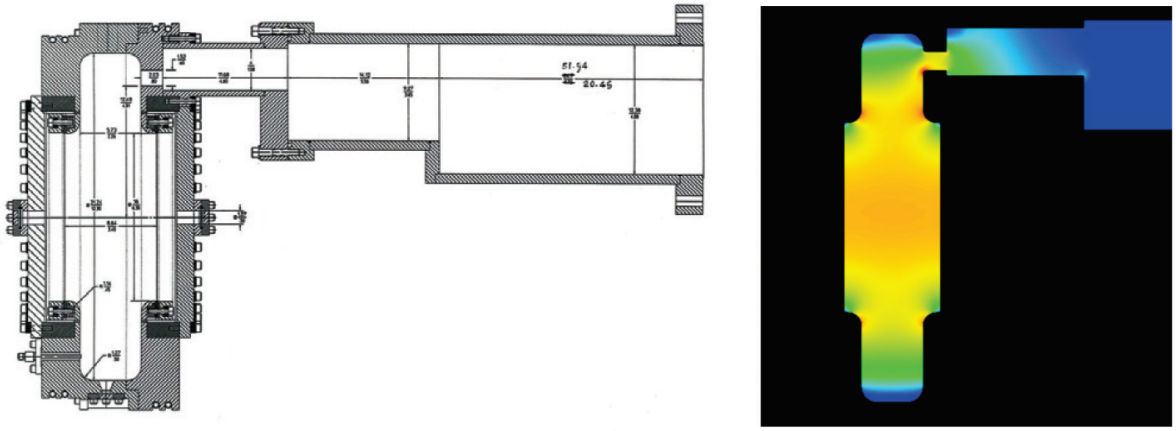

Figure 2.1: Schematic of the pillbox-like cavity (left) and simulated in OMEGA3P [100] electric field distribution (right) [45, 54].

In real ionization cooling channels cavities must allow for muon beam passing, which is not the case for traditional thick copper wall cavity. One solution is to introduce thin beryllium apertures allowing beam to pass while preserving the high shunt impedance (see section 1.5.2). Thin, curved beryllium windows have been successfully used in 201 MHz cavity [55]. The windows were coated with TiN layer to suppress multipacting. However in practical terms, use of beryllium is usually expensive and the hazardous nature of material requires extra safety measures.

An alternative approach is to use grid of metal tubes as a beam window. To be an effective

solution, the grid window must minimally scatter high energy muons, be conductive to allow for power dissipation, allow for reliable high vacuum sealing, and possess mechanical strength capable of withstanding plastic deformation from pulsed heating. Windows satisfying these conditioning were used in high power tests of the pillbox cavity [56]. Figure 2.2 shows the implementation of the gridd window design.

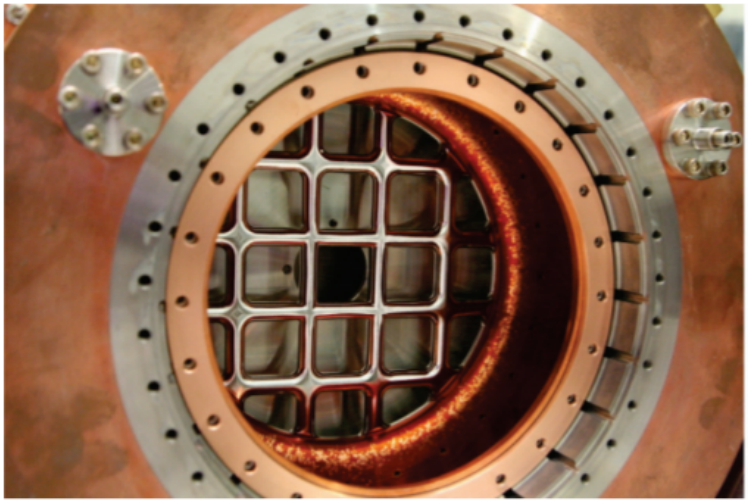

Figure 2.2: Partially disassembled pillbox cavity wall with one visible aluminum grid window [54].

Achieved accelerating gradients at high power runs in axial magnetic field with gridd window and beryllium window configurations will be discussed in Section 2.4.

To study the effect of different materials on breakdown phenomenon in external magnetic fields, another modification to the pillbox geometry was introduced. Pairs of copper and beryllium "buttons" were mounted on the cavity's longitudinal axis, creating enhanced electric field regions and, hence, inducing the breakdown in the vicinity of the button surface. Analysis of button damage suggests that beryllium is less susceptible to breakdown damage compared to Copper [45]. The arc current density of breakdown was estimated to range from 10^9 to 10^{11} A/m^2.

2.2.2 805 MHz High Pressure RF cavity program

Another approach for achieving muon ionization cooling combines the absorber and RF cavity. The Helical Cooling Channel (HCC) scheme was developed for the muon collider [59]. The concept of HCC combines functions of the RF cavity and absorber into one, by using a system of RF cavities filled with gas pressured up to 180 atm along the beam trajectory. The beam passes this system under external solenoidal and helical dipole fields, losing energy and undergoing dispersion effects at the same time. Figure 2.3 demonstrates the concept of Helical Cooling Channel design.

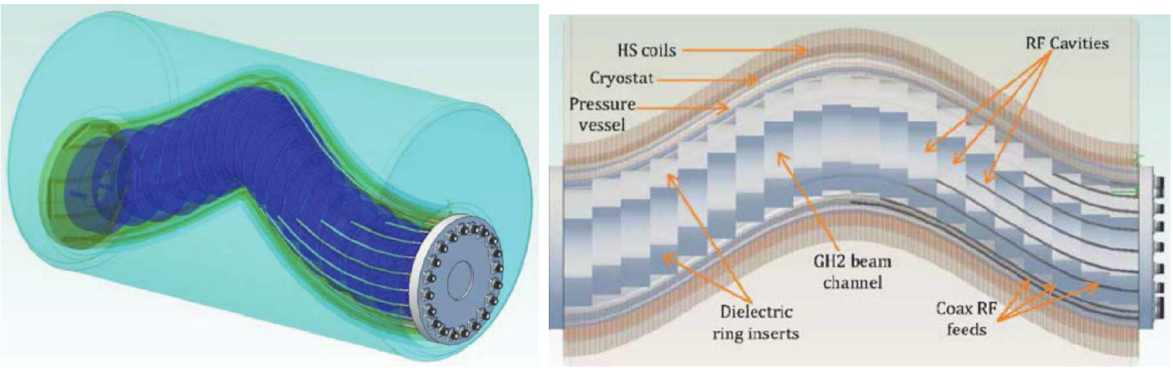

Figure 2.3: 3D view of HCC portion (left) and cutaway view of the same section with labeled components (right) [60]. "HS coils" refers to magnetic coils.

Most HCC concepts include normal-conducting RF cavities filled with high-pressure gas operating in multi-tesla external magnetic fields. In contrast to vacuum cavities, the gas acts also as an absorber of dark current electrons, suppressing the initiation stage of RF breakdown. Cavity capable of sustaining high internal pressure was designed and tested at the MTA with the purpose of studying operational and breakdown limits for different gases, gas pressures and surface materials [61]. A summary of high-power tests in an external magnetic field of 3 tesla is shown in Figure 2.4. Results demonstrate that at low gas pressures, the Paschen effect is the main limiting factor for accelerating gradient [62]. At higher hydrogen pressure, the breakdown gradient significantly exceeds gradients achieved in previous vacuum cavities. Another important result is that the breakdown gradient is independent

(within measurement error) of the external magnetic field. Thus, high-pressure cavity tests demonstrated a viable solution to the problem of RF breakdown in external magnetic fields in the context of muon ionization cooling designs.

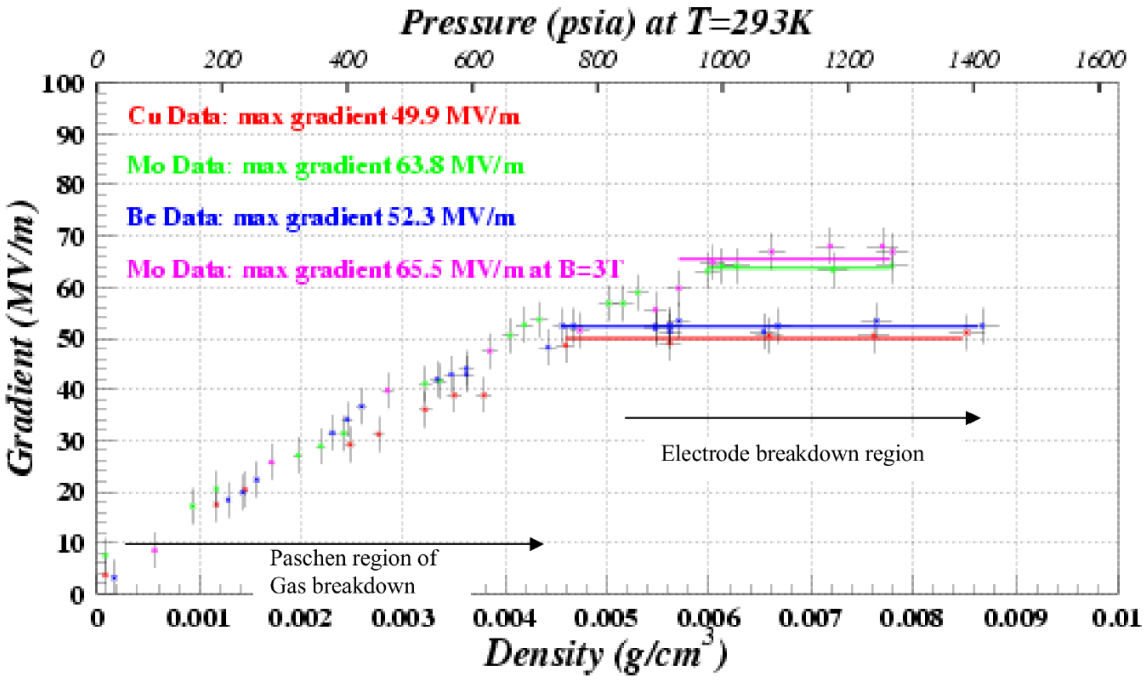

Figure 2.4: Measured maximum stable accelerating gradients for copper(red), molybdenum (green) and beryllium (blue) at 0 T and molybdenum at 3 T (purple) [63].

2.2.3 "All-Seasons" cavity

.

A cavity capable of operating both under high vacuum and filled with high-pressure gas, "a cavity for all seasons " was developed to study the role of gas pressure in the suppression of breakdown [57]. The experimental goals for the All-Seasons cavity included measurement of maximum stable operating gradient for external magnetic fields in the range of up to 5 tesla and for cavity pressure between 10^{-8} torr and 100 atmospheres, as well as optimization of conditioning sequence for best gradient performance. Figure 2.5 shows the cross-section of the cavity with simulated electric field distribution and a view of the cavity interior. Table 2.1

summarizes properties of the cavity.

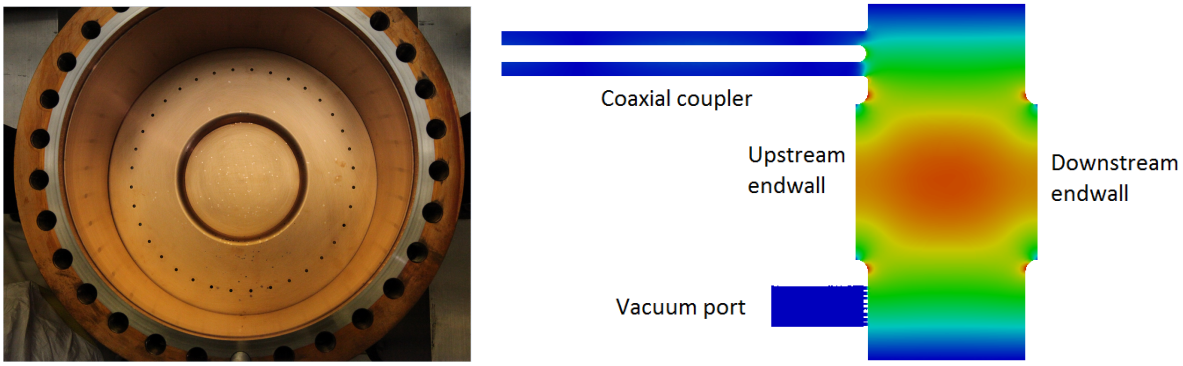

Figure 2.5: All-seasons cavity interior (left) and cross section of the cavity with electric fieldmap simulated in OMEGA3P. Cavity material is copper-plated stainless steel.

Table 2.1: RF Properties of All-seasons cavity [58].

Parameter	**Value**
Frequency	810.4 MHz
Q_0, Q_L	28000, 15500
Coupling constant, β	0.8
Gap length	14.5 cm
Base vacuum pressure	3×10^{-8} torr
Pulse length	30 μs
Stored energy at 20 MV/m	5 Joules
Pulse repetition rate	1 Hz

The All-seasons cavity was operated in magnetic fields between 0 and 5 tesla. After its last high power test the cavity was disassembled and inspected. Approximately 400 breakdown damage sites were found on each cavity wall. The structure of the cavity did not allow for surface inspection in-between runs at different magnetic fields, so it is impossible to assign each pit to magnetic field value. Characteristic breakdown damage is shown in Figure 2.6. The average volume of melted material of each pit is estimated to be around 0.1 mm^3. The energy required to melt such amount of copper is 0.4 J, while the amount of energy stored in the cavity at 20 MV/m is 5 J.

Damage inspection also revealed one-to-one correspondence between damage sites on the opposing walls of the cavity. Approximate 40% of the pits had a corresponding damage

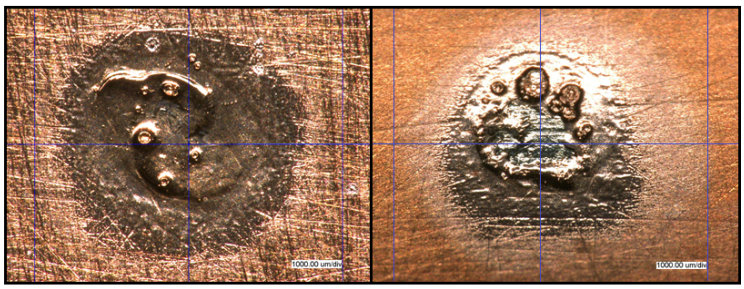

Figure 2.6: Microscopic images of typical breakdown damage sites in the All-seasons cavity. Characteristic diameter of each pit is around 1 mm.

site on the opposing surface. Figure 2.7 shows the matching of certain pit patterns on the opposing walls. In-depth analysis of damage matching in magnetic field will be discussed in Section 3.2, when discussing inspection results of Modular Cavity.

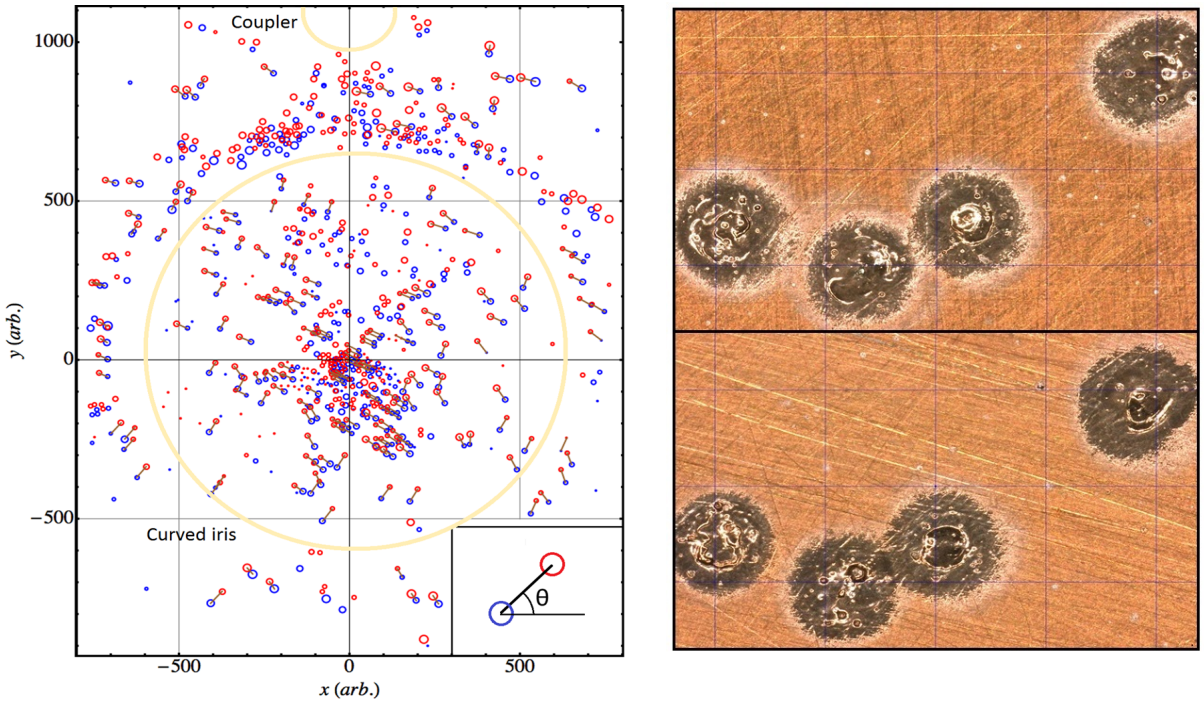

Figure 2.7: Left - distribution of breakdown damage sites on two opposing endplates. Blue circles correspond to the upstream plate, red circles to the downstream plate. Corresponding pairs are connected with lines. Right - micrographic example of matching patterns on the opposing plates [58].

The All-seasons cavity demonstrated record gradient when operated in 5 tesla magnetic field. Discussion on gradient performance of All-seasons cavity follows in Section 2.3.

2.2.4 201 MHz MICE cavity

.

A 201 MHz pillbox-like cavity was built for the final stages of MICE experiment [20]. Capabilities of MTA allowed for testing the module prototype cavity in the conditions close to MICE. The parameters of the MICE cavity are listed in the Table 2.2. The cavity's inner surface was electropolished to suppress field emission and reduce multipacting [64].

Table 2.2: Parameters and run configuration of MICE cavity.

Parameter	**Value**
Frequency	210.25 MHz
Q_0	53,500
Gap length	42 cm
Inner radius	61 cm
Beam iris radius	21 cm
Peak stable gradient	10.6 MV/m
Pulse length	180 μs
RF rep rate	5 Hz

The cavity was successfully tested with no detected breakdown events at the target gradient of 10.6 MV/m in the fringe field of MTA's 5 tesla magnet [65]. Such external magnetic field configuration is close to one assumed in the actual cooling channel.

2.3 Pulsed heating model of RF breakdown in magnetic fields

The pulsed heating model, proposed by Stratakis, Gallardo and Palmer, explains why we see the deterioration of the gradient in the presence of external axial magnetic fields [66]. The model estimates the limitations on the maximum achievable gradient by considering local surface heating effects. Metal surfaces have intrinsic defects (i.e. an asperity) that create electric field enhancement and boost electron field emission according to mechanism described by Fowler and Nordheim (see Section 1.5.4). Dark current, emitted from these asperities on the inner walls, gets focused by the magnetic field and repeatedly bombards a particular spot on the opposing wall. This bombardment heats up this spot over and over,

leading to the pulsed heating of local surface area. When this local temperature rise become larger than a critical value it can lead to plastic deformation, changes in surface topology, and eventually RF breakdown may be triggered [67]. This effect puts a limit on the gradients that can be achieved in strong magnetic fields. More detailed view on the pulsed heating model will be offered in Section 4.

Considering common operating conditions in previous experiments conducted in the MTA, Stratakis *et al.* produced predictions on the maximum operating gradient that can be achieved in an 805 MHz cavity with pillbox-like geometry. The result can be seen in Figure 2.8, where the black line corresponds to theoretical predictions of the model.

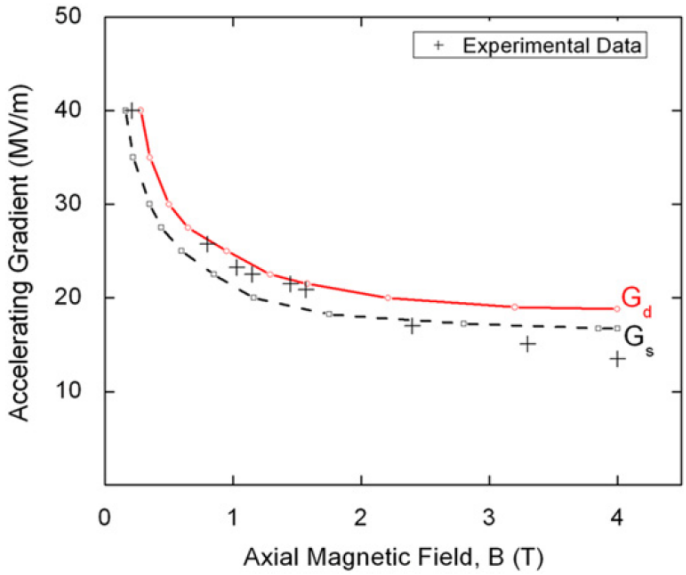

Figure 2.8: Predictions of the pulsed heating model for maximum gradients in 805 MHz pillbox-like cavity to reach critical local surface temperature [66]. Black crosses correspond to measured maximum gradients in a pillbox cavity [68].

As a consequence of the model and the MTA tests described in this Section, there are several potential ways one can consider to mitigate the effect of pulsed heating:

- Improve surface conditions of the cavity by applying various surface treatments, like polishing, aiming to decrease the amount and prominence of the defects that might lead to field emission of electrons. Some of the cavities tested at MTA were chemi-

cally polished (Modular Cavity, see Section 2.5) and electro-polished (201 MHz MICE cavity).

- Decrease the impact energy of dark current electrons by extending the RF gap of the cavity, effectively increasing the transit-time factor. In other terms, if the flight time of an electron traversing the cavity is longer than the half period of RF oscillation, its kinetic energy will decreased by the opposing electrical force. As a demonstration, consider a standard 805 MHz pillbox cavity with RF gap length $L_p = 10.2$ cm and All-season pillbox-like cavity with a longer gap of L_a =14.5 cm. Calculated impact energy of electron emitted at $\pi/2$ RF phase 20 MV/m gradient is $E_a = 1.7$ MeV in pillbox cavity and $E_p = 0.7$ MeV in All-season cavity. Lower energy electrons typically deposit less energy close to the surface of material they impact on, as the stopping power $\frac{dE}{dx}$ of the material positively correlates with the particle's impact energy.

- Change $E \parallel B$ condition so that electrons are deflected to the sides of the cavity. This concept was tested in the MTA on specially designed Box Cavity [69]. The main idea of Box Cavity geometry is to suppress surface damage caused by the focused beamlets of dark current electrons. Deflection is achieved by the external magnetic field being directed perpendicular to the electric field. The concept showed improved results over limited range of orientations. However, significantly lower shunt impedance of this cavity compared to standard pillbox geometry makes box-type cavity solutions power costly.

- Use materials with higher radiation length of electrons compared to copper (e.g. beryllium). Such materials would allow electrons to pass through the bulk of the material without depositing kinetic energy in the form of heat near the surface. For more discussion see Chapter 4.

2.4 Summary of gradient measurements in magnetic fields for 805 MHz cavities

Several experiments based in the MTA measured the high-gradient performance of 805 MHz cavities, as discussed in Section 2.2. The experimental data is summarized in Figure 2.9.

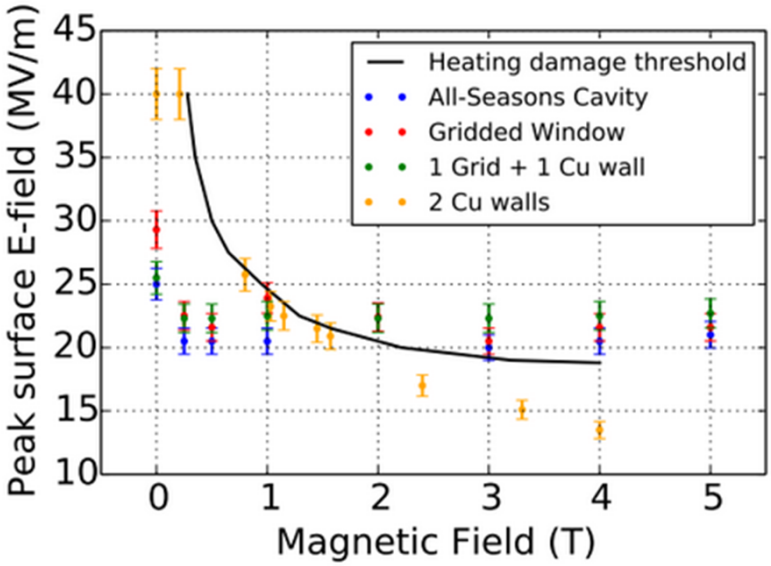

Figure 2.9: Gradient performance of 805 MHz cavities. Colored data points correspond to measured safe operating gradient of different cavity configurations tested in the MTA. The solid black line shows the prediction of the pulsed heating model [70].

It can be seen that experimentally measured gradients generally follow the trend of pulsed heating model predictions, but there is also some discrepancy between theory and experiment. The list of possible reasons why this discrepancy varies from one cavity to another includes:

- *Lack of careful surface treatment.* The pillbox-like cavity (marked as "2 Cu walls" in Figure 2.9) was machined copper structure without more delicate surface treatment. Its gradient performance is inferior compared to other tested cavities.

- *Choice of the flat walls material.* Some tested configurations included beryllium as the material of choice. Having longer radiation length for electrons compared to copper,

beryllium is less susceptible to dark current damage. As an illustration, the impacting electron with kinetic energy of 1 MeV sees the the stopping power near the surface $\left(\frac{dE}{dx}\right)_{Be} = 2.5$ MeV/cm in beryllium and $\left(\frac{dE}{dx}\right)_{Cu} = 22.2$ MeV/cm in copper. Another type of configuration involved gridded windows that allowed the majority of dark current electrons to exit cavity volume without impacting the walls.

- *Cavity geometry affecting electron impact energy.* The geometry of the cavity has an effect on the impact energy of dark current electrons inside the cavity. The All-seasons cavity' has a longer RF gap (15cm) compared to other 805 MHz pillbox-like cavities tested at the MTA. that increased the transit-time factor of electron traversing the cavity gap, effectively decreasing the electron energy upon impact.

- *Coupler design with electric field enhancement regions.* Field enhancement regions around the coupler facilitate field emission and increase the probability of local breakdown. The operating gradient of such cavities is limited by the breakdowns occurring in the coupler region rather than on-axis. Pillbox cavity tested at the MTA had the surface electric field near the coupler larger than on-axis.

- *Conditioning history of the cavity.* As the cavity undergoes the high power testing its surface condition evolves. Surface changes include but are not limited to local baking, pulsed heating damage, breakdown damage, evaporation of emitters etc. Depending on operating history of the cavity it might perform differently under similar conditions [71].

2.5 Modular cavity

2.5.1 Motivation

High power experiments at the MTA, outlined in previous sections, provided motivation for further systematic studies of RF breakdown in strong magnetic fields in controlled conditions [72]. Those cavities' designs did not allow for frequent surface inspection between

high power operations, making the tracking of surface damage under different operating conditions impossible. Additionally, most cavities' designs featured field enhanced regions near coupler that contributed to increased breakdown activity off cavity longitudinal axis. Effects of cavity geometry, in particular coupler design, were difficult to directly compare across different cavities. A new design of the cavity, allowing for better systematic studies of RF breakdown in strong magnetic field in controlled operating conditions, was called for.

2.5.2 Design and capabilities

An 805 MHz "Modular" cavity was designed and built with removable flat end walls to facilitate surface inspection between high-power runs in different conditions and trace the effect of different materials on breakdown behavior. Additionally, modular design of the cavity opens the possibility of evaluating breakdown effects at different values of stored energy by changing the central cavity body. Modular Cavity's design fits requirements for practical use in the actual ionization cooling channels of muon collider or neutrino factory. At the same time, the cavity is integrable into the MTA facility.

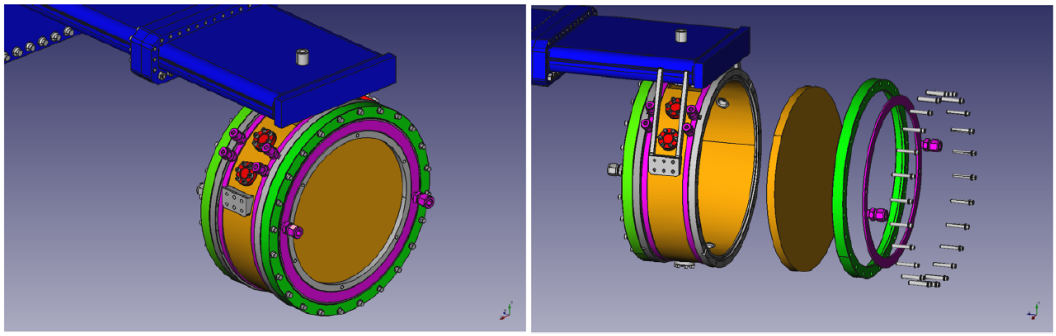

Figure 2.10: 3D model (left) and exploded view (right) of modular cavity, showing the assembly process of a flat wall [73]. The flat endplate is mounted on the cylindrical body (both shown in orange) of the cavity and sealed with the clamp rign (green). Two instrumentation ports on the cavity body are shown in red. Flat waveguide (blue) is shown in blue.

Figure 2.10 shows an exploded view of the cavity body and waveguide geometry. Cavity consists of the a cylindrical body (14.2 cm in radius and 10.4 cm in inner length) and two flat end walls, each 1.42 cm thick. The stainless steel clamp ring at the perimeter of cavity body

is designed to clamp the flat end walls to the cavity body, providing required pressure for good vacuum and RF contact. Water lines built into the cavity body and across the front of the flat endplates provide temperature regulation of the body and endplates. This helps limit the temperature deviation across the cavity walls during high power tests. The maximum measured temperature rise during operation was 10 ^{o}C. Six instrumentation ports on the circumference of the cylindrical cavity body accommodate pickup loops measuring cavity gradient and optical fibers for spark detection. Flat waveguide components are stainless steel plated in copper. The Modular Cavity design uses magnetic coupling to transmit power into the cavity through the 56-cm long narrow waveguide. Standard WR-975 waveguide is used to transmit power from the source to the narrow portion.

Figure 2.11 demonstrates the interior design of the modular cavity. The inner surface of the flat copper walls is coated with 20 nm a thin layer of titanium nitride. To create proper RF contact, a $\sim$ 2 mm thin copper gasket is placed in the groove next to the O-ring. During the assembly process, the stainless steel clamp is bolted in sealing the cavity with the flat endwall. The fully annealed soft copper gasket is compressed between the body and the plate, deforming for optimal RF contact. The full modular cavity assembly is shown on Figure 2.12. The cavity is placed on rails, mirroring the rails mounted in the MTA superconducting magnet bore, making the process of installing the cavity into the bore easier. A schematic of the Modular Cavity installed in the magnet bore is shown in Figure 2.13. Cylindrical stainless steel flanges on the waveguide couple to turbo and ion pumps. Ceramic window in the WR-975 waveguide upstream from vacuum ports is installed to separate the 1-atm power transmission system from the evacuated cavity volume. The base vacuum pressure of the Modular Cavity is 3x10^{-8} torr.

Another design aspect of the cavity is the low ratio of peak surface electric filed on the main axis to the surface field in other regions of the cavity. As mentioned before, previously tested 805 MHz cavities in the MTA have experienced RF breakdowns in the coupler region, where the high curvature metal features were creating an electric field enhancement. In

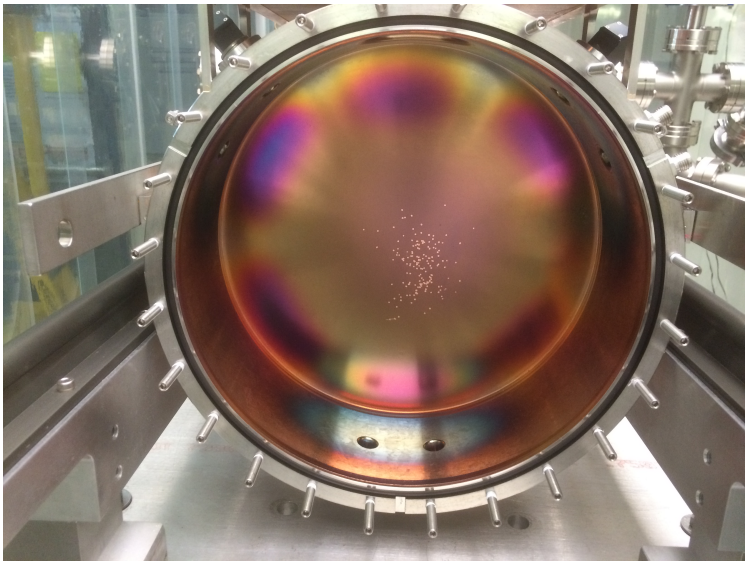

Figure 2.11: Interior view of the Modular Cavity. Six holes in the cylindrical body are instrumentation ports described above. The black rubber O-ring provides the vacuum seal of the interior volume.

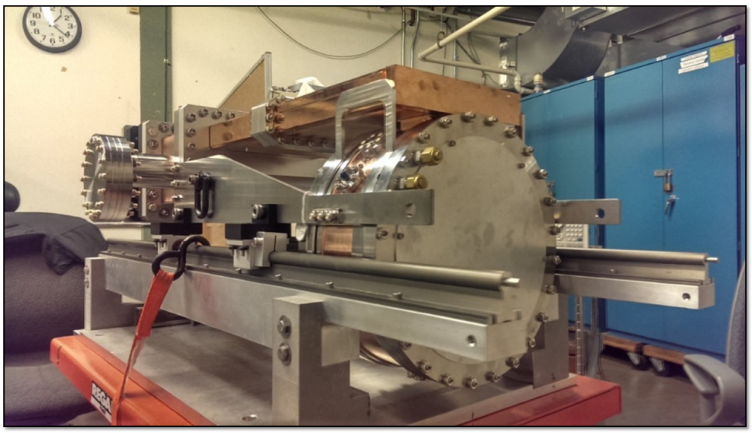

Figure 2.12: Modular cavity assembly setup. Cavity body clamped with the flat copper endwall is attached to the flat waveguide. The whole construction is attached to the fixture on rails.

order to avoid this additional complication, one needs to make sure that most breakdowns are localized on the flat endwalls surface. As breakdown probability is typically approximated by the power law of local peak electric field (see section 1.5.4), it is important to keep the ratio of peak surface electric field on the main axis to that near the coupler region. To make sure this ratio is maximized, SLAC's ACE3P finite-element simulation code was used in the design of modular cavity [78]. Simulated ratio for the Modular Cavity design is $f = 5.2$.

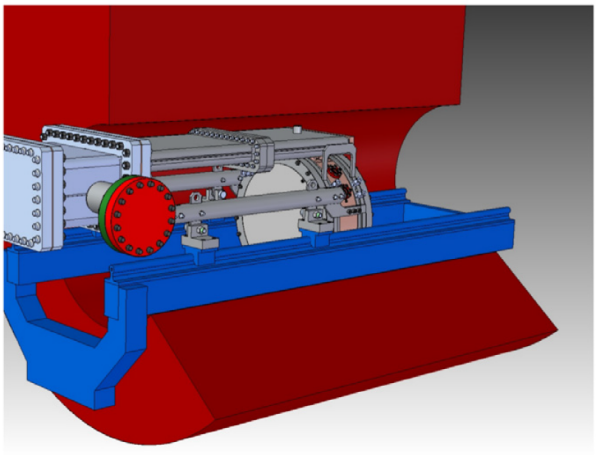

Figure 2.13: Modular cavity installed in the bore of MTA's superconducting magnet [73].

Figure 2.14 shows the color-coded distribution of peak electric and magnetic fields across the cavity and waveguide volume. Note that peak values for magnetic and electric field are separated by $\pi/2$ phase shift.

Another coupler design limitation is due to multipacting behavior. The multipacting effect refers to the phenomenon when stray electrons impact on the cavity's inner surface, causing secondary electron emission from that surface. These newly emitted electrons are again accelerated by the RF fields creating electron avalanche effect. Two types of multipacting behavior are relevant for designs of modular cavity: two-point multipacting and single-point multipacting. Single point multipacting occurs when emitted electrons impact back on their emission site. Two-point multipacting is a more prevalent issue for metal cavities and occurs at a resonance between the electron travel time and the RF phase of impact events of primary and secondary electrons [74]. Essential to multipacting effect is the secondary emission yield profile of the surface - average number of secondary electrons emitted after primary electron impact. Typical secondary yield of metals used in modern RF cavities exceeds one, making them susceptible to multipacting. To suppress secondary emission, inner surfaces of flat beryllium and copper endplates used in modular cavity experiments were coated with the thin ($\sim$20 nm) layer of titanium nitride, material with lower secondary electron yield [75]. Typical secondary electron yield for 500 eV electrons is 2.1-2.3

for unprocessed copper and 1.2 - 1.8 for TiN coating [76, 77].

Track3P, a particle tracking code, was used in finalizing the coupler geometry for the range of external magnetic fields and accelerating gradients. The optimized geometry of the coupler allowed to minimize the multipacting effect on cavity operation [73]. A summary of the cavity's design parameters is shown in Table 2.3.

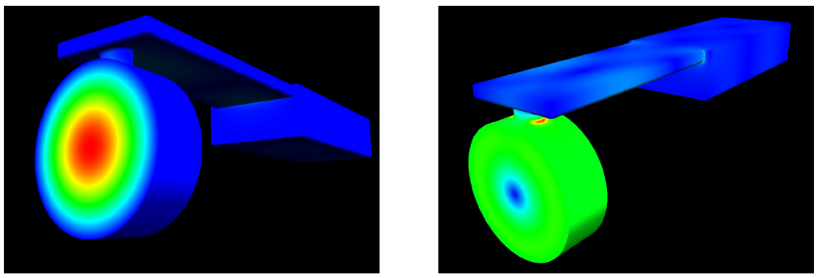

Figure 2.14: Simulated field distribution in the cavity and waveguide. Red color show the highest electric (left) and magnetic (right) regions, blue corresponds to the low field values.

Table 2.3: RF Properties of the Modular Cavity

Parameter	**Design value**
Frequency	804.5 MHz
Q_0, Q_L with copper plates	23000, 11000
Coupling constant, β (simulated)	1.3
Gap length	10.44 cm
Inner radius	14.22 cm
Peak electric field ratio	5.2
Base vacuum pressure	$3x10^{-8}$ torr
Pulse length	30 μs
Stored energy at 20 MV/m	6 joules
Repetition rate	2 - 10 Hz

2.6 Instrumentation

Extensive instrumentation was used in order to fully characterize operation conditions and signals coming from the Modular Cavity. Among those are:

- *Small fast plastic counters X-ray counters.* Each detector consists of a scintillating material, lightguide and photomultiplier tube. Typical rise time of the counters' signal

is $\sim$ 200 ns. Scintillators are about 5 cm x 5 cm x 1 cm with 2 meter-long lightguide. As PMTs are sensitive to magnetic field, shielding is required to enable detectors' proper operation. Therefore, PMTs are enclosed in tubes of high magnetic permeability metal (Mu-metal or similar). Furthermore, when the magnet is operational, the PMTs are placed as far away from the bore as possible, and oriented perpendicular to the magnetic field lines to minimize penetration.

- *Acoustic sensors.* Passive acoustic transducers comprised of a piezoexlectric crystal were built for taking acoustic data on breakdown events [79]. These sensors were designed to be able to operate in high external magnetic field, where use of electric-powered components is highly restricted and only non-magnetic materials are allowed. Microphones were mounted using non-gaseous epoxy and connected to the pre-amplifier installed outside of magnetic bore. Locations for the microphones were chosen as follows: 4 sensors on each endplate and 2 sensors on the narrow waveguide portion.

- *Optical fibers for breakdown detection.* Optical fibers installed in two of the six ports on cylindrical body monitor visible light inside the cavity. Picked up light signal is then guided to the photo-multiplying tubes that convert light into electrical signal.

- *Magnetic loop pickups in cavity.* For real time measurement of cavity gradient, two magnetic loop pickups inserted through the available ports on the modular cavity body were used.

- *Temperature sensors on cavity body and endplates.* Several Resistance Temperature Detectors (RTDs) were used to monitor temperature of cavity's endplates near center and edges, on cylindrical body and narrow waveguide piece near coupler. Class A tolerance RTDs, made from 100 Ohm were epoxied on the external surfaces of the cavity and waveguide [80].

- *Hall temperature sensors for monitoring ambient temperature in the experimental area.*

- *Ionization chamber radiation detectors.* Responding to ionizing radiation, ionization chamber is the gas-filled radiation detector for X-ray measurement.

- *Forward and reflected power directional couplers on the waveguide.* Directional couplers allow for tracking the ratio of power reflected from the cavity to the power transmitted to the cavity.

- *Water flow meters.* Water flow sensors are used to ensure stability of the water flow in the cooling lines around cavity body and endplates.

- *NaI radiation detector.* NaI crystal was installed about 6 meters away from the magnetic bore to avoid the effect of magnetic field on detector's operation. NaI is a scintillating material with high luminescence efficiency and produces one of the highest signals in a PMT per absorbed radiation dosage.

- *Chipmunk IV type radiation area monitors* [81].

- *Vacuum gauges.* Baseline vacuum level for modular cavity high power tests is 3×10^{-8} torr. Three vacuum gauges, placed in vacuum pumps' connection to the waveguide portion of cavity assembly were used to ensure stable vacuum pressure.

- *Faraday cup.* Coaxial Faraday cup is 5 cm in the outside diameter, tuned to 50 Ohm using time domain reflectometer. Additional signal amplifier was installed in the signal cable path, about 2 meters downstream, to compensate for amplitude loss in the cable between experimental hall and DAQ station.

2.6.1 Data acquisition system

Three main data streams are used for data acquisition system:

- The RF data stream is displayed as waveforms on the oscilloscopes. Regular captures of oscilloscope waveforms are set by the shift operator, and typically performed every

10 minutes to an hour. Additionally, the user has an option to manually capture these waveforms at any given time. In the event of detected breakdown, all oscilloscope outputs are also stored to the disk array. Each waveform has a unique filename and pulse number so that it can be identified for future analysis.

- Parallel to these waveform captures, DAQ program records a summary of operational parameters in the binary log files. List of parameters includes:
  - Clock time and pulse number of each recorded event
  - Peak amplitude, rise and fall duration in the pickup signal
  - Ratio of pickup to reflected power signal
  - Drive amplitude
  - Resonant frequency
  - Breakdown triggers, if applicable (see Section 2.7.1)
- In addition to signals going through Labview's VI, signal from MTA instrumentation that does not require sampling rate higher than 10 Hz is being stored through ACNET interface [84]. Such signals include the number of accumulated RF pulses during the recent run, resonant frequency, and pickup probe voltage, number of spark events, etc. ACNET parameters are stored on Fermilab servers and can be remotely accessed. Utilities are in place to automatically notify the operator if some of the critical parameters (e.g. cavity surface temperature) go out of their nominal ranges.

2.7 Run control system

Run control enclosure is located 100 meters from the MTA experimental hall in the vicinity of Fermilab's LINAC station 8. Run control software and hardware were developed specifically for the needs of the MTA group [82]. The DAQ system consists of several desktop computers running National Instraments Labview software coupled to an array of oscilloscopes [83].

Waveforms of RF signals are acquired by the National Instrument's 60 MS/s, 8 Channel digitizer/oscilloscope card. A general purpose interface bus communicates with the signal generator and five oscilloscopes are used for waveform acquisition and capture, including Agilent 80308B, Lecroy 625Zi, Tektronix DPO7104, Tektronix DPO510 and Agilent 7304. The sampling rates for oscilloscopes are between 20 GHz and 1 GHz, minimal bandwidth is 3 GHz. Master timing distribution module is used for simultaneous triggering of periodic and breakdown event captures in the oscilloscopes. RF waveforms are acquired by the digitizer card and then passed to Labview's Cavity Waveform Analysis VI for the measurements, detection of breakdown events, and logging. Measurements on the pickup probe signal include peak voltage, fall and rise time, exponential fitting of the time constant. Figure 2.15 shows the photo of the control room.

Figure 2.15: Run control room at Fermilab's LINAC station 8. Shifter's desk is equipped with run control monitors, waveforms from oscilloscopes (racks on the left) are analyzed in real time by Labview-based software.

2.7.1 Breakdown detection algorithm

During breakdown pulse, energy stored in the cavity gets dissipated in less than a microsecond, which can be seen as a sharp fall in pickup envelope signal. Due to impedance mismatch, sharp spike in reflected power signal is observed immediately following the spark. Sparking is also accompanied by the burst of radiation and visible light, that gets picked up by the optical fiber looking inside the cavity.

The breakdown detection algorithm is implemented as a logical OR between three triggers. First, the threshold voltage on the optic fiber looking into the cavity, detecting flash of light during the spark. The second signal is the fall time of the cavity probe voltage which must be shorter than some user-defined value. Typical threshold value for 805 MHz vacuum cavity is one microsecond. The third signal is reflected power spike immediately following the spark before external circuit detects breakdown event and turns the high power RF drive off. Figure 2.16 demonstrates the logic behind the breakdown detection system.

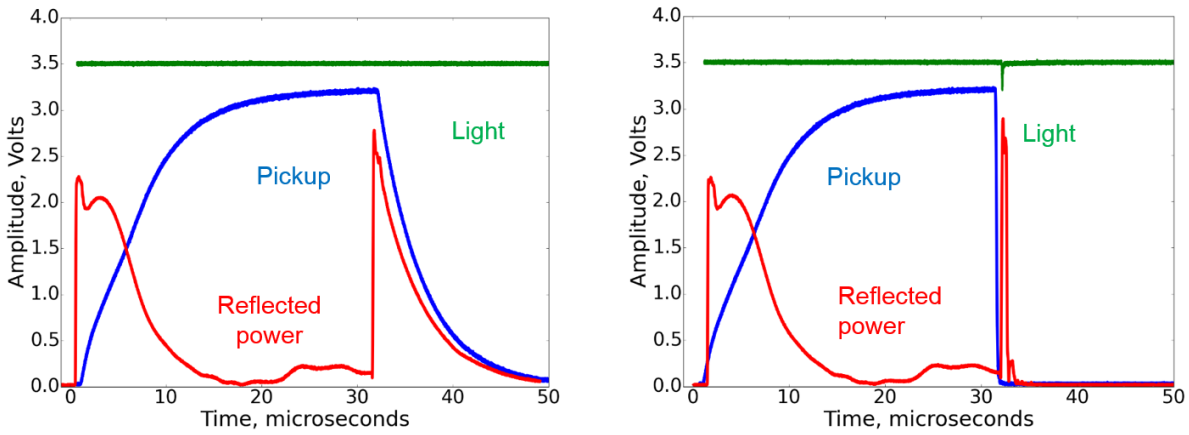

Figure 2.16: Example of normal RF pulse (left) and breakdown pulse (right) during Modular Cavity operation. Accelerating gradient is 32 MV/m.

2.7.2 Cavity tuning

During high-power, steady-state operation, the inner surfaces of the cavity experience a rise in temperature proportional to gradient, due to ohmic heating. This temperature change

slightly distorts the dimensions of the cavity, which translates into a shift in resonant frequency of the cavity and can disrupt resonance. To achieve precise resonance, the RF drive frequency has to be adjusted accordingly. The run control algorithm uses a sequence of predetermined steps *df* on each side of the most recent center frequency to check whether (a) the amplitude response of the cavity is maximized and (b) the ratio of integrated cavity probe signal vs. reflected signal is maximized. Typical sweep step for 805 MHz drive is 10 kHz and frequency adjustment is 1 second.

2.7.3 Run control procedure

One of the main goals for the modular cavity program is the measurement of maximum safe operating gradient in external magnetic field. Safe Operating Gradient (SOG) is defined by the threshold spark rate of 10^{-5}, therefore, the accurate measurement of spark rate is essential. One would be tempted to maximize the number of breakdown events to improve precision of the spark rate measurement. However, inflicting too many breakdown events can potentially:

1. Negatively affect the high gradient operation of the cavity. Damage caused by the breakdown accumulates on the surface and might lead to the increased spark probability in the subsequent operation.

2. Over-complicate the surface inspection process at the end of the run. Potential pile-up of the damage features on top of each other might hinder the damage documenting procedure.

3. Make experiment duration impractical. Operating the cavity at 10 Hz repetition rate (maximum allowed rep rate limited by DAQ response time) near SOG means the on average, each new spark event occurs every $\sim$3 hours.

To ensure the stable high power operation and the consistent measurement sequence, special run algorithm was developed and used throughout all Modular Cavity high power

runs. Several simplified assumptions are built into procedure:

- Spark rate depends only on the operating gradient
- Spark rate increases with the gradient
- At a given gradient value, probability of a breakdown event is approximated by the Poisson process:

$$P(N, \mu, G) = f(G)\ \frac{e^{-\mu}\mu^{N}}{N!} \tag{2.1}$$

  where μ is the measured spark rate, $P(, N, \mu)$ is the probability of N spark events occurring in unit time, G is the cavity gradient, and $f(G)$ the function that captures the breakdown rate dependence on gradient.

Every high power run starts with the low gradient operation to allow for the processing of surface contamination, inflicted during the inspection. The gradient is slowly raised with the predetermined rate : standard procedure implements the drive amplitude increase of 0.02 dB every 30 seconds. If multipacting behavior is observed, the gradient is kept at the constant level until multipacting subsides. This "processing" of the multipacting barriers is done to prevent negative consequences of the multipacting phenomenon at higher operating gradients. Typically, multipacting behavior is diagnosed by the increased vacuum activity and/or by the irregularity of the RF pickup signal. Figure 2.17 shows an example of the multipacting behavior observed in the Modular Cavity operation.

When RF breakdown event occurs, the run control hardware instantly lowers the delivered RF power by 3 dB to (a) prevent the excessive surface damage by succeeding breakdowns (b) allow the vacuum pressure to normalize. After the power decrease, the standard gradient ramp up continues until the next registered breakdown event. Algorithm enforces change in the procedure only when two consecutive sparks occur at the same gradient level (within tolerance window $\Delta G \sim 1$ MV/m). Figure 2.18 shows the run algorithm in the form of block

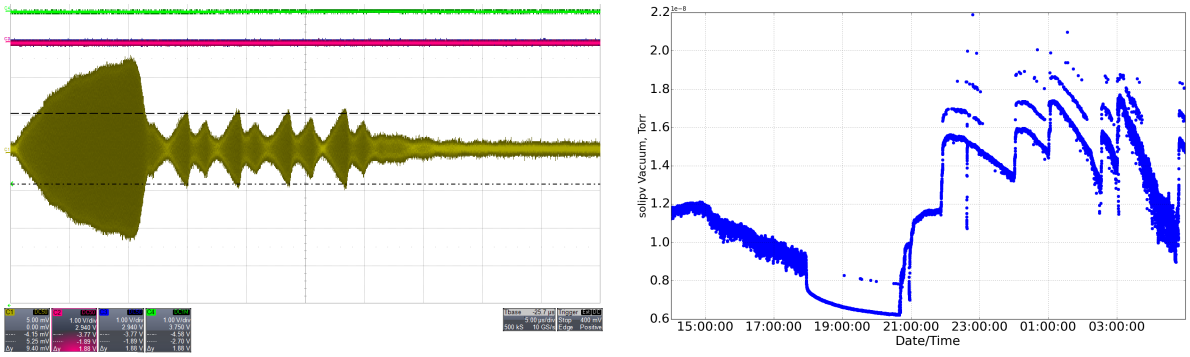

Figure 2.17: Left - example of the distorted RF pickup signal during the low level multipacting. Right - increased vacuum activity caused by multipacting . Note the steadily decreasing vacuum pressure during normal operation (before 19:00) and the pressure fluctuations once the multipacting starts.

diagram. To determine whether two sequential sparks indicate “hard” or “soft” breakdown barrier,the spark rate is measured at the current gradient level. Barrier is considered ”soft” if RF conditioning leads to lower breakdown rate. Measurement time Δt was chosen to be the time it takes to accumulate 2×10^5 RF pulses. According to Equation 2.1, at the spark rate of 10^{-5}, the probability of not registering the breakdown event in 10^5 pulses is $p \approx 14\%$. If no sparks occur during Δt, the ramping kick scooter is resumed. Otherwise, the breakdown rate measurement at fixed gradient level continues. This logical step in the run algorithm leans towards ”over-shooting” the safe operating gradient and is implemented as a time-saving mechanism - waiting for several sparks multiple gradients adds days in operating time. In case the measured spark rate exceeds the target value of 10^{-5} , the run algorithm initiates roll back to the last stable gradient plateau and starts normal sequence again. Breakdown rate at the target gradient is determined based on the minimum of 10 spark events, which gives the standard measurement error in breakdown rate of 30%. High power run can be interrupted for the surface inspection if the number of accumulated sparks exceeds critical value N. Typically, N is set in the range of $50 - 150$. Intended behavior of the run algorithm for is shown in Figure 2.19.

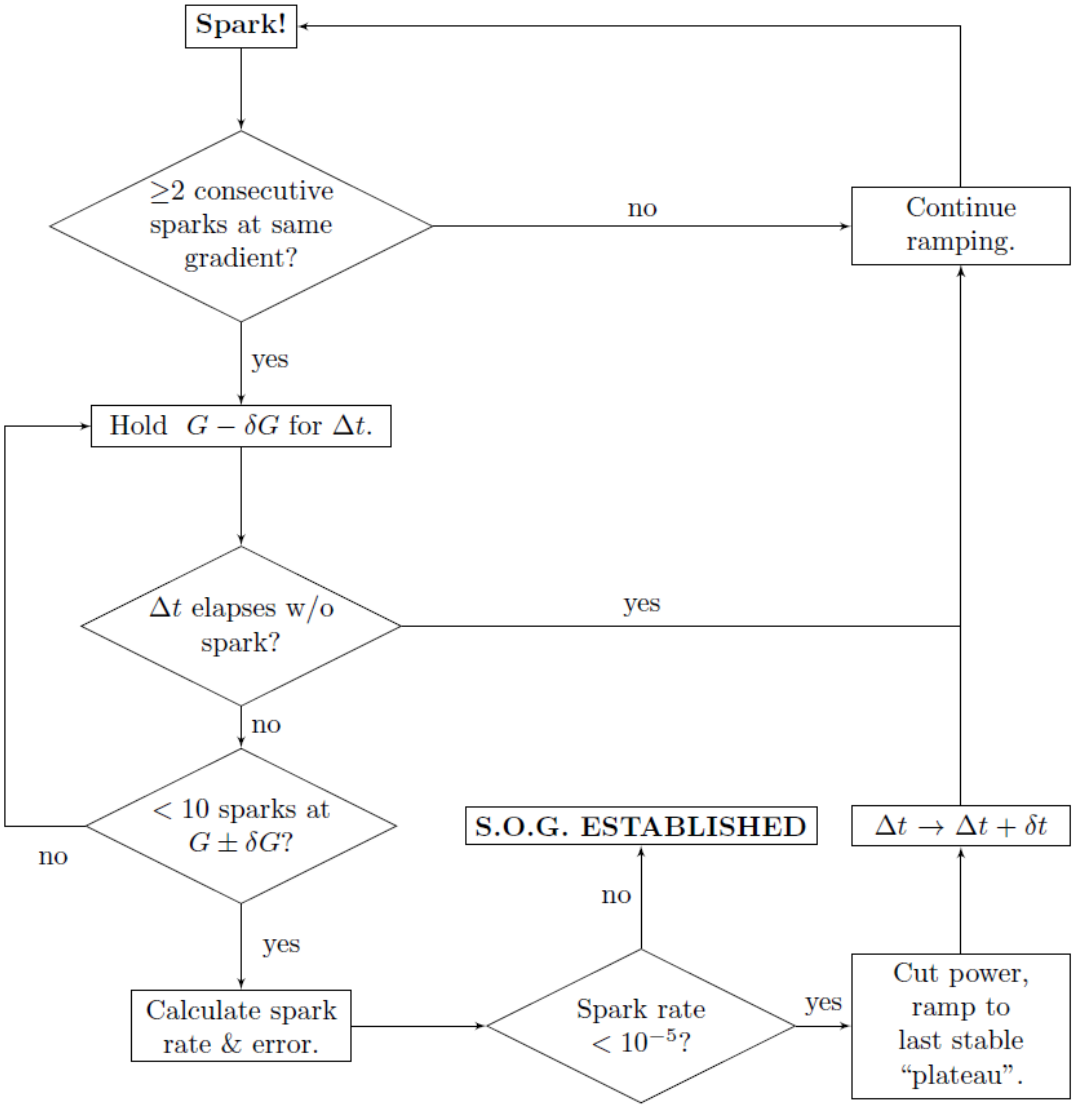

Figure 2.18: Block diagram outlining the run algorithm's logic. Typical $\Delta t = 2 \times 10^5$ RF pulses, $\delta G = 1$ MV/m. Block diagram is created by D. Bowring.

2.8 Surface inspection procedure

One of the goals of the Modular Cavity program is to trace the changes in surface condition after high power tests in different external magnetic fields. For this purpose, the surface inspection procedure was performed after each high power run. Some inspections took place in the middle of the run in case the spark count approached critical value. Logistics of the inspection procedure involved several steps:

- Low power RF calibration of the evacuated cavity in the magnet bore.

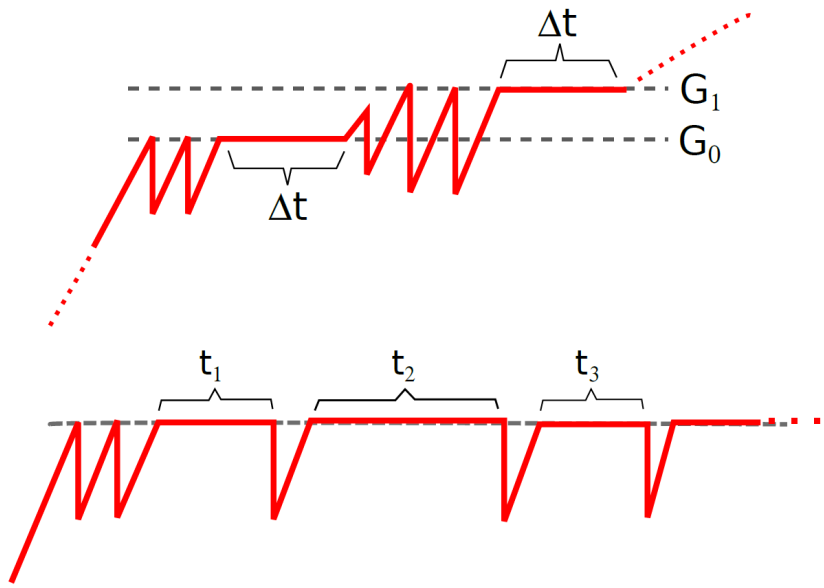

Figure 2.19: Hypothetical spark pattern and the run algorithm response. Vertical lines correspond to the spark events followed by the automated 3 dB decrease in delivered RF power. Top - barriers G_1 and G_2 are "soft", as after 2 consecutive sparks no breakdown event observed during Δt. Bottom - spark rate is measured at the constant gradient by accumulating at least 10 sparks. Drawing is courtesy of D. Bowring.

- Modular cavity is disconnected from the water cooling system, vacuum and other instrumentation.
- Cavity is extracted from the magnet bore and transported to the portable cart.
- Clean up of all external surfaces with water and alcohol wipes to avoid contamination of the clean room environment.
- Cavity is transported to the portable clean room inside the MTA experimental hall.
- Removal of both endplates from the cavity. Procedure performed by minimum of two qualified personnel, dressed in the clean room garment.
- Inner surface of both endplates is scanned with high-resolution flatbed scanner (see Subsection 2.8.1 for optical instruments' specs).

- Microscopic surface inspection is performed using optical microscope in the MTA clean room, clean room in the Fermilab's A0 facility or in the Spectroscopy lab at the Fermilab's Technical Division.

2.8.1 Optical instruments and their capabilities

Portable inspection system, designed for the clean room conditions, was used to characterize breakdown damage on the inner surfaces of the Modular Cavity. The following instrumentation was used for the surface inspection process:

- Flatbed scanner with maximum re!solution of 10^5 pixels per mm^2. Most high resolution images were obtained at 1800 dpi setting.

- Digital Keyence VHX-100K optical microscope. Two optical lenses were used interchangeably: 20x-200x and 500x - 5000x zoom. Microscope is also capable of constructing 3D images by implementing depth-from-defocus method [85].

- Digital Keyence VK-9700K color 3D Laser Microscope. Capabilities of this microscope include the automated motorized platform, the high precision 3D imaging, and the profillometry analysis.

Figures 2.20 and 2.21 show the setup used for inspection process in the portable clean room in the MTA and clean room at the Fermilab's A0 facility.

2.8.2 Environment standards and handling techniques

As the inspection process requires dismantling and handling cavity components, it is inherently prone to risks of damage and contamination. Thus, certain safety precautions must be followed, especially when handling the beryllium components. Beryllium dust poses a serious risk to human health.

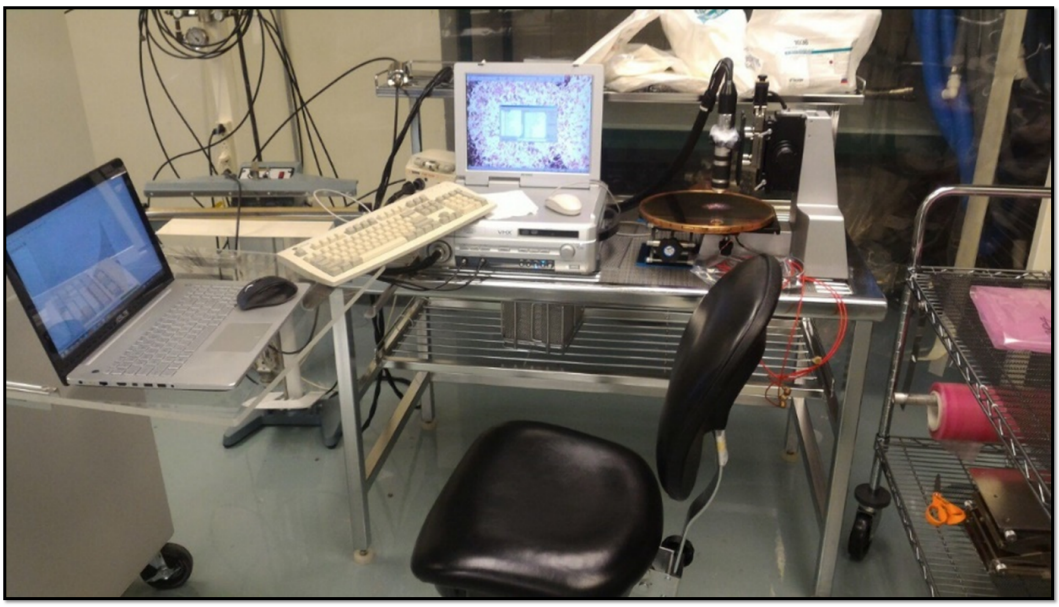

Figure 2.20: Portable inspection setup in the A0 clean room. Microscopic image is displayed on the computer screen in real time, enabling the prompt survey of damage features. High-resolution scan of the endplate surface on the laptop screen is used as a map for microscopic lens navigation. Copper endplate is placed on the movable flat platform under the lens.

Figure 2.21: Portable cabinet with instrumentation for microscopic inspection (left). Observing and mapping the damage under the microscope (right).

Disassembly and assembly of the cavity is a procedure with elements of risk. As cavity components are strained under external bolts and vacuum pressure, providing tight fit for the good vacuum and RF seal, the unforeseen complications are possible. Biggest operational hazard is the scratching the inner surfaces of the endplates when removing them off the cavity. To mitigate the possibility of damage, the endplates are equipped with the special handles. Copper endplates's handles are directly drilled into the material, while handles on beryllium are attached to the aluminum buttons epoxied to the endplate surface. Figure 2.22 shows the outer surfaces of the endplates with the attached handles. Minimum of two people is required to satisfy the safety of the endplate removal process. One person handles the endplate, while another ensures the sufficient clearance between the endplate and the surrounding structures.

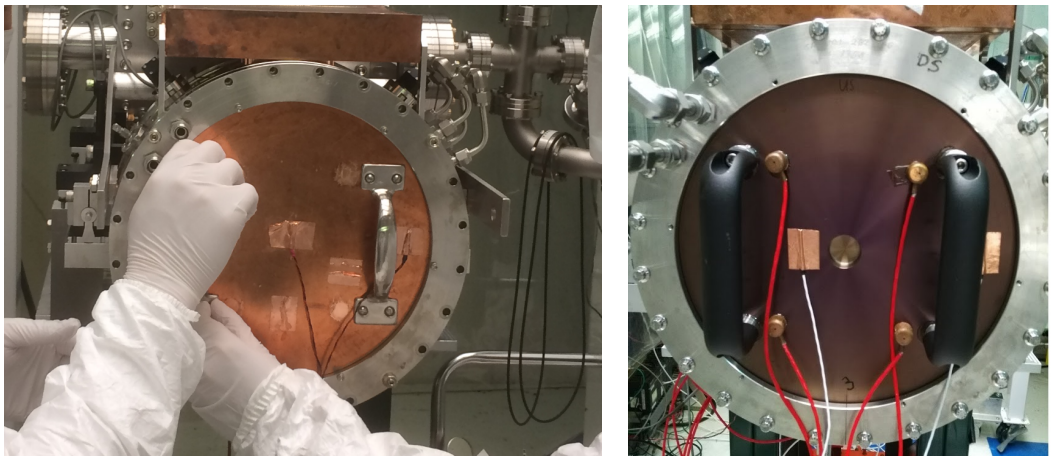

Figure 2.22: Copper endplates with the rigidly mounted handles (left), beryllium endplates with epoxied handles (right).

Preventing the contamination of the inner surfaces during the inspection process is important for consistency of the high power tests. For this reason, all assembly and disassembly work was conducted inside the portable ventilated clean room. All personnel, entering the clean room, must wear special suit, mask and gloves. Equipment and instrumentation entering the clean room is wiped with the alcohol-soaked wipes. As the main purpose of the surface inspection is to identify new damage and trace the evolution of surface features, clean environment during the microscopic inspection is paramount. Inspected surface is regularly

treated with the lint-free dry napkin, wiping away the foreign dust particles.

2.8.3 Experimental goals of the Modular Cavity program

The design of the modular cavity allows for a turnaround time as low as one week in the surface inspection process. Modular construction of the cavity allows for structural modifications in both used materials and geometrical parameters. Based on these properties, the experimental goals for the modular cavity program were:

- *Measurement of the safe operating gradient (SOG).* Designs of vacuum ionization cooling channel require limits on the breakdown rate allowed in cavities. The SOG is a measure of the cavity's stable operation, defined as the maximum accelerating gradient for which the breakdown rate does not exceed 1 spark in 10^5 RF pulses. One of the main goals of the modular cavity program is measuring the SOG for different external magnetic field values in a controlled environment.

- *Testing modular cavity as a realistic cavity model for ionization cooling channel.* Design of modular cavity was created as a model for future structures used in ionization cooling channel. Compared to previously built and tested at the MTA cavities, modular cavity is coupled to the power transmission waveguide via aperture coupling.

- *Tracking surface changes under high power operation in varying conditions.* Fast turnaround of the assembly and inspection processes allows for damage analysis to be performed after each run with fixed conditions. Tracking surface evolution in between runs allows for understanding the effect of run conditions (e.g. RF pulse length, magnetic field, repetition rate etc.) on the morphological properties of the surface.

- *Exploring the effect of different materials and geometries on RF breakdown.* The modular design opens the possibility of testing the effect of different materials on RF breakdown in otherwise identical conditions by swapping flat endwalls in between high-power

tests. Moreover, geometrical modifications to the cavity body, changing the RF gap length of the cavity are also possible. Varying the cavity's gap length allows to study the effect of impact energy of dark current electrons on RF breakdown.

- *Test the predictions of pulsed heating model.* Control over systematic errors and usage of different materials in high-power tests enable testing the predictions of the pulsed heating model of RF breakdown in strong magnetic fields, described in Section 2.3.

  The fundamental physics goal of the Modular Cavity program is to build the coherent picture, explaining the deterioration of accelerating gradient in strong magnetic field.

CHAPTER 3

RESULTS OF MODULAR CAVITY HIGH POWER TESTS

.

The goals of Modular Cavity experimental program were listed in Section 2.8.3. Time and resource constraints imposed the limitation on the amount of high power testing and variety of configurations the cavity was tested at. In this chapter, experimental results of high power tests of the Modular Cavity will be discussed.

3.1 Gradient performance of the Modular Cavity

Table 3.1 summarizes the safe operating gradients, measured with the two endplate materials on the Modular Cavity. Safe operating gradient (SOG) is defined as a maximum accelerating gradient for which the spark rate does not exceed 1 breakdown event per 10^5 RF pulses. The error bars on safe operating gradient incorporate the measurement error in the low-power RF calibrations. "Material" column refers to the materials of two endplate. For example, "Cu /Cu" refers to configuration with two copper endplates.

Table 3.1: Measured safe operating gradients in the Modular Cavity tests.

Material	**Magnetic field, T**	**Gradient, MV/m**
Cu / Cu	0	45.4 ± 0.3
Cu / Cu	3	12.9 ± 0.1
Be / Be	0	41.1 ± 2.5
Be / Be	3	49.8 ± 3.0
Be / Cu	3	10.1 ± 0.1

As discussed in section 2.7.1, the procedure of determining the safe operating gradient is based on the breakdown rate measurement. Table 3.2 shows the statistics for RF breakdown events accumulated at the safe operating gradient with different cavity configurations and external magnetic fields. It is important to note that requirement of accumulating 1 million RF pulses for SOG measurement was met for all listed tests.

Table 3.2: SOG statistics in the high power tests of the Modular Cavity.

Material	**Magnetic field, T**	**# of RF pulses**	**# of spark events**
Cu / Cu	0	1 M	15
Cu / Cu	3	1.5 M	12
Be / Be	0	1.1 M	12
Be / Be	3	3.3 M	6
Be / Cu	3	2.5 M	12

There are several notable results in gradient performance of the Modular Cavity that are discussed below.

- *Safe operating gradient of ∼50 MV/m in three tesla magnetic field with the beryllium endplate configuration.*

  The cavity demonstrated stable performance at the gradient of 49.8 ± 3.0 MV/m with the spark rate $\sim 2 \cdot 10^{-6}$. Testing the cavity at the higher gradients was limited by the RF source's output power.

- *Significant deterioration of SOG in three tesla magnetic field with copper endplate configuration compared to zero tesla.*

  Measured gradient of 12.9 ± 0.1 MV/m in three tesla field is a factor of 3.5 lower than the gradient achieved in zero tesla. This factor is higher than one measured in the other 805 MHz cavities (see section 2.2).

- *Deterioration of the stable operating gradient in three tesla field in "Cu / Cu" configuration with time.*

  Figure 3.1 demonstrates the history of the operating gradient during the three tesla run with copper endplates. After the initial ramp up sequence, the cavity ran stably at gradients ∼14 MV/m. Attempts to achieve higher gradients lead to the increased breakdown rate and the decrease in stable gradient. Final stable gradient at this portion of the run was below 12 MV/m.

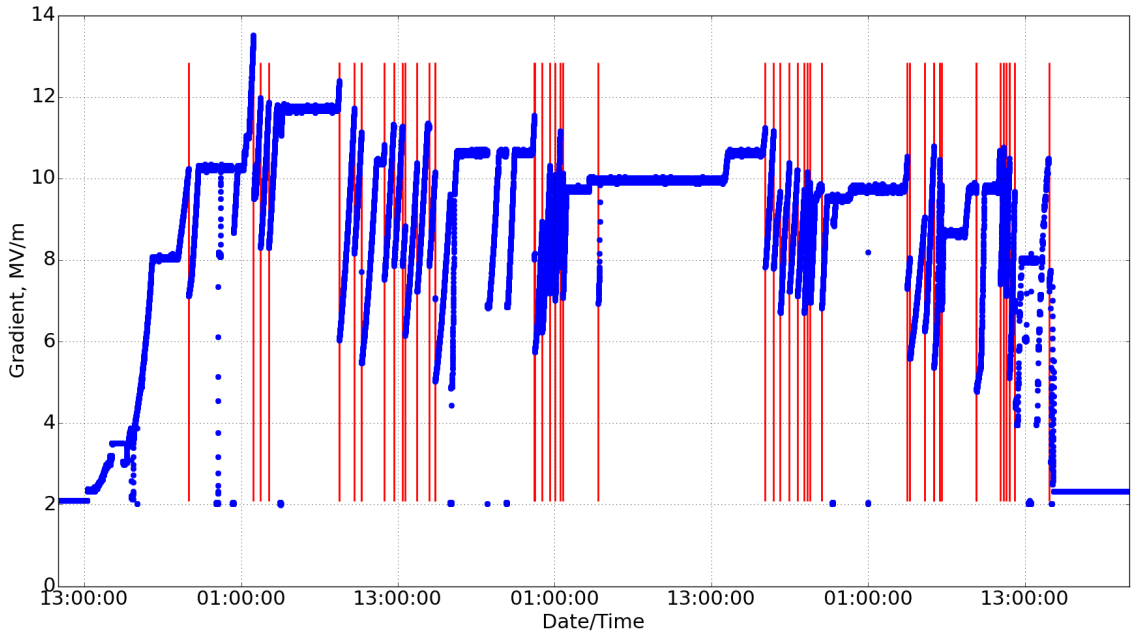

Figure 3.1: Gradient history of the "Cu / Cu" configuration in three tesla field. Breakdown events are denoted by vertical red lines.

- *Measured SOG of ∼10 MV/m in "hybrid Be /Cu" configuration.*

  This gradient performance is in line with the "Cu /Cu" runs of the Modular cavity. This suggests that the cavity's gradient performance is limited by the gradient performance of the copper endplate.

- Copper performance is zero tesla field is negatively affected by the three tesla operation.

  After the three tesla run, copper endplates were tested in zero tesla field again. Significant deterioration of the gradient performance was observed. Figure 3.2 demonstrates the gradient history of the Modular Cavity during 0 tesla operation. The total of 460 breakdown events was inflicted in 11 million RF pulses of operation. One can see that the cavity was conditioning over time - leading to higher achieved gradients. The final measured stable gradient is $\sim$ 22 MV/m, significantly lower than the SOG measured in the initial zero tesla tests.

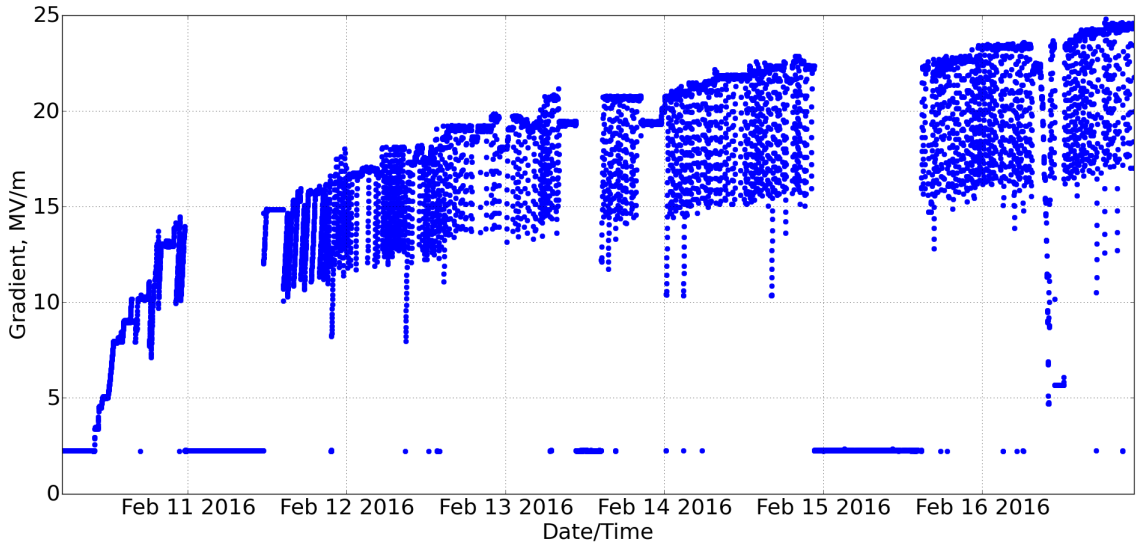

Figure 3.2: Gradient history of "Cu / Cu" configuration in 0 tesla "conditioning" run.

- *Modular avity demonstrated stable operation with beryllium endplates at the gradients above 50 MV/m in the range of magnetic fields between 0 and 3.5 tesla.*

  Last high power test with beryllium endplates featured collecting data at different gradients over the range of magnetic fields. Table 3.3 shows the statistics of RF breakdown events obtained at different gradients and magnetic fields. "X / Y" should be read as "X breakdown events in Y RF pulses". Time constraints did not allow for accumulating enough statistics for establishing the SOG. Note that the cavity was operating stably at gradients exceeding 50.7 ± 2.9 MV/m over the range of magnetic fields between 0 and 3.5 tesla .

Table 3.3: Breakdown statistics for operating beryllium endplates over the range of magnetic fields.

B, T	**50.7 MV/m**	**53.6 MV/m**
0	5/600k	4/50k
0.5	2/300k	0/50k
1	0/300k	0/50k
2	1/300k	0/30k
3.5	0/300k	0/50k

3.2 Surface inspection findings

Inspection of the inner surfaces was performed after each high power test of the Modular Cavity. Careful observation and cataloging of breakdown damage has enabled the set of the following observations about the effect of RF breakdown on the surface:

- *No breakdown damage was observed on the cylindrical cavity body, input coupler or anywhere on the inner surfaces outside of flat endwalls.*

  It can be concluded that all breakdown damage incurred on the inner surfaces of the flat endplates. This allows to discuss the surface inspection findings in the context of simple defined geometry and electromagnetic field profile in the region where the breakdown events are localized.

- *Breakdown damage on the copper endplates is categorically different in the presence of external magnetic field.*

  Figure 3.3 shows the typical breakdown damage traces observed after operating copper endplates in zero tesla field. Fractal-like structure on the left image represents the Lichtenberg figure, a typical pattern of branching electric discharges, often appearing in the insulating materials [110]. Thin 20 nm TiN layer on the inner surfaces of copper endplates provides the insulating medium for the Lichtenberg figure formation. The profilometry measurements of Lichtenberg-type damage revealed the characteristic depth differential less than 100 nm. Image on the right shows another prevailing type of damage observed on copper endplates after zero tesla field operation. Similarly to fractal-type structures, the characteristic transverse size of these features is hundreds of microns, depth differential is undetectable by available optical methods.

  Figure 3.4 shows examples of the typical damage incurred during operating copper endplates in three tesla field. Breakdown pits typically are round-shaped with diameter ranging from 0.8 mm to 1.5 mm. Image on the left shows an example of the pit that has a melted core in the middle, while pit on the right image is lacking the melted core

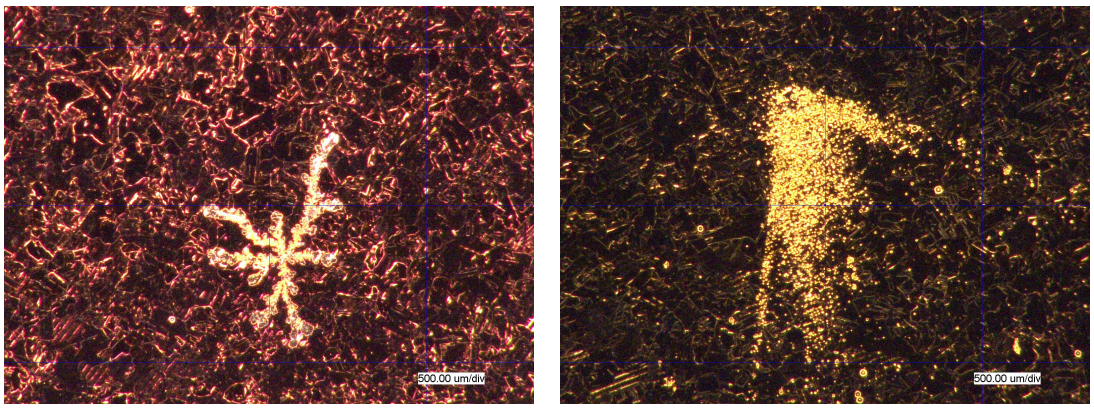

Figure 3.3: Examples of the typical damage after operating the Modular Cavity with copper endplates in zero tesla field. Dark background corresponds to TiN layer coating.

and is virtually flat (height differential is less than 100 nm). Diameter of the melted core can reach up to 1 mm.

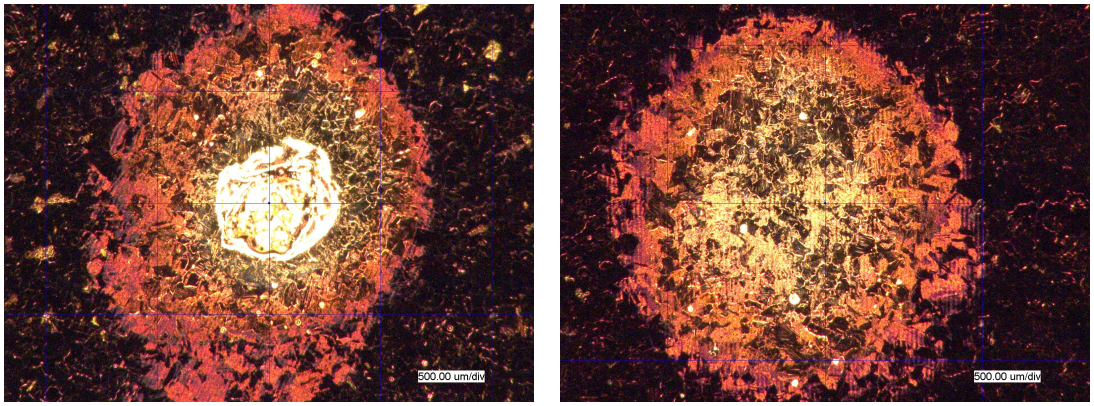

Figure 3.4: Typical breakdown damage after operating the Modular Cavity with copper endplates in three tesla field. Left - breakdown pit with the melted core in the middle. Right - "flat" breakdown pit.

An example of the melted core, also referred to as a "crater", is shown in Figure 3.5. The bottom of the melted core is out of focus on the left image, indicating its height difference with respect to the level of unscathed surface.

Capabilities of Laser 3D Microscope allow for profilometry analysis of the surface. The measurements show that the depth of the breakdown pits can reach up to 100 μm. Figure 3.6 shows an example of the height profile of the breakdown pit. Note the

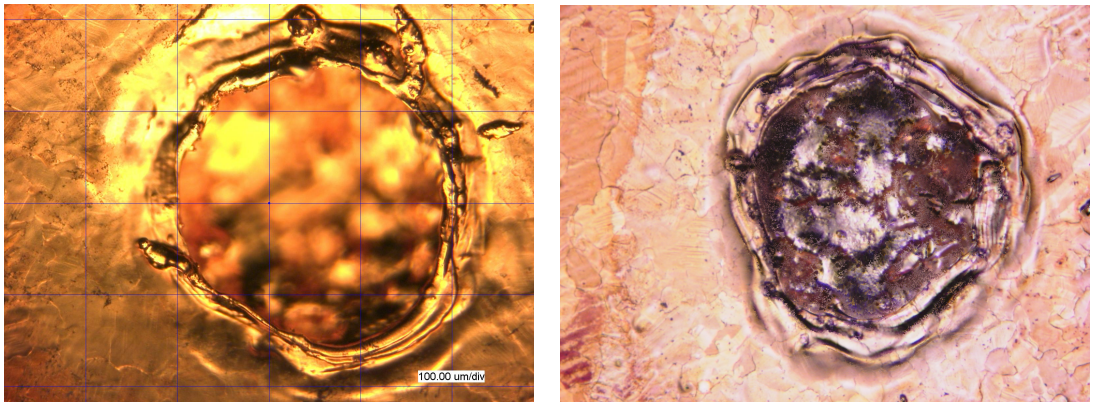

Figure 3.5: Example of the breakdown pit's melted core. The sharp edge of the core is visible on the left image. Right image shows the in-focus picture of the core's rough surface.

increased roughness of the surface around crater's rim and at the "bottom" of the crater due to non-uniformity in the solidification process. Typical measured roughness of undamaged surface is $R_a \approx 0.1 - 0.4$ μm. Typical roughness in the melted material region is $1.0 - 2.4 \mu$m. Estimation of the energy, required to melt the equivalent amount of material can be made. Taking the maximum observed radius of the core $r \sim 500$ μm, and depth $d \sim 100$ μm, the required melting energy is ~ 0.1 joules, a fraction of stored energy within the cavity. Cavity, operated at the typical gradient for three tesla run G = 12 MV/m, has the peak stored energy E = 1.2 joules.

- *Breakdown damage incurred in three tesla field features microscopic splashing of melted copper.*

  "Violent" nature of the damage in magnetic field features crater-like damage, where copper is melted and extracted from the pits by the breakdown arc. Example of such splashing is shown in Figure 3.4. Driven by plasma forces in the breakdown arc, melted droplets land on the surface region that surrounds the breakdown pits' locations. The evidence of observed copper splashing is presented in Figure 3.7. Droplets and splashes of copper are typically dozen of microns wide and several microns tall. Estimated field enhancement factor of individual droplet can reach up to $\beta_e = 3$. No evidence of copper

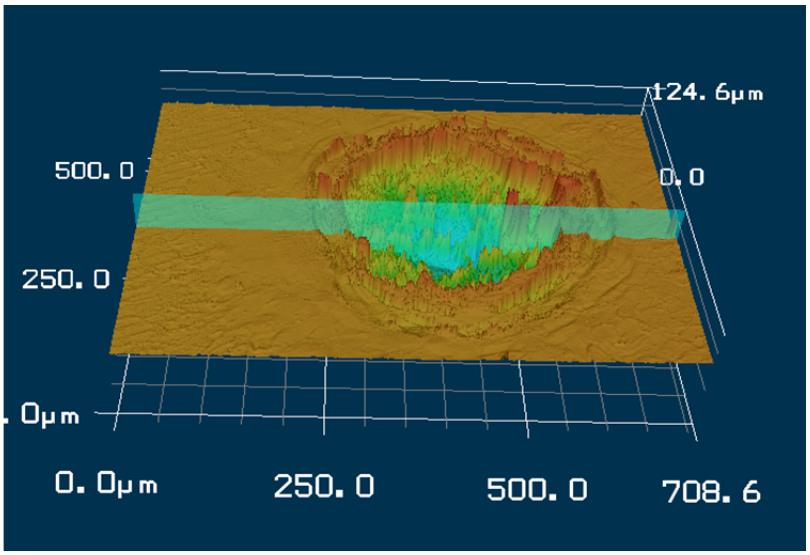

(a)

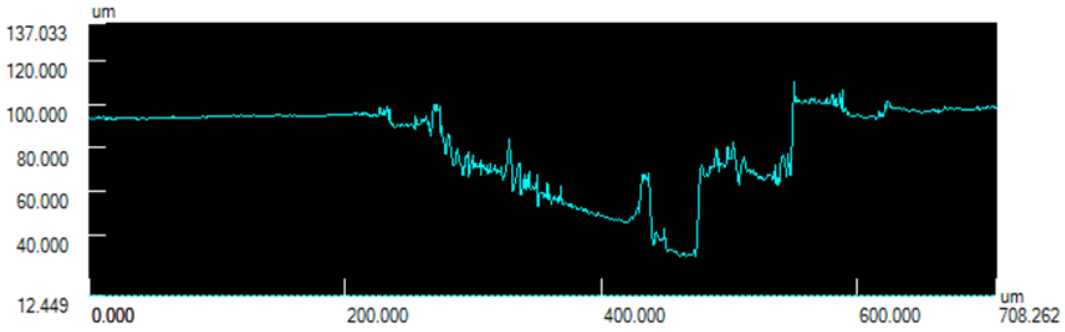

(b)

Figure 3.6: Height profile of the breakdown pit incurred during three tesla operation on the copper surface. (a) - reconstructed 3D image, (b) - height profile along the imaginary vertical cutoff shown in (a).

splashing was found after operation in zero tesla field.

- *Mismatch between the number of the detected sparks and the number of observed breakdown pits in three tesla copper tests.* 55 breakdown events were registered during the high power tests of copper endplates. 168 breakdown pits on each endplate were documented during the surface inspection.

- *Copper splashes incurred during three tesla operation are processed out in zero tesla conditioning.*

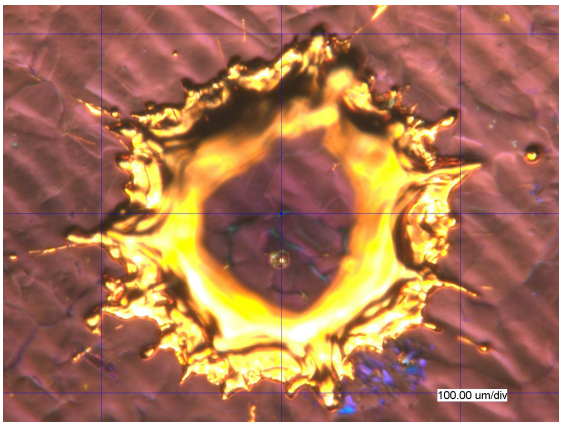

(a)

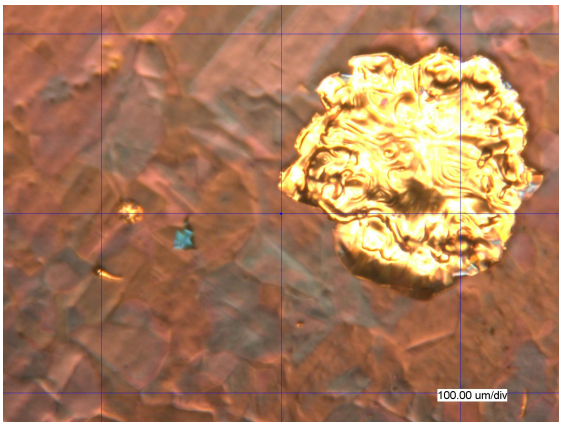

(b)

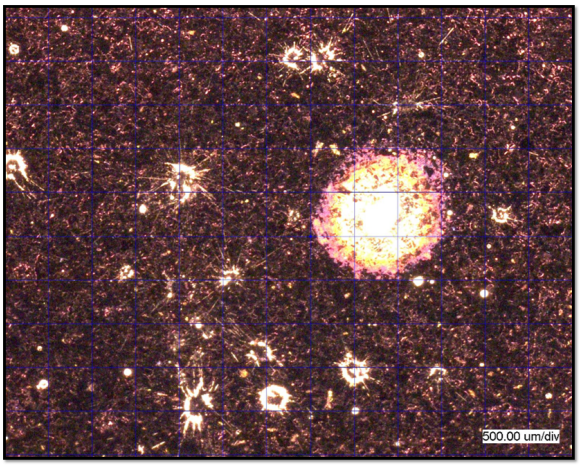

(c)

Figure 3.7: Splashing of molten copper after operation in three tesla magnetic field. (a), (b) - typical shapes of copper droplets deposited on top of TiN layer on the copper endplate. (c) - an example distribution of splashing traces in the vicinity of the breakdown pits' location.

Copper endplates were operated in zero tesla field right after the three tesla run. Surface inspection revealed that some of the copper splashing traces incurred during three tesla run were processed out in zero tesla operation. Figure 3.8 shows an example of this phenomenon.

- *Perfect one-to-one correspondence between breakdown damage sites on opposite copper endplates after three tesla operation.* We observed that each breakdown pit incurred during three tesla run has a corresponding pit on the opposite side of the cavity, as demonstrated in Figure 3.9. No correlation between damage on opposing plates was

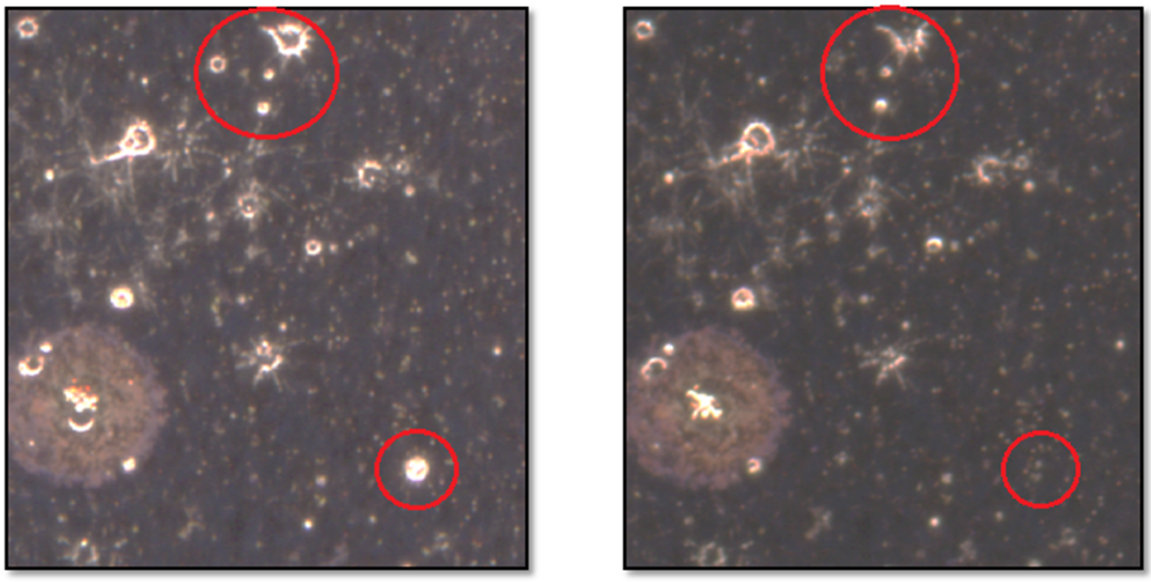

Figure 3.8: Evaporation of copper splashing traces during zero tesla operation. Left - snapshot of surface state after the three tesla run. Right - the same surface region after subsequent zero tesla test. Red circles highlight the regions where the changes are most evident.

found after zero tesla operation.

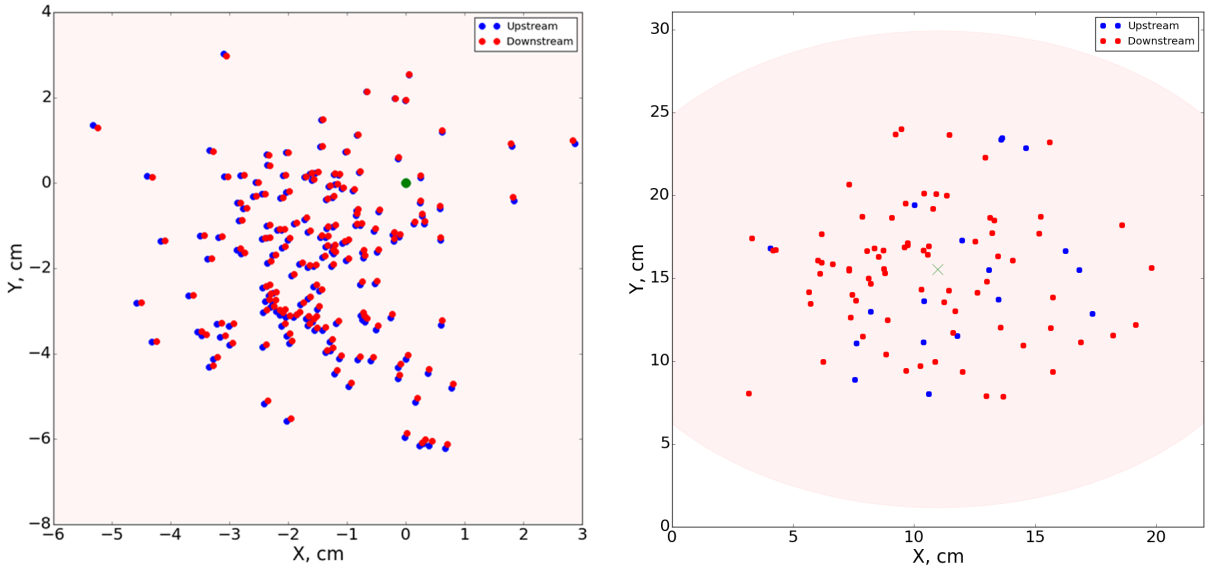

Figure 3.9: Map of the breakdown damage on the copper endplates in three tesla field operation (left) and zero tesla field operation (right). Locations are color-coded: red and blue dots indicate opposite walls. Zero tesla damage map is represented by the Lichtenberg figures distribution. The center of the endplates is marked in green.

- *Damage incurred in zero tesla field on copper walls spreads more uniformly and over a larger surface area compared to the damage incurred in three tesla.*

  As can be seen from Figure 3.9, damage incurred in three tesla is clustered around the center of the endplate where the electric field is highest. At the same time, damage incurred in zero tesla operation spreads out more and covers a larger surface area. Figure 3.10 highlights this by showing the histogram of the damage density per unit area for damage in zero tesla and three tesla.

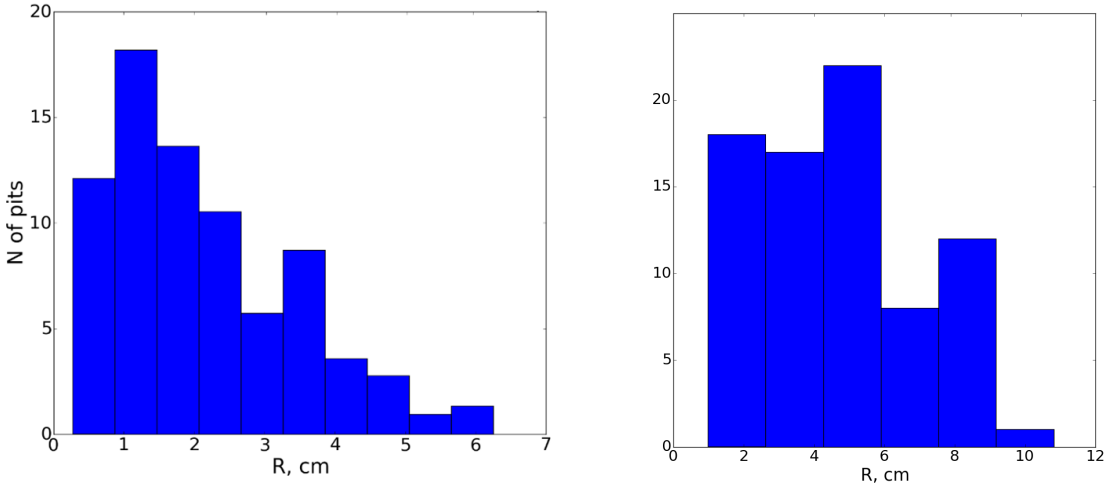

Figure 3.10: Radial distribution of breakdown damage density in three tesla field (left) and zero tesla field (right).

- *Breakdown damage on beryllium plates operated in zero tesla is similar to the damage observed on copper endplates operated in zero tesla.*

  Two dominant types of damage were observed after operating beryllium in zero magnetic field, as shown in Figure 3.11. Similar to the damage incurred in copper in zero tesla, Lichtenberg figures are the prominent occurrence. The second type of common damage can be described as a cluster of dots of exposed metal. Also similar to copper, no correlation between damage distributions on opposing endplates was found.

- *Beryllium endplates incurred no damage when operated in three tesla magnetic field.*

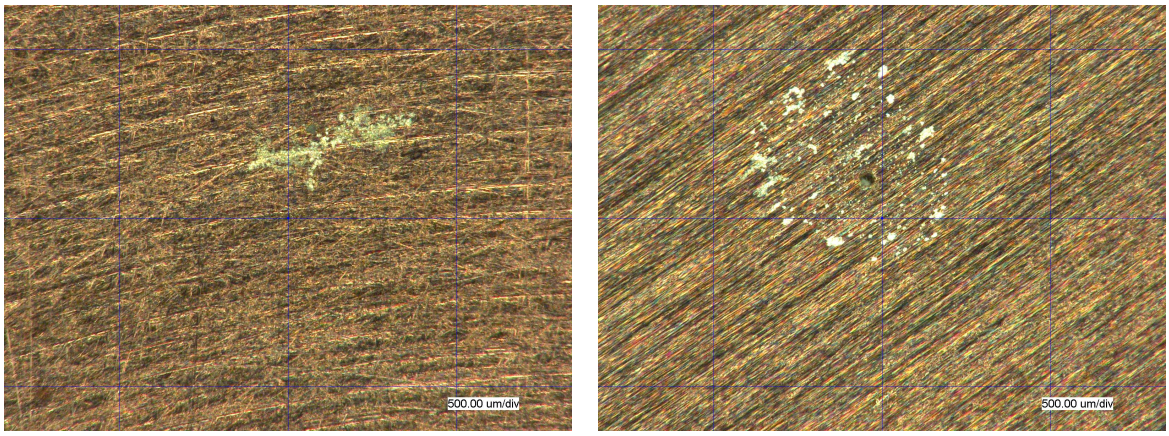

Figure 3.11: Example of the typical breakdown damage types found on beryllium endplates operated in zero tesla field.

41 breakdown events were detected by run control system during operating beryllium endplates in three tesla field. However, microscopic surface inspection revealed no new damage features. No conclusions can be made about sub-microscopic damage, as SEM inspection of the endplates was not possible in-between the high power tests.

- *Copper droplets can traverse the RF gap of the cavity in three tesla magnetic field.* Solidified copper droplets were found on beryllium endplate after operating "Be / Cu" configuration in 3 tesla magnetic field. Figure 3.12 demonstrates an example of an observed copper droplet. One can see that melted material is deposited on top of the flat beryllium surface coated with the TiN layer. It is important to point out that opposing copper endplate is the only realistic location for the droplet to originate from.

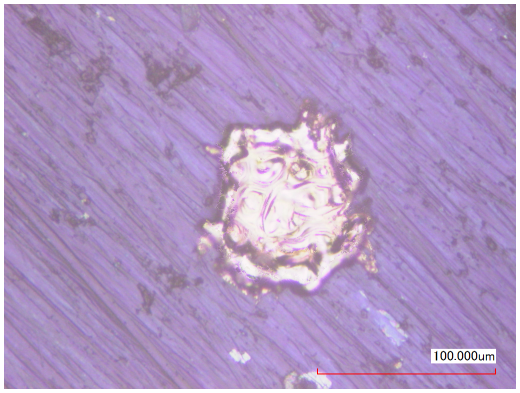

(a)

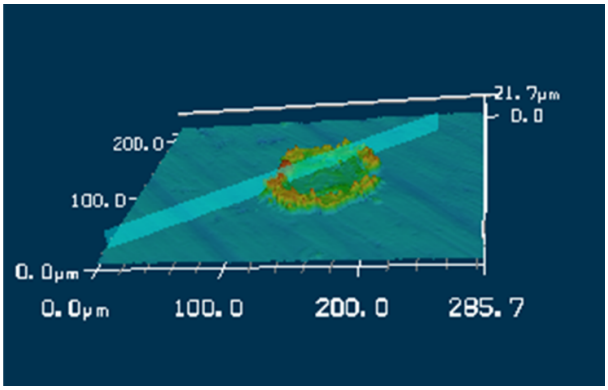

(b)

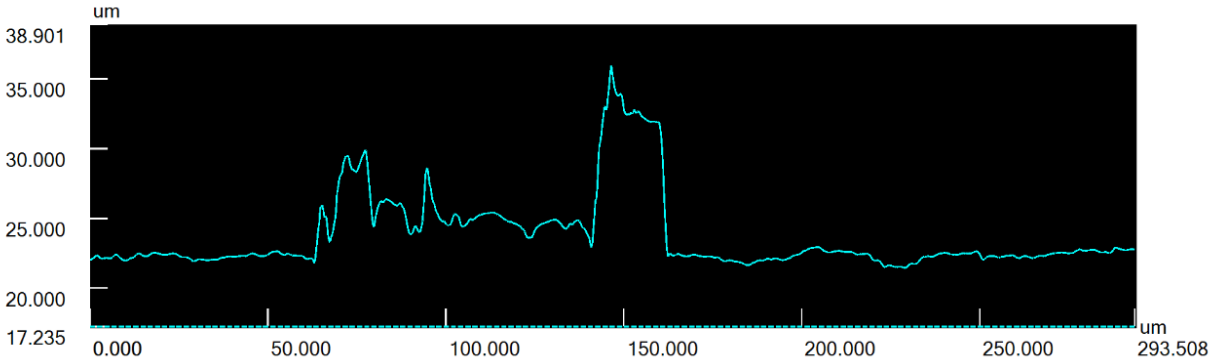

(c)

Figure 3.12: Characterization of a copper droplet observed on the beryllium endplate after operating the Modular Cavity's "Be / Cu" configuration in three tesla magnetic field. (a) - micrograph of the copper droplet on beryllium surface. (b) - reconstructed 3D image of the droplet region. (c) - height profile of the droplet surface.

CHAPTER 4

THE PULSED HEATING MODEL OF RF BREAKDOWN IN STRONG MAGNETIC FIELD

Proposed by Robert Palmer *et al.* in [86], the pulsed heating mechanism is the first attempt to quantitatively explain the deterioration of surface gradient in external focusing magnetic fields. Their work was motivated by the previous experiments in the MTA, which demonstrated the deterioration of cavities' gradient performance in external magnetic fields [87]. In this chapter, the model of pulsed heating will be developed further. The model will also be adjusted for the geometry and run conditions of the Modular Cavity. The goal of this work is to obtain the gradient predictions for copper, beryllium and aluminum endplate materials in the external magnetic field. The choice of three materials is dictated by the experimental data, obtained for beryllium and copper endplates in the Modular Cavity tests, and also potential interest in the aluminum as a candidate material for cavity designs [88].

Most models of RF breakdown assume that the electron field emission from the local surface area acts as an initiation stage of RF breakdown (see section 1.5.4). Surface defects, which can be in the shape of sharp needle-like tips, surface micro-cracks, or other type of asperities, create a condition for the enhanced electric field region. According to the Fowler-Nordheim approximation, enhanced local electric field leads to the exponentially increased emission of electrons from the surface, called dark current. Placed in the external focusing magnetic field, dark current is focused into so-called beamlets that impact on the opposing surfaces within the cavity volume and lead to the heating of local surface area. This local temperature rise under certain conditions can be high enough to cause the permanent damage on the surface and, thus, eventually lead to the initiation of RF breakdown. The purpose of the pulsed heating model is to study the critical conditions for the local temperature rise, which will enable making predictions for the maximum stable gradient in the range of external magnetic fields.

Modeling the pulsed heating mechanism could be divided into five stages:

- Simulation of the electron field emission from the surface defect.
- Electron beam tracking across the RF gap of the cavity.
- Energy deposition by the impacting on the surface dark current beam.
- Numerical solution of the heat equation for the local temperature rise.
- Translating local temperature rise to the threshold gradient.

In this chapter of my thesis, I will go over each of the 5 stages in detail.

4.1 Simulation of the electron field emission from the surface defect

Direct dark current measurements demonstrate that intensity of electron dark current sharply increases right before the breakdown event [89]. Similar conclusion could be drawn from the X-ray measurements in the high power tests of the Modular Cavity. Figure 4.1 shows an example of the typical breakdown event in three tesla. One can see on the image on the right that the radiation activity is spiked within 1 microsecond before the breakdown discharge. These observations suggest that the dark current plays a crucial part in the initiation stage of RF breakdown.

Surface damage studies demonstrate that different emitters activate on the surface during high power testing; possible mechanisms of emitters' creation, evolution and destruction are discussed in several works [90, 91]. The mechanism of field emission under electric field is described by a Fowler-Nordheim formula, which considers a quantum tunneling of electrons through the potential barrier near the surface of the metal. The electron current density can be expressed in the following form:

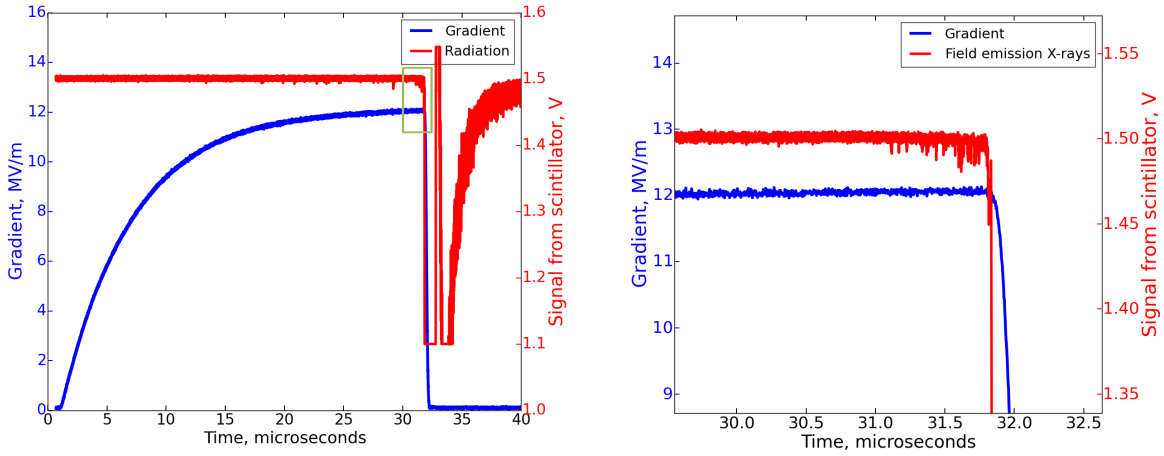

Figure 4.1: Typical breakdown event during the Modular Cavity's high power testing with copper endplates (left) and zoom-in on the breakdown initiation time window (right). Red trace corresponds to the signal from the X-ray scintillator counter, positioned along the cavity main axis; blue trace corresponds to the envelope of the RF pickup signal. Saturation of PMT tube is responsible for the vertical spike in the radiation signal around $t = 33$ μs and can be neglected.

$$J(G_s, \beta) = \frac{A_{FN}(\beta G_s)^2}{\phi} \exp\Big(-\frac{B_{FN}\phi^{1.5}}{\beta G_s}\Big) \tag{4.1}$$

where G_s is the surface field gradient in MV/m, β is the field enhancement factor, defined as the ratio of maximum gradient on the emitter tip to the average surface gradient, ϕ is the work function of the metal expressed in eV, $A_{FN} = 1.54 \times 10^6$ A eV/(MV)^2, $B_{FN} = 6.8 \times 10^3$ MV/m (eV)$^{1.5}$. Following this formalism, we can define G_{total}, the maximum electric field value at the tip of the emitter as $G_{total} = \beta G_{surf}$. Given the current density $J(G_s, \beta)$, total dark current from the emitter can be calculated as $I(G_s, \beta) = A_{emit} \cdot J(G_s, \beta)$, where A_{emit} is the effective surface area of the emitter.

The detailed dark current studies allow to estimate the geometrical parameters of the emitters. MTA's multicell experiment demonstrated that total electron emission from the active surfaces at a given time is dominated by the single emitter with the highest beta [38]. Indeed, the power dependence in Fowler-Nordheim formula weights the data heavily towards

the highest β asperities. Equation 4.2 directly follows from Fowler-Nordheim formula:

$$\frac{d\ log_{10}(I_{FN}/G^{2.5})}{d\ (1/G)} = -\frac{2.8 \times 10^9\ \phi^{1.5}}{\beta} \tag{4.2}$$

, where I_{FN} is the total emission current, β is the total field enhancement factor. As the work function of material is assumed to be known and the average surface gradient can be measured, Equation 4.2 suggests that β can be calculated as a slope on the log plot of the left hand-side . Similarly, the effective emitting surface area of the asperity A_{emit} can be calculated according to Equation 4.3:

$$log_{10}(I_{FN}/G^2)_{G\to\infty} = log_{10}\Big(\frac{1.54 \times 10^{-6}\ A_{emit}\ \beta^2\ 10^{4.52\phi^{-0.5}}}{\phi}\Big) \tag{4.3}$$

In addition to the field-assisted electron tunneling, thermal-assisted emission can be considered [94]. The expression for current density in thermal-assisted emission takes the form:

$$J(T) = A_G\ T^2 \exp\Big(-\frac{\phi}{kT}\Big) \tag{4.4}$$

, where material-dependent coefficient A_G is in the order of 10^6 $\mathrm{A \cdot m^{-2}\ K^{-2}}$, k is the Boltzmanns' constant, T is the surface temperature, and ϕ is the work function of metal. However, for temperatures lower than several thousand kelvin, field-assisted emission dominates thermal emission. Typical temperature rise induced by ohmic RF surface heating at gradients $10 - 50$ MV/m does not exceed 20 K.

Previous microscopic studies of the structures tested in high power RF fields revealed sharp, cone- or needle-like metal whiskers on the surface. In particular, MTA's 805 MHz multicell cavity experiment conducted a surface study of the iris area [38]. Sharp protrusions, better described as hair-shaped structures with corresponding field enhancement factors up to several hundred, were observed lying on the metal surface. Metal whiskers of varying dimensions were also observed under strong electrostatic and RF fields in other

experiments [92]. Instrumentation on the multicell experiment allowed for the measurements of the dark current. Important for this model, the range of typical field enhancement factors was measured. Figure 4.2 shows several measurements of β_{total} as the cavity was undergoing high-power conditioning sequence. It is important to note that measured value of field enhancement factor converges to $\beta_{total} \simeq 400$. Typical values of dark current measured in the experiment were in the order 100 mA, which corresponds to the effective emitting area of 10^{-14} m^2.

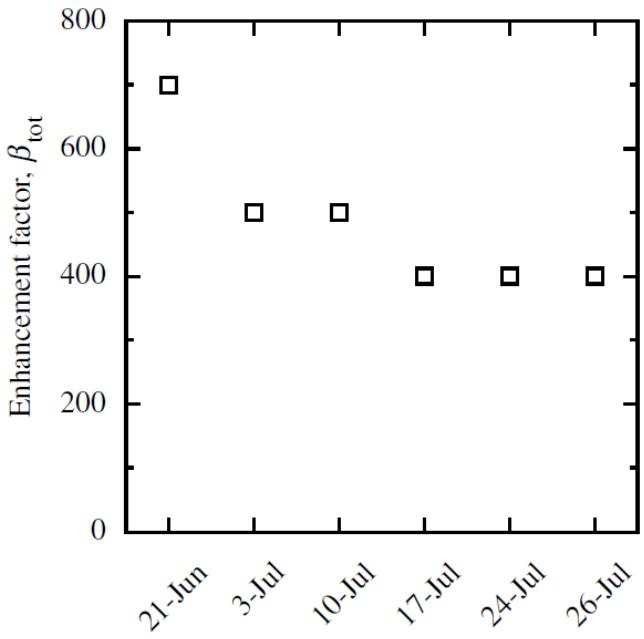

Figure 4.2: Field enhancement factors measured in the MTA's 805 MHz multicell cavity experiment [38].

In this model, I consider individual emitter shaped as a prolate spheroid. By varying dimensions of the spheroid, it is possible to model the needle-like sharp structures with any field enhancement factor β. Additional benefit of this approach is that it allows to find the precise analytical solution for the electric field around asperity without involving complex simulation tools. Wolfram Mathematica package was used in building the model for field emission, electron trajectory tracking and heat equation solving [93]. This was a collaborated effort with Alvin Tollestrup and Diktys Stratakis, scientists at Fermi National laboratory.

To calculate field emission parameters from prolate spheroid-shape asperity, one need to start with calculating the potential on its surface. Assuming h and a are corresponding major and minor axes of the spheroid and G_{surf} is the average surface gradient, potential can be expressed as [95]:

$$V(G_{surf}, z, r) = G_{surf}\ z \left(1 - \frac{coth^{-1}\big[y(z,r)\big] - \frac{1}{y(z,r)}}{c_2}\right) \tag{4.5}$$

, where $y(z,r)$ and c_2 are defined as:

$$\begin{gathered} c_2 = coth^{-1}\big[\eta_0(r,z)\big] - \frac{1}{\eta_0(r,z)} \\ y(z,r) = \Big(1/2\ (1 + (z/c_1)^2 + (r/c_1)^2 + \sqrt{(1 + (z/c_1)^2 + (r/c_1)^2)^2 - 4(z/c_1)^2}\Big)^{1/2} \\ c_1 = h\sqrt{1 - (a/h)^2} \\ \eta_0(r,z) = h/c_1 = \frac{1}{\sqrt{1 - (a/h)^2}} \end{gathered} \tag{4.6}$$

$\eta_0(r,z)$ and $y(r,z)$ are defined to be spheroidal coordinates. It is now possible to calculate the $z-$ and $r-$ components of the electric field near asperity:

$$\begin{gathered} G_z(z,r) = \frac{dV(z,r)}{dz} \\ G_r(z,r) = \frac{dV(z,r)}{dr} \\ G_n(z,r) = \sqrt{G_z(z,r)^2 + G_r(z,r)^2} \end{gathered} \tag{4.7}$$

$G_n(z,r)$ denotes the electric field component, normal to the surface of the emitter. $G_n(r,z)$ is a useful quantity that will be used for calculation of the total emitted current and emission area, according to Equations 4.2 4.3.

In this work, I will be used an extended form of the Fowler-Norheim's field emission expression, offered in [96]:

$$J = A_{FN}\ \frac{G^2}{t(y)\ \phi} \exp\Big(- B_{FN}\ \phi^{1.5}\ v(y)/G\Big) \tag{4.8}$$

where J is the current density, expressed in A/cm^2, A_{FN} and B_{FN} are the constants defined earlier in this Section, G is the surface gradient expressed in MV/m, and $y = 0.0362{\times}G^{1/2}/\phi$. The first part of the equation describes the flux of electrons coming from inside to the surface of the metal. The exponential part of the equation describes the probability of electron to penetrate under the potential barrier of the surface. As function $t(y)$ affects the value of the current density by only a few percent, it is often approximated by unity. Function $v(y)$, however, is included in the exponent and, therefore, its contribution can not be neglected. The extended expression for $v(y)$ is given in [97] and in the short form can be written as:

$$v(y) = 1 - 0.143y - 0.885y^2 \tag{4.9}$$

Figure 4.3 shows the functions $v(y)$ and $t(y)$.

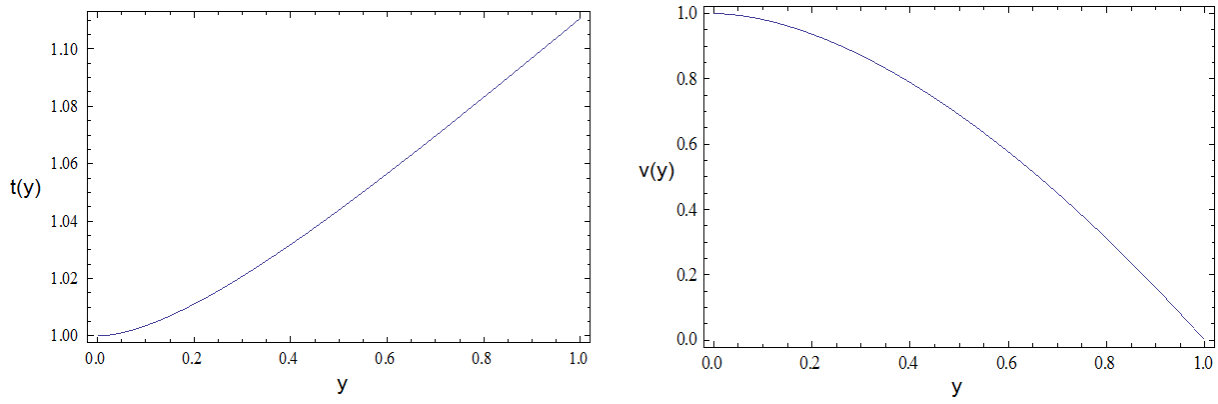

Figure 4.3: Functions $v(y)$ and $t(y)$ in the extended form of Fowler-Nordheim equation [96].

Combining 4.8 and 4.9, the expression for the current density becomes:

$$J\big(\phi, G_n(r,z)\big) = \frac{A_{FN}}{\phi}\ G_n(z,r)^2\ \exp\left(- \frac{B_{FN}\ \phi^{1.5}\ v(y)}{G_n(r,z)} \right) \tag{4.10}$$

Table 4.1 summarizes the parameters used in the field emission modeling.

Table 4.1: List of parameters use in the field emission model.

Parameter	**Value**
A_{FN}	1.54×10^6 A $\cdot$ eV/(MV)^2
B_{FN}	6.8×10^3 MV/m $\cdot$ (eV)$^{3/2}$
ϕ (Copper)	4.4 eV
ϕ (Beryllium)	5.0 eV
ϕ (Aluminum)	4.0 eV
h	62 μm
a	1.77 μm

The metal work function ϕ significantly affects the current density, as it is present in both electron flux and potential barrier parts of the Fowler-Nordheim Equation 4.10. Traditionally, experimental measurements of work function are conducted by the photon spectroscopy or thermionic emission methods. The downside of these methods is that they average the value of the work function over large surface area. This area might contain multiple surface imperfections. As total field emission current from the surface is dominated by a single emitter, it is important to understand how the metal work function depends on the geometry of the asperity under extreme high field condition. Modern methods of the density functional theory enabled precise calculation of the work function around contaminants and intrinsic surface defects. It was shown that the work function for copper can deviate as much as 10% from average in sharp surface geometries [98]. In this model, I will be using experimentally measured values of work function for smooth metal surfaces, listed in Table 4.1.

Following the formalism in [66], the emitter dimensions were chosen to best fit to the measured values of field emission in MTA's multicell experiment. Choosing $a = 1.77$ μm and $h = 62$ μm gives the total field enhancement factor of $\beta = 385$, which agrees well with the experimentally measured values in Figure 4.2. Figure 4.4 shows the geometry of the emitter used in simulations. Figure 4.5 shows the axial dependence of r- and z-components of the electric field along the surface of the emitter, calculated according to Equation 4.7 at a radius of $r = 0.1$ μm for the accelerating gradient of $G = 30$ MV/m. Note that the radial component of the field nearly linearly increases to the maximum value at the tip of

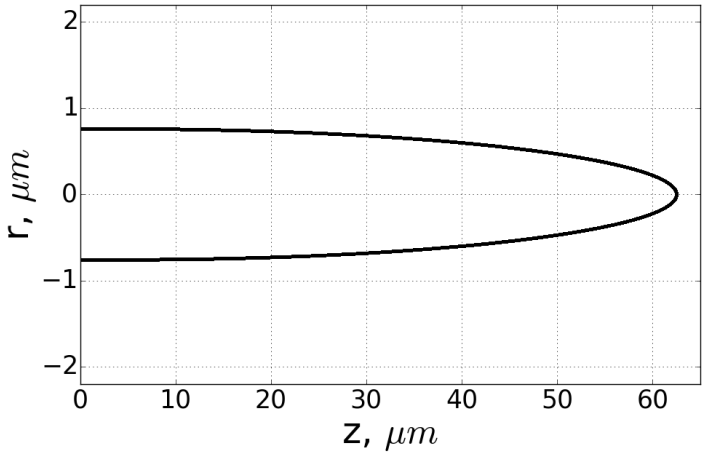

Figure 4.4: Geometry of the individual emitter, following the emitter dimensions in [66].

the emitter ($z = 62$ μm) and then drops quickly outside of the emitter surface. The axial component is virtually negligible anywhere except for the emitter tip ($z > 61$ μm), where the field enhancement factor is the highest.

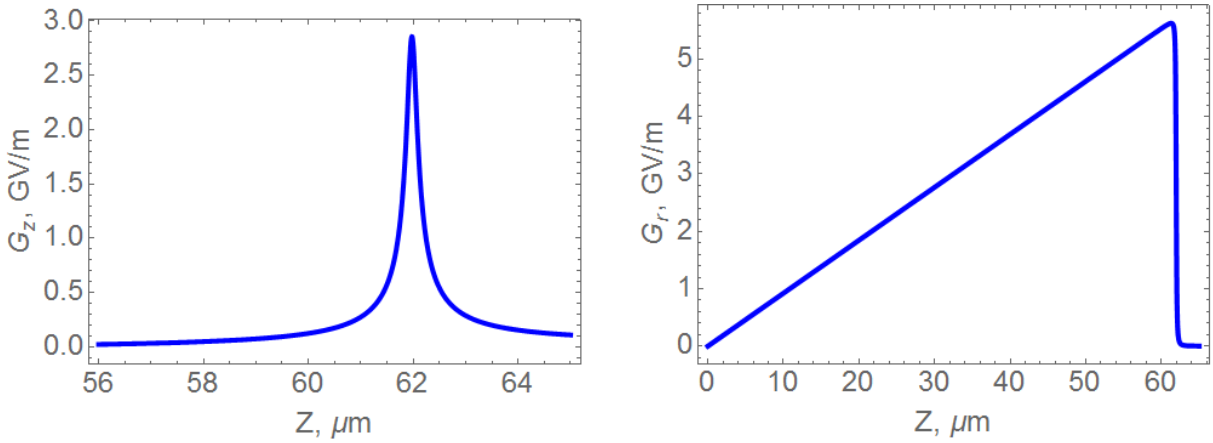

Figure 4.5: Z-component (left) and r-component (right) of the electric field around prolate spheroidal emitter with $h = 62$ μm and $a = 1.77$ μm, calculated at a radius of 0.1 μm for accelerating gradient of 30 MV/m.

Figure 4.6 shows the behavior of the radial component of electric field around the emitter. One can see that the radial electric field is relatively low at the "base" of the asperity. At the same time, due to axial symmetry, the radial component decreases when very close to the emitter tip. Thus, 61.5 μm curve, that corresponds to the region close to the tip, is

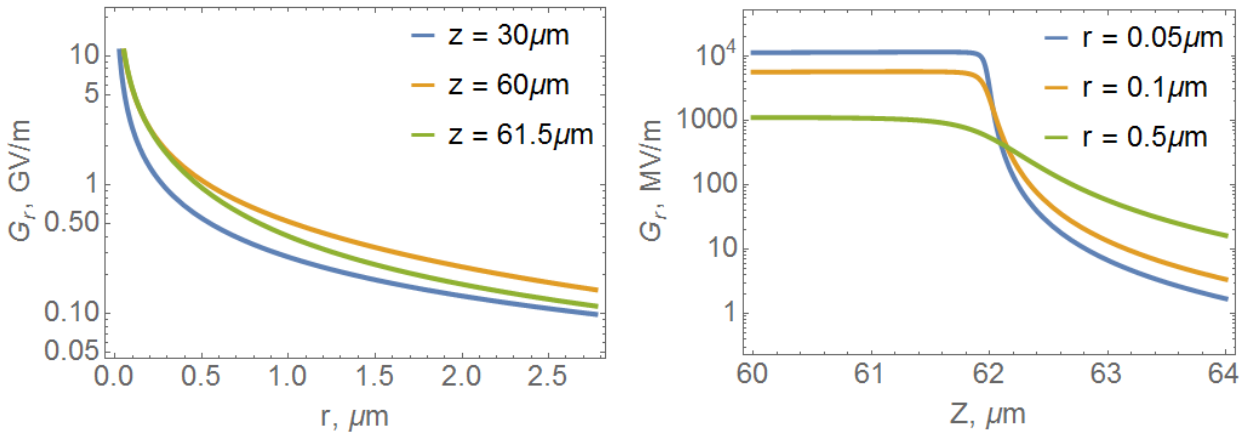

Figure 4.6: Radial electric field component around prolate spheroidal emitter. Left - radial dependence, right - axial dependence.

trending lower than 60 μm curve on the left diagram. Similarly, $r = 0.5$ μm is surpassing $r = 0.1$ μm on the right graph. Note that both G_r and G_z exhibit the $1/r$ asymptotic trend in the region outside of the emitter.

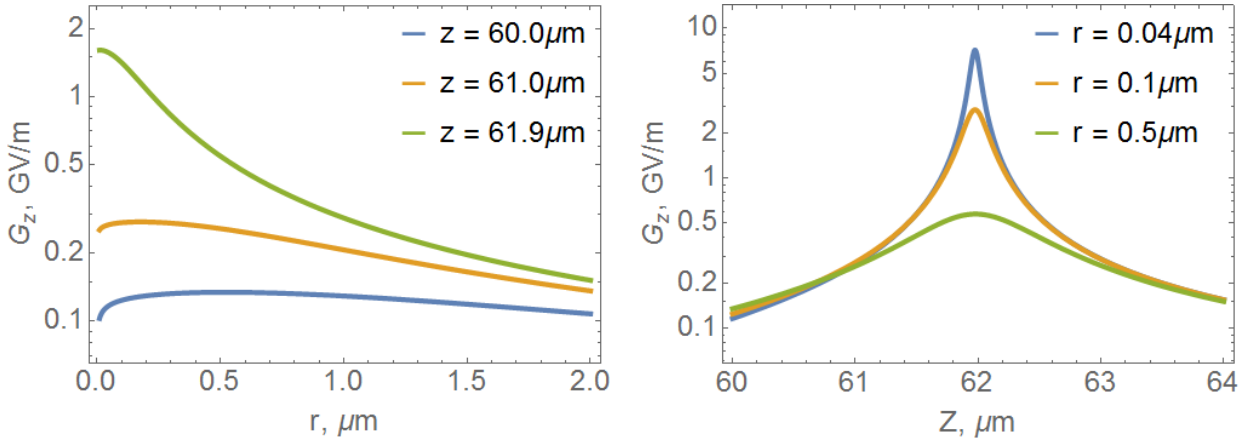

Figure 4.7: Axial electric field component around the prolate spheroidal emitter. Left - radial dependence, right - axial dependence.

Figure 4.7 shows the behavior of the axial component. Note the strong field enhancement in the region near the tip of the emitter. As expected, value of axial field goes down with the radius, as the radial component dominates in the region away from the tip.

Using the geometrical relation for the spheroid, $z = h\sqrt{1 - \left(\frac{r}{a}\right)^2}$, total electric field

G_n, normal to the emitter's surface at any point, can be calculated as:

$$G_n(r) = G_n\left(h\sqrt{1-\left(\frac{r}{a}\right)^2}, r \right) \tag{4.11}$$

Figure 4.8 shows the calculated $G_n(r)$ dependence for copper in 30 MV/m accelerating gradient. The peak field at $r = 0$ μm is $G_{peak} = 11.55$ GV/m, which corresponds to the field enhancement factor of $\beta = 385$.

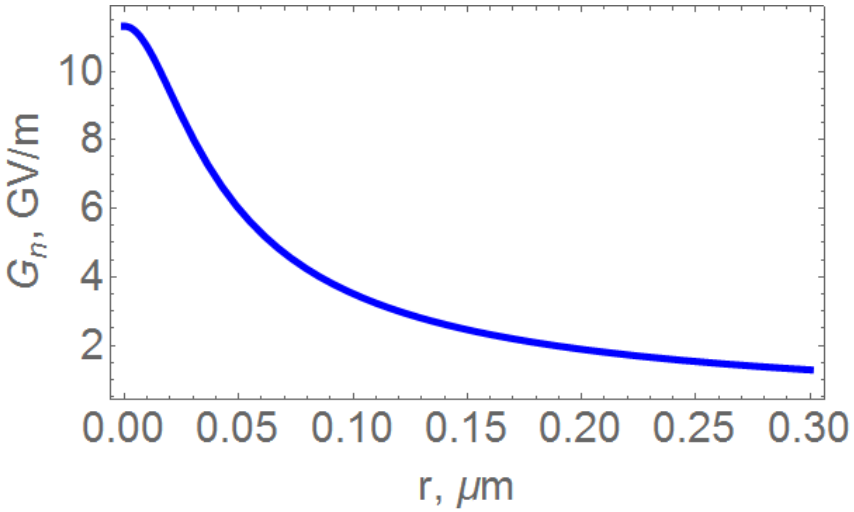

Figure 4.8: Normal electric field G_n, calculated along the emitter's surface.

Figure 4.9 shows the dark current density dependence on the radius of the emitting spot. Notice the logarithmic vertical scale - emission current falls off quickly with the radius, as expected from the Fowler-Nordheim formula. The total emission current can be calculates as:

$$I = \int_0^r J(R)\, dS \tag{4.12}$$

where dS is the surface area element calculated as $dS = 2\pi R\, dR$. Figure 4.11 shows the calculated total current dependence on the radius of integration r. It is important to note that the emission current gets saturated for radius exceeding $r \simeq 0.06$ μm. This makes the the effective emission area of the asperity of the order of $10^{-13} - 10^{-14}$ μm^2. That value

is consistent with the experimental findings in MTA's 805 MHz multicell cavity, where the total measured dark current at the gradient's range of $30 - 35$ MV/m was $I_{meas} = 100$ mA.

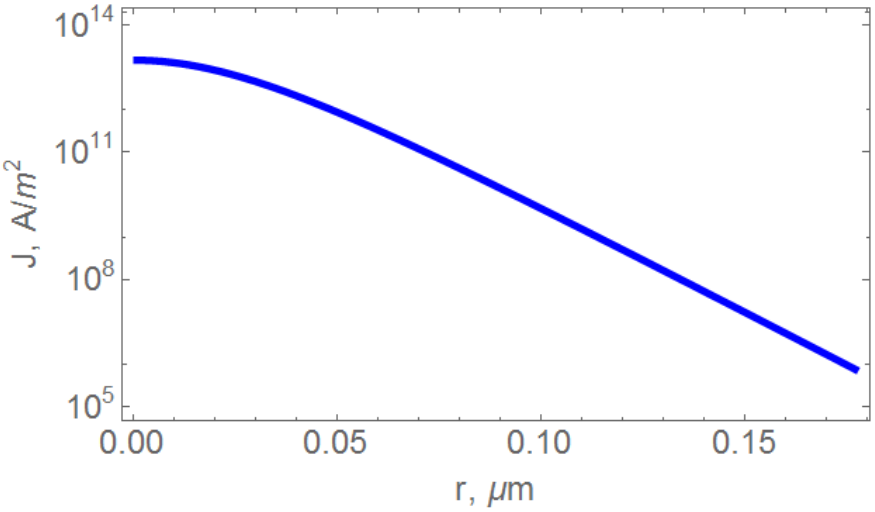

Figure 4.9: Current density dependence on the radius of the emitting spot.

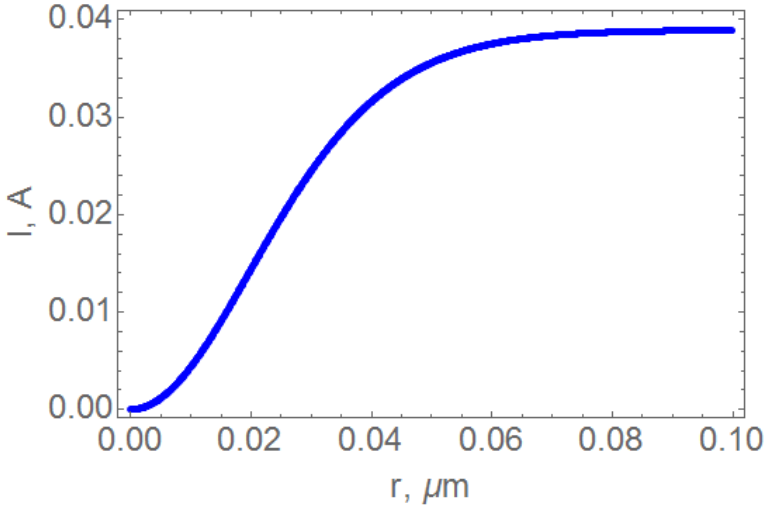

Figure 4.10: Total emission current at 30 MV/m accelerating gradient, calculated as $I = \int_0^r J(R)\, 2\pi R\, dR$.

Figure 4.11 shows the total dark current dependence on the surface gradient. Note that the total dark current increases by 3 orders of magnitude between G = 20 MV/m and G = 50MV/m.

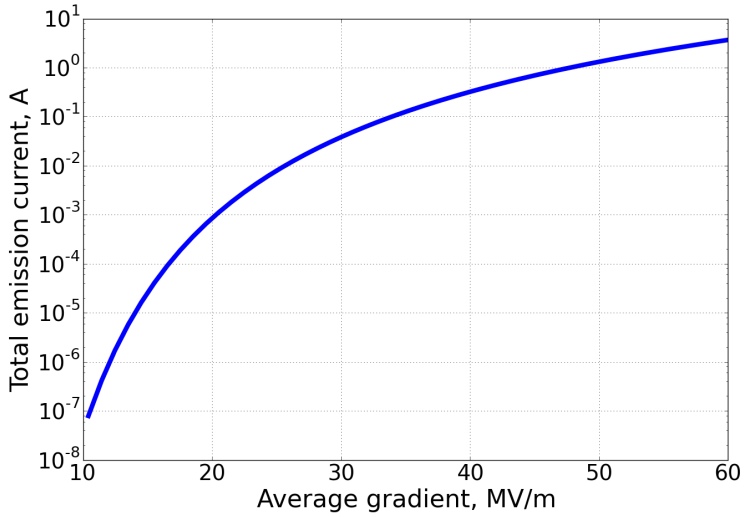

Figure 4.11: Total emission current as a function of the surface gradient.

4.2 Electron beam tracking across the RF gap of the cavity

.

To estimate the energy deposition by the dark current beam on the opposing endplate, one needs to calculate the transverse size of the beam and the total current, carried by the beam. As the dark current electrons leave the field enhancement region around asperity, their motion is fully determined by their interaction with the cavity RF fields, external magnetic field and particle-particle interaction within the beam.

Modular Cavity has near perfect pillbox geometry - the cylinder of radius $R = 10.44$ cm and the length $L = 14.22$ cm. The only disruption to the ideal pillbox approximation is the coupling input near the top of the cavity body. In order to model the RF fields inside the cavity volume, one needs to verify that such disruption is minor and does not significantly deviate from the pillbox approximation.

To compare the field distribution in the actual geometry to that of an ideal pillbox, realistic modular cavity geometry was implemented in the Cubit suite [99]. Cubit is a software package, developed at Sandia National Laboratory that allows geometrical modeling of three-dimensional finite element meshes. Cubit enables meshing with varying in size tetrahedral

mesh, which allows for more precise finite-element solution to the field distributions inside the cavity volume. Figure 4.12 shows the meshed geometry of the modular cavity, modeled in Cubit. Note that the mesh density increases near the curved elements to facilitate better precision of RF fields calculation, while still maintaining the reasonable processing time.

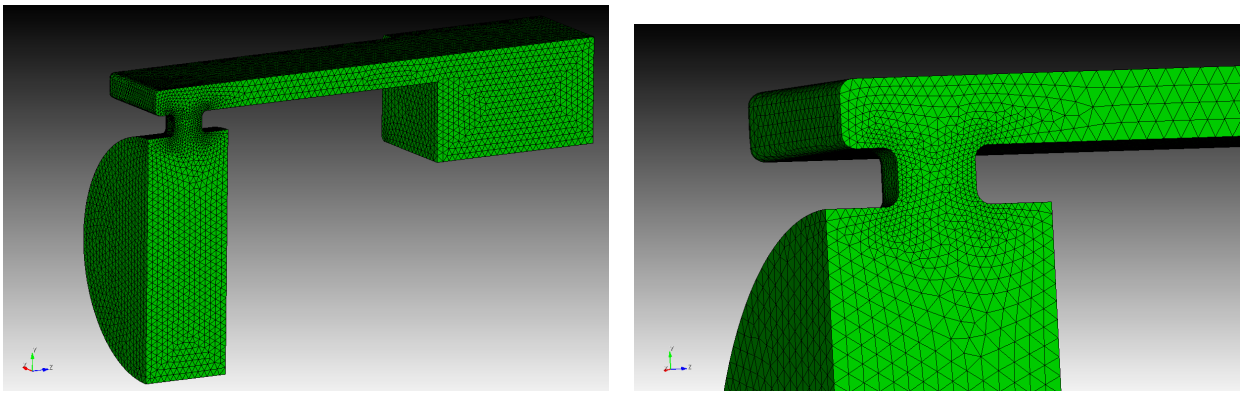

Figure 4.12: Meshed geometry of the Modular Cavity, implemented in Cubit suite. Left - cut in half along the vertical symmetry axis view of the cavity's inner volume. Right - zoom-in on the finite element mesh near the curved coupler input.

After geometry was implemented and meshed in Cubit, ACE3P software was used for calculating the field distribution inside the cavity and the waveguide [78]. ACE3P's sub-package, Omega3P is a parallel finite-element code that numerically solves Maxwell equations with the boundary conditions, defined by the user, to find the electromagnetic field distribution in the cavity, its resonant frequency and other RF parameters [100]. The resulting eigenvector of solutions, together with the cavity geometry can be visualized by the Paraview software [101]. Figure 4.13 shows the color-coded map of the magnitude of electric field inside the cavity volume and the waveguide. As expected, the field is highest in the center of the endplates and drops towards the edges. Corresponding theoretical dependence for the ideal pillbox was described by Equation 1.5.

Figure 4.14 shows the comparison of $E(r)$ between the ideal pillbox solution and the simulated fields in the Modular Cavity. The $E(r)$ dependence for simulated geometry is plotted along the imaginary surface line shown of Figure 4.13. One can see that near the

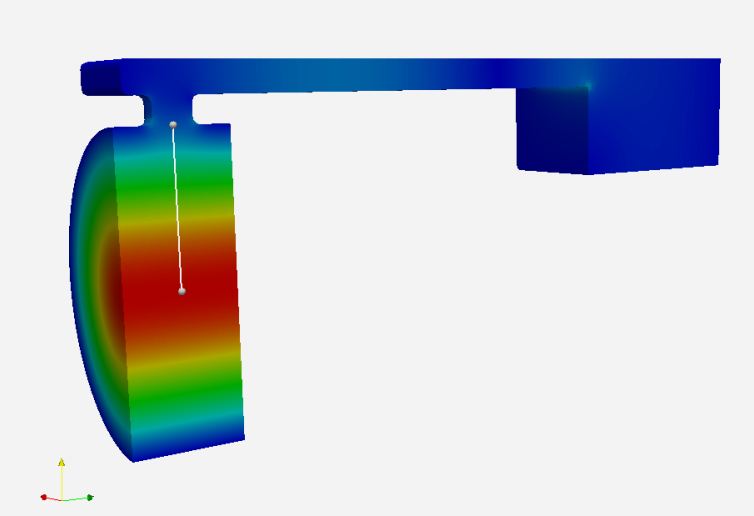

Figure 4.13: Color-coded map of electric field distribution inside the modular cavity.

center of the endplate, the pillbox approximation is very accurate. The coupler geometry introduces additional correction in the $R > 10$ cm region. However, hence the field emission in the center of the endplate is dominant due to stronger electric field, the solution for the perfect pillbox geometry can be used as a substitute for the "real" field distribution in the cavity.

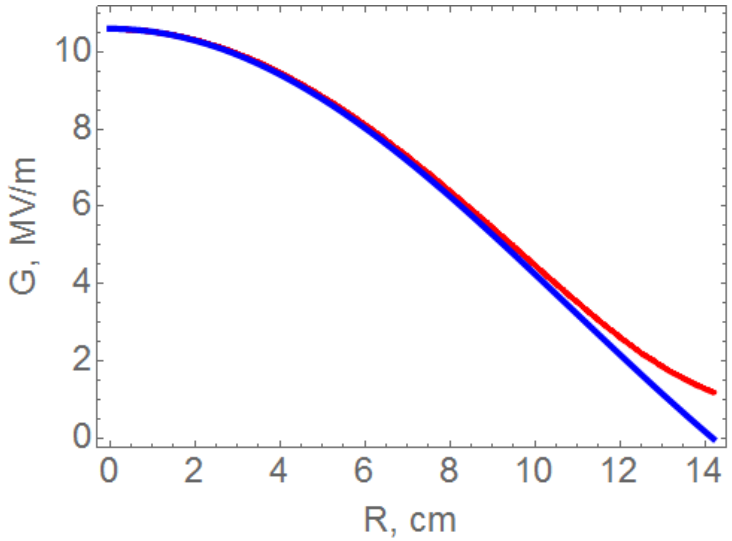

Figure 4.14: $E(r)$ dependence for ideal pillbox with $R_0 = 14.22$ cm (blue) and for simulated modular cavity geometry (red).

To estimate the impact energy of the beam one needs to take into account the su-

perposition of the electric field around asperity and the RF field in the cavity volume: $G_{total} = G_{local} + G_{RF}$. Figure 4.15 shows the behavior of the normal electric field component G_z in the region extending outside the asperity. For distance that is exceeding characteristic radius of the emitter, field enhanced region does not affect the dynamics of the electron. Indeed, compared to the travel distance across the RF gap $L = 10.44$ cm, electron's energy gain in the order of several keV in the $z_o \sim h$ region, has limited effect on the final impact energy. Figure 4.16 demonstrates the effect that the initial energy of emitted electron has on the impact energy at the opposing surface at 30 MV/m gradient. Initial energy of 3 keV was chosen as the universal parameter of the model for all field emission calculations.

The inter-beam interaction of the electrons, namely space-charge effect, plays important part in the focusing of the beam, but does not affect the longitudinal motion of the particle [102]. Consequently, the space charge effect is excluded from the impact energy calculation.

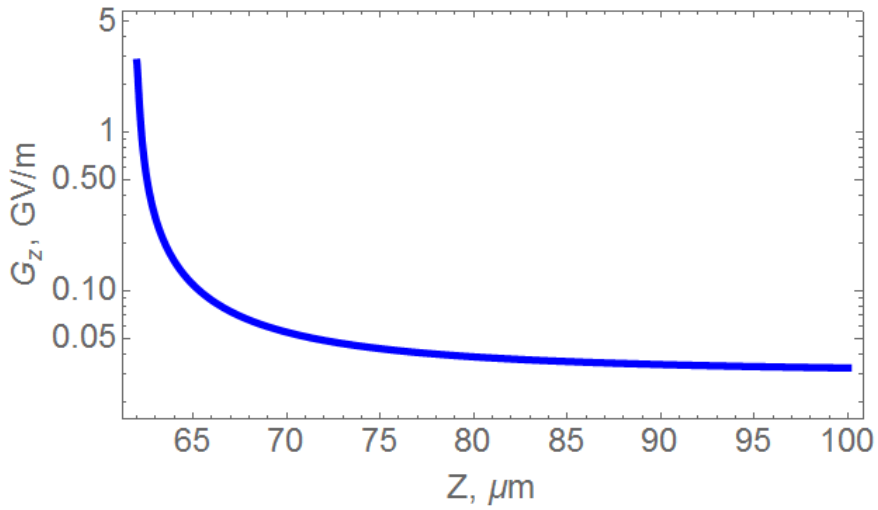

Figure 4.15: Accelerating component of the local field in the region outside asperity. Note that asperity's tip is at z = 62 μm.

Consider an electron moving in the electromagnetic RF field of the cavity. The general equation of motion for the particle in the electromagnetic field can be expressed as:

$$\frac{d\vec{p}}{dt} = q[\vec{E} + \vec{v} \times \vec{B}] \tag{4.13}$$

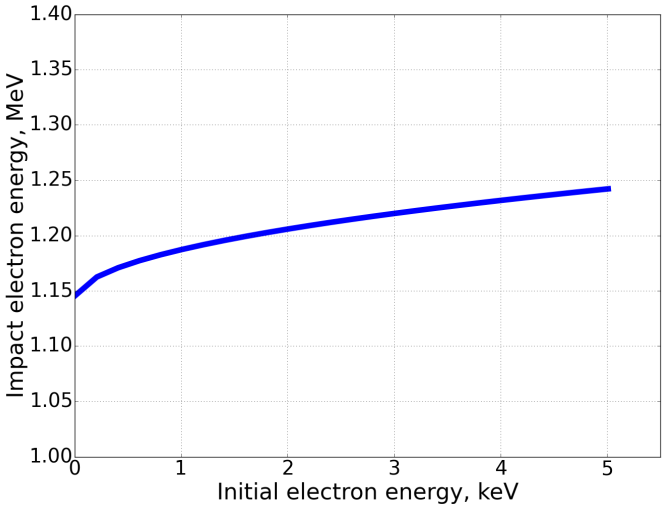

Figure 4.16: Impact energy dependence on the initial electron energy at 30 MV/m gradient.

In the ideal pillbox geometry, electric field has only one non-zero component E_z that oscillates in time: $E_z = E_0 \cos(2\pi f_0\, t + \phi_0)$, where $f_0 = 805$ MHz is the resonant frequency of the cavity and ϕ can be interpreted as the emission phase of the electron, relative to the RF cycle. Magnetic field has all three non-zero components: two radial RF components from pillbox solution Equation 1.5 and the constant solenoidal z component. The system of equations, describing electron motion in the cavity takes the following form:

$$\begin{cases} \dfrac{m_e \ddot{z}}{\left(1-\left(\frac{\dot{z}}{c}\right)^2\right)^{3/2}} = qE_0(z) \cdot \cos(2\pi f_0\, t + \phi_0) + q(\dot{x}B_y - \dot{y}B_x) \\ m_e \ddot{x} = q(\dot{y}B_z - \dot{z}B_y) \\ m_e \ddot{y} = q(\dot{z}B_x - \dot{x}B_z) \end{cases} \tag{4.14}$$

where m_e is the electron mass, c is speed of light in vacuum, q is electron charge and other quantities were defined earlier in this chapter. Note that the first equation governing longitudinal motion of electron is written in the relativistic form, as the electrons are accelerated to the energies comparable and even exceeding the rest energy of electron $m_e = 511$ keV. This system of equations is implemented in Wolfram Mathematica and can be numerically solved for any internally consistent set of input values, namely peak gradient E_0, emission

phase ϕ_0, initial electron energy K_0, momentum $\vec{p}$ and emission coordinate $\vec{r}$.

In this model I will be assuming that electrons are emitted from the sites close to the center of the endplate, where the electric field is strongest. This assumption is based on (a) empirical evidence that breakdown probability is proportional to G_n^5 [31] and (b) Modular Cavity surface inspection findings, that showed the majority of the breakdown damage is localized in the region $R < 3$ cm (see Section 3.2). Figure 4.17 shows the dependence of the impact energy on the surface gradient and emission phase. Note that phase $\phi = 90^o$ corresponds to the positive crest of the surface electric field.

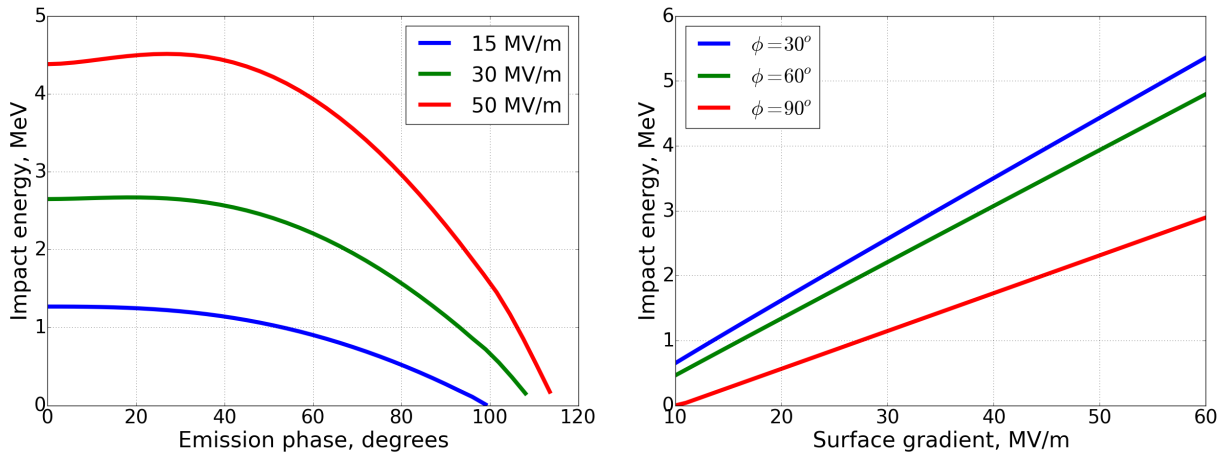

Figure 4.17: Left - impact energy dependence on the phase of the emission for three surface gradient values. Right - impact energy as a function of the surface gradient for different emission phases.

To estimate the transverse size of the dark current beam, result of electron tracking simulations, obtained in [66] will be used. PARMELA simulation was used to find the empirical dependence of beam's RMS radius on the emitted current and on the external magnetic field. Result of the simulations showed the the radius scales as:

$$R_{rms} = 22.6 \, \frac{I^{\,0.33}}{B} \tag{4.15}$$

where R_{rms} is expressed in μm, B in tesla, I in μA. Figure 4.18 shows the impact beamlet radius dependence on the magnetic field for different surface gradients. As the gradient

increases, so does the radius of the beamlet due to the higher current associated with the higher gradient. Authors also emphasize that the result in Equation 4.15 is weakly dependent on the asperity's dimensions, assuming field enhancement factor is held constant [66].

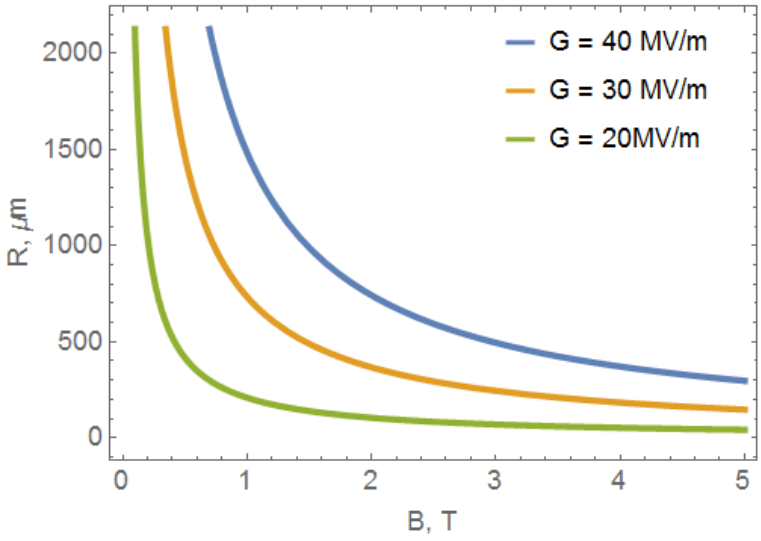

Figure 4.18: Final beamlet radius dependence on magnetic field for different surface gradients.

4.3 Energy deposition by the impacting on the surface dark current beam

Opposing surface of the cavity gets periodically bombarded by the dark current beamlets. Assuming P is the incident power, power density can we expressed as $W = \frac{P}{\pi R_{rms}^2}$. As beam penetrates metal, it loses kinetic energy to the electron-matter interaction. The rate of energy dissipation and penetration depth depend on the properties of the metal, the incident energy of the beam and the total current. Table 4.2 lists the material properties for beryllium, copper and aluminum used in this model.

The stopping power in materials has been theoretically modeled and simulated for the wide range of materials [103]. However, most of the approximations used in modeling energy loss per distance traveled for electrons in matter, are of limited use in the regime when the

Table 4.2: Material properties

Parameter	**Copper**	**Beryllium**	**Aluminum**	**Unit**
Density, ρ	8.90	1.85	2.70	g/cm^3
Work function, ϕ	4.6	5.0	2.7	eV
Specific heat, h	385	1825	900	$J/Kg \cdot K$
Thermal conductivity, λ	401	200	205	$W\ /\ m \cdot K$
Thermal diffusivity, a	1.2×10^{-4}	5.9×10^{-5}	8.4×10^{-5}	m^2/s

scattering angle is not small. In this model I will be using the experimental data on the stopping power of electrons in metals in the 0.3 - 1.0 MeV energy range [104]. Figure 4.19 shows the stopping power in aluminum as a function of the penetration depth for three kinetic energies of electron. Note that higher energy electrons, accelerated by stronger electric field have larger penetration depth. However, deposition rate in the proximity of the surface is higher for less energetic electrons.

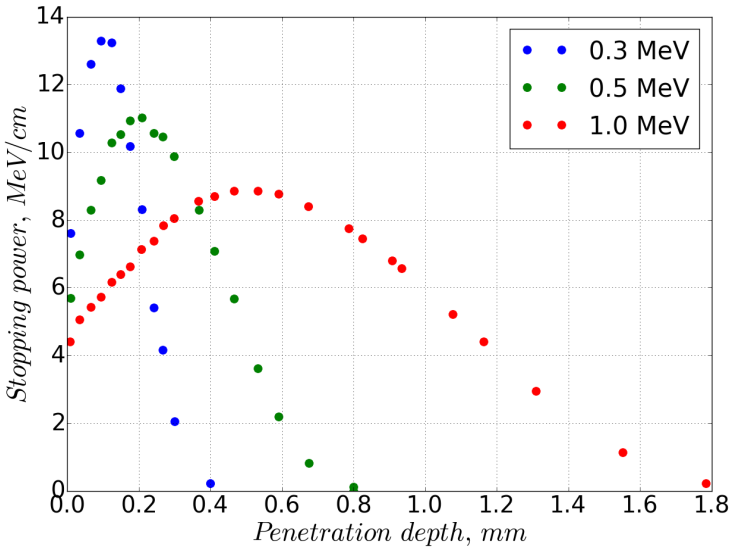

Figure 4.19: Experimental data on electron stopping power $\frac{dE}{dx}$ in aluminum for three energies of impacting particles [104].

Comparison between the stopping power in copper, beryllium and copper is shown in Figure 4.20. Among the three metals, the radiation length of electron in copper is shortest, while beryllium has the longest radiation length for electrons. The energy deposition rate near the surface is also highest for copper and lowest for beryllium.

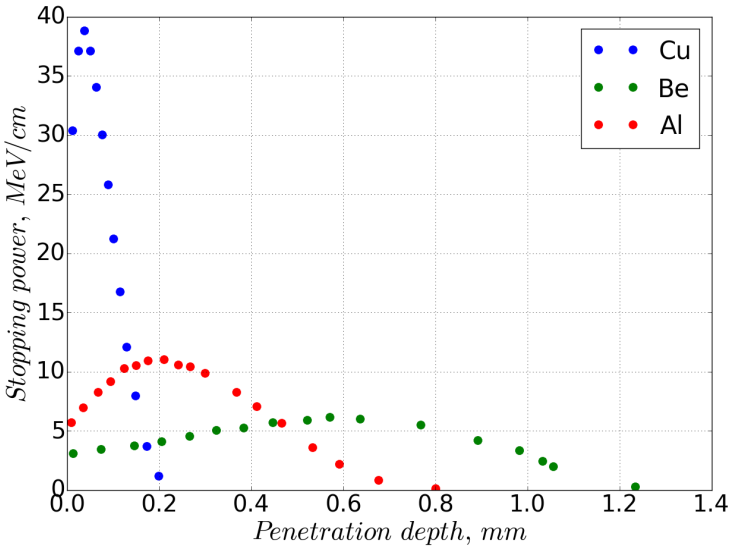

Figure 4.20: Measured stopping power $\frac{dE}{dx}$ for 0.5 MeV electrons in copper, beryllium and aluminum.

Material's stopping power acts as a source term in the heat equation, when calculating the local temperature rise caused by the bombardment of dark current beamlets. As the energy of the impacting electrons depends on the surface gradient and the emission phase, its value might take the continuous range of values. Therefore, the pulsed heating model calls for the explicit functional representation of the stopping power dependence on the impact energy of electrons. To model this dependence, the experimental dE/dx data was fitted with the Gaussian function and that functional form was extrapolated to the continuous spectrum of energies. Figure 4.21 shows the stopping power in aluminum fitted with the Gaussian function of the following form:

$$f(z, A, \mu, \omega) = \frac{A}{\sqrt{\pi/2}\ \omega}\ \exp\Big(-\frac{2(z-\mu)^2}{\omega^2}\Big) \tag{4.16}$$

where A, ω, and μ are the fitting parameters, and z is the penetration depth.

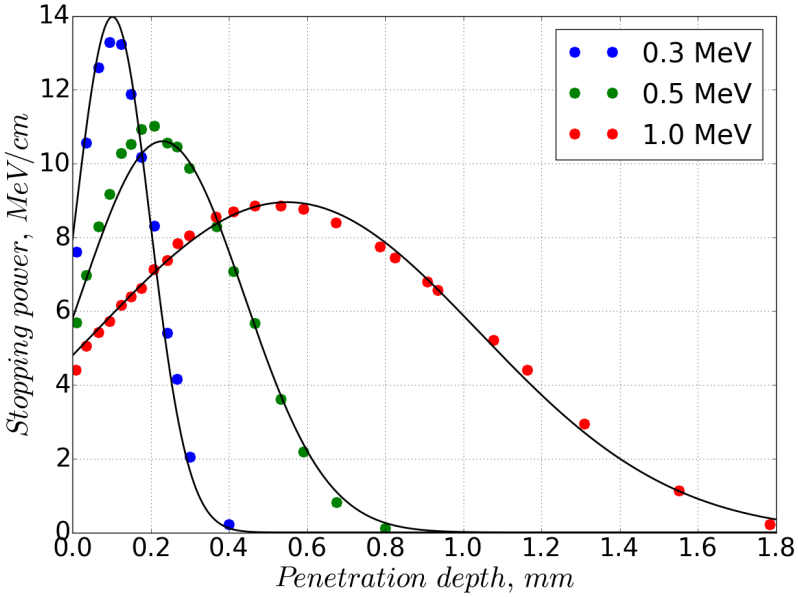

Figure 4.21: Measured electron stopping power in aluminum (colored points), fitted with Gaussian functions (black curves).

4.4 Numerical solution of the heat equation for the local temperature rise

.

As electrons are penetrating in the material they dissipate their kinetic energy in form of heat, which leads to the rise in local temperature at the surface. Following Stratakis's suggestion, this model assumes that most of the beam energy is dissipated into heat within a cylindrical region with radius R_{rms} and length equal to the penetration depth of the electron in metal [105]. Using Equation 4.15, the heat dissipated in the unit volume can then be expressed as:

$$W = N_e \frac{1}{\pi R_{rms}^2} \frac{dE}{dz} = C\ I^{0.33}\ B^2\ \frac{dE}{dz} \tag{4.17}$$

where $N_e = \frac{I}{q}$ is the number of impacting electrons, C is the numerical constant. Several observations can be made from studying Equation 4.17:

- Heating term increases with the beamlet's current. This suggests that higher temperature rise can be expected at higher gradients.
- Delivered power depends on the focusing strength of external magnetic field as B^2. This result is especially important in the context of this dissertation.
- Material with higher $\frac{dE}{dx}$ are more susceptible to the local heating by dark current. This hints towards higher expected gradient performance of beryllium, the material with longer radiation length compared to copper.

For calculating the local temperature rise under the heat generated by the incoming electron beam, I will be solving the heat equation in cylindrical coordinates:

$$\frac{1}{r}\frac{\partial}{\partial r}\Big(r\frac{\partial T}{\partial r}\Big) + \frac{\partial^2 T}{\partial z^2} + \frac{1}{\lambda}W(r,z,t) = \frac{1}{a}\frac{\partial T}{\partial t} \tag{4.18}$$

The typical radiation length for MeV- energy range electrons is several millimeters, which is smaller than the thickness of the Modular Cavity endplates (d = 14.2 mm). The radius of the beamlet in simulations does not exceed several millimeters. For the semi-infinite disk heated at the surface by a disk heat source, cylindrical Green Functions can be applied to yield the exact solution in the form of an integral [106]. The surface of the semi-infinite disk is considered to be insulated everywhere except for $0 < r < R_{rms}$. Initial temperature is taken to be zero for convenience. A mathematical representation of the boundary conditions for equation 4.18 is the following:

$$\begin{gathered} -\lambda\frac{dT(r,0,t)}{dz} = \begin{cases} q_o & for\ 0 < r < R_{rms} \\ 0 & for\ r > a, \end{cases} \\ T(r,z,t) \to 0 \quad for\ r \to \infty \quad and \quad z \to \infty, \\ T(r,z,0) = 0, \end{gathered} \tag{4.19}$$

It is important to discuss the validity of the approximations in the context of time-scale

of the physical processes involved. The length of the RF pulse in Modular Cavity tests is 30 μs, the maximum repetition rate is 10 Hz. This means that each RF is separated by 0.1 s gap. During the RF pulse metal surface is bombarded with the dark current electrons periodically with frequency $f_0 = 805$ MHz, which means that the characteristic time between the intensity peaks is 1.2 ns. The general properties of the heat propagation tell us that the characteristic distance of heat transfer in the material is $D \sim \sqrt{a\,t}$, where a is the thermal diffusivity and t is time. Figure 4.22 puts this dependence for copper in perspective of timescales outlined above.

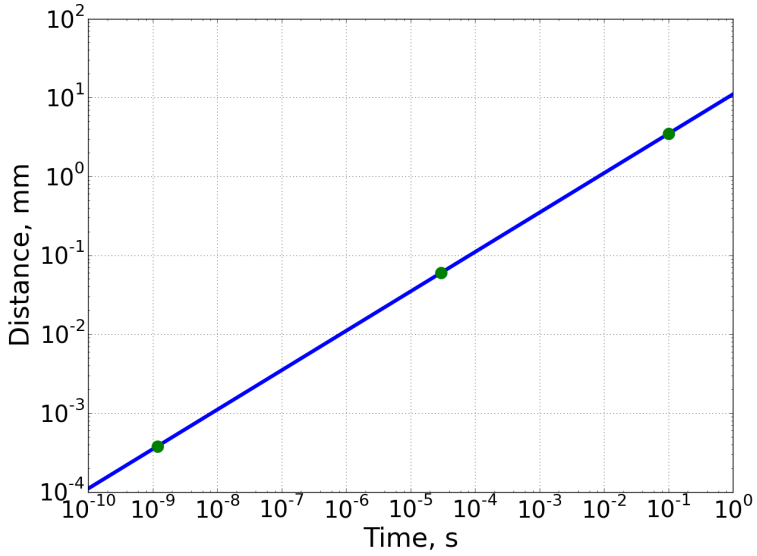

Figure 4.22: Characteristic time sclale vs heat propagation distance for copper (blue line). Relevant points for pulsed heating effect are marked with green dots.

On the 805 MHz timescale (t $\sim$ 1.2 ns) the heat propagation length does not exceed 1 μm, which is orders of magnitude less than the characteristic radius of the beamlet R_{rms}. This means that one can exclude RF time dependence from the calculations and substitute it with the steady-state heating term. During the 0.1 s between the pulses heat dissipates over the distance of $d \sim 5$ mm, which significantly larger than R_{rms}. Thus, we can limit the calculation of local temperature rise to just one RF pulse and assume that the local temperature returns to the average endplate temperature by the start time of the next RF

pulse. Note that these estimates are also valid for beryllium and aluminum, as their thermal diffusivity is comparable to copper (see Table 4.2).

The temperature rise at the surface of the cylinder could be expressed as an integral using Green's functions [106]:

$$\Delta T = \frac{a}{\lambda}\int_0^{R_{rms}}\int_0^{d}\int_0^{\tau_p} G_R \cdot G_z \cdot W(r,' z', t)\; 2\pi r\; dr'\; dz'\; dt \tag{4.20}$$

where d is the cylinder's length, G_R and G_z are the one dimensional Green functions that take the following form:

$$\begin{aligned} G_z(z,z') &= \frac{1}{\sqrt{4a\pi t}}\Big[\exp\Big(-\frac{(z-z')^2}{4at}\Big) + \exp\Big(-\frac{(z+z')^2}{4at}\Big)\Big] \\ G_r(r,r') &= \frac{1}{4a\pi t}\cdot\exp\Big(-\frac{r^2+r'^2}{4at}\Big)\cdot I_0\Big(\frac{r\;r'}{2at}\Big) \end{aligned} \tag{4.21}$$

where a is metal thermal diffusivity and I_0 is the modified Bessel function of the first kind. Now, combining Equations 4.20, 4.21 4.17, 4.16, the final integral for the temperature rise calculation becomes:

$$\begin{aligned} \Delta T(t,r,z) = \frac{2a}{q\lambda R^2}\int_0^{\tau_p} I dt' \int_0^{R}\left(\frac{r\;dr'}{4a\pi t}\exp\Big(-\frac{r^2+r'^2}{4at}\Big) I_0\Big(\frac{r\;r'}{2at}\Big)\right)\times \\ \int_0^{d}\left(\frac{dz'}{\sqrt{4a\pi t}}\Big[\exp\Big(\frac{-(z-z')^2}{4at}\Big) + \exp\Big(\frac{-(z+z')^2}{4at}\Big)\Big]\right)\times\frac{A}{\sqrt{\pi/2}\;\omega}\;\exp\Big(\frac{-2(z-\mu)^2}{\omega^2}\Big) \end{aligned} \tag{4.22}$$

where A, ω, μ are the gaussian fit parameters for $\frac{dE}{dz}$, $R \equiv R_{rms}$, τ_p is the RF pulse length, a and λ are the material properties, defined in Table 4.2. The first integral in 4.22 corresponds to the integrated current over the pulse length τ_p. As discussed earlier, current fluctuations within RF period do not affect the temperature calculation. This means one can rewrite $\int_0^{\tau_p} I dt = N\int_0^{\tau_{rf}} I dt$, where τ_{rf} is the period of one RF cycle and N is the number of RF cycles in one RF pulse, so that $\tau_p = N \times \tau_{rf}$.

To calculate $\int_0^{\tau_{rf}} I dt$ numerically, positive half-period of the electric field's RF sine wave

is divided into 16 points for phases $\phi_n = 35^o,\ 40^o ... 110^o$. The total current at each point is calculated according to 4.12 and the integral is approximated by the Riemann sum $\int_0^{\tau_{rf}} Idt = \sum_{n=1}^{16} I(\phi_n)\Delta t_n$. Figure 4.23 demonstrates the procedure of current integral approximation for surface gradient 30 MV/m. Note that the calculated current for $\phi_n < 35^o$ is negligible compared to the current near the crest of the waveform. Electrons emitted at $\phi_n > 110^o$ phase typically do not reach the opposite wall of the cavity or have very low impact energy (see Figure 4.17).

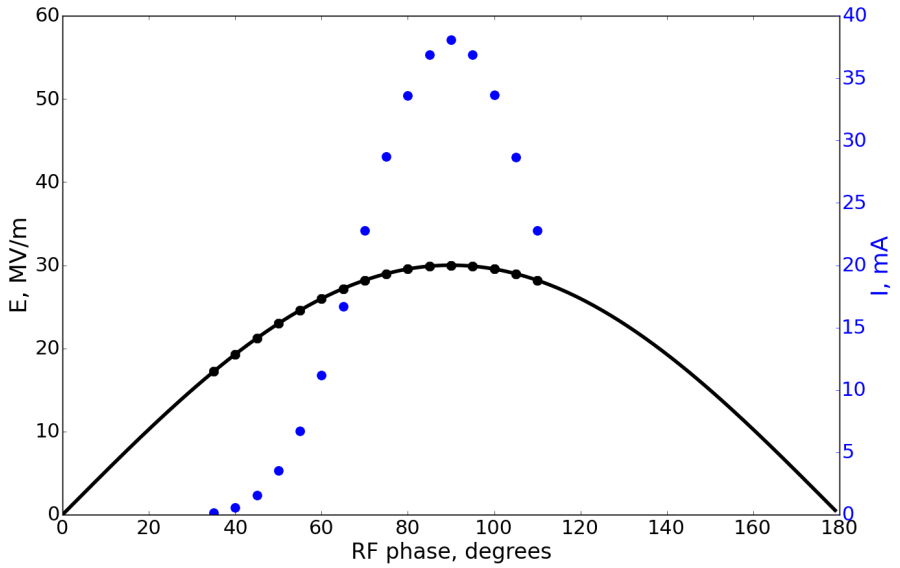

Figure 4.23: Dark current integration procedure over one RF period. Black line demonstrates the positive half RF period of surface gradient with black dots marking the time points at which current values are calculated. Current values for each phase are shown as blue dots).

Integral representation of the temperature rise 4.22 can be solved numerically for any point t_0, r_0, z_0. According to the pulsed heating model, the surface temperature rise is the critical therefore z_0 is set to zero. The choice of t_0 is dictated by the duration and shape of the RF pulse during the Modular Cavity's high power runs. Figure 4.24 shows the typical envelope of the pickup signal. The duration of the RF pulse length delivered to Modular cavity by the power source is 32 μs, followed by the exponential decay in the stored energy. $\tau_p = 20$ μs shown with dashed lines, during which the gradient deviation from the maximum does not exceed 5%, was chosen for the pulsed heating model input. Sensitivity of the model

predictions to pulse length will be discussed in Chapter 5.

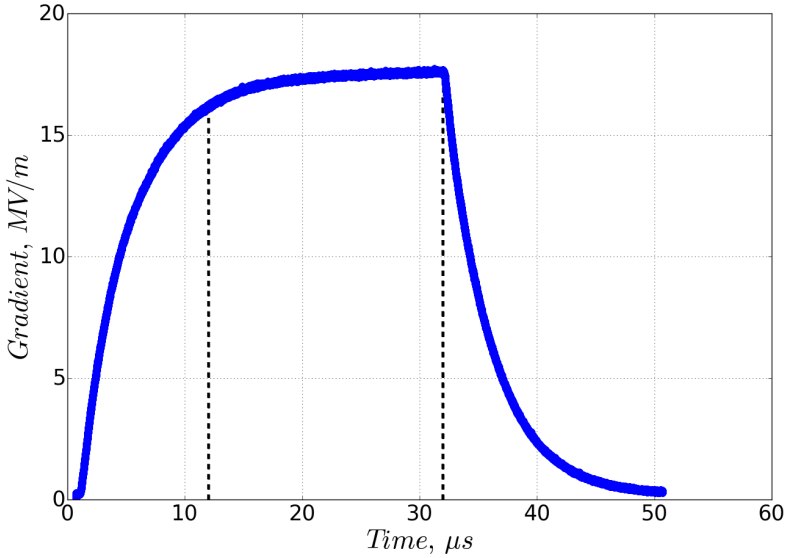

Figure 4.24: Example of the pickup signal envelope during the Modular Cavity run. 20 μs flat top is marked with vertical dashed lines.

Figure 4.25 shows the temperature profile solution on the surface, calculated for copper endplate operating at 20 MV/m in three tesla field. The maximum temperature of $T = 44$ K is reached at the center of the impacting beam profile.

4.4.1 Translating local temperature rise to the threshold gradient

When the thermal stress, imposed by the bombarding electrons exceeds the elastic limit of material, surface defects, such as cracks, can develop due to cyclic fatigue [107]. Cyclic fatigue is the metal fatigue caused by the cyclic heating and cooling. If the heating happens quick enough, the fast heating of skin layer by dark current leads to the thermal expansion in the surface of material, while inner colder layers are confined and are limited in the ability to expand transversely. H.M. Musal demonstrated that during the initial part of the temperature increase the metal surface is subject to compression within its elastic range [108]. However, after the yield stress is reached, surface undergoes the plastic compression. The threshold temperature rise for the plastic deformation can be expressed as:

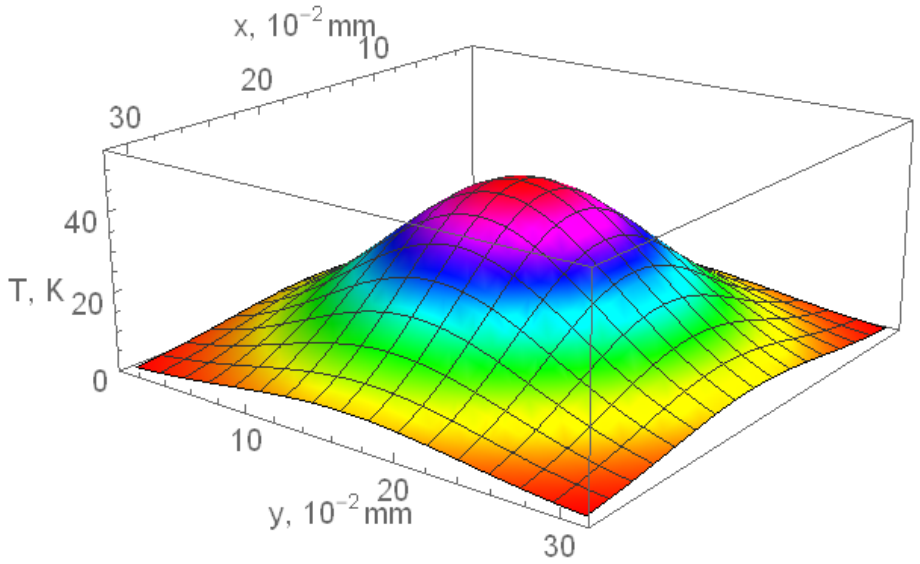

Figure 4.25: Surface temperature profile solution for the copper endplate in three tesla magnetic field, operated at 20 MV/m surface gradient.

$$\Delta T_s = \frac{(1-v)\sigma}{\alpha\epsilon} \tag{4.23}$$

where v, σ, α are mechanical properties of the material defined in Table 4.3. Previous experiments showed the visible surface damage when operating cavities at conditions exceeding ΔT_s [109]. Table 4.3 also includes the calculated values for the threshold temperatures for plastic deformation in copper, beryllium and aluminum. The lowest of three threshold temperature for copper is the consequence of the relatively low yield stress compared to other materials. Largest of three, the critical temperature for beryllium indicates that beryllium might be less susceptible to the pulsed heating induced stress. Figure 4.26 demonstrates the calculated surface temperature rise dependence on the external magnetic field for copper. Naturally, the higher accelerating gradient leads to the larger increase in surface temperature. More importantly, strong dependence of the temperature rise on the external magnetic field is evident - the heating source term in Equation 4.20 becomes large at strong magnetic fields

Table 4.3: Mechanical properties of materials

Parameter	**Copper**	**Beryllium**	**Aluminum**	**Unit**
Poisson ratio, v	0.330	0.330	0.032	-
Elastic modulus, ϵ	1.3×10^{11}	6.9×10^{10}	3.0×10^{11}	N/m^2
Yield stress, σ	6.2×10^{7}	2.8×10^{8}	2.4×10^{8}	N/m^2
Linear expansion, α	1.7×10^{-5}	2.4×10^{-5}	1.2×10^{-5}	1/K
Threshold temperature, ΔT_s	38	128	224	K

due to the focusing effect. The dashed line in Figure 4.26 relates to the threshold temperature for copper, $T_s = 38$ K. Figure 4.26 also suggests that for each gradient $G_s \geq 20$ MV/m there is a threshold magnetic field for which the temperature rise exceeds the elastic limit of copper, making it susceptible to the cyclic fatigue.

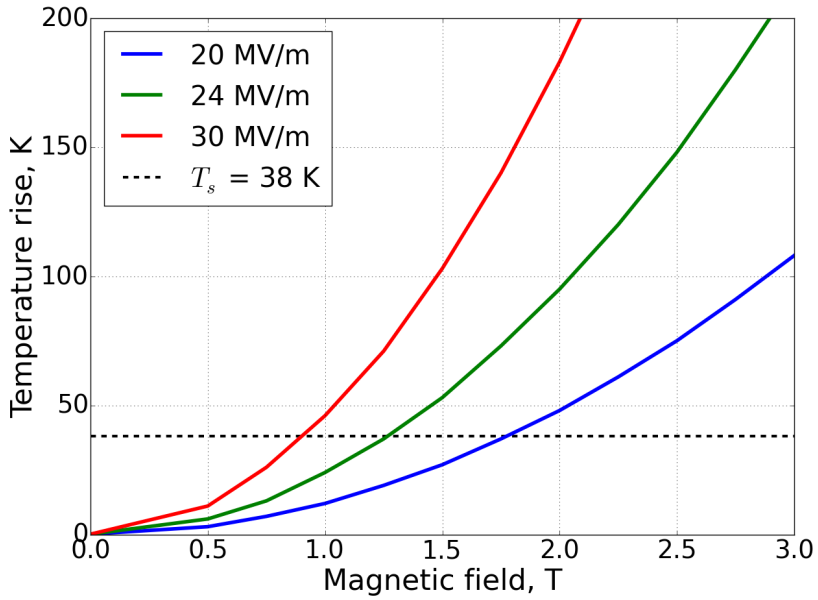

Figure 4.26: Surface temperature rise dependence on the external magnetic field. Dashed line corresponds to the threshold plastic deformation temperature for copper.

Comparison of the temperature profiles between copper, aluminum and beryllium are summarized in Figure 4.27. The trend of the dependence is the same for all three materials, however, longer radiation length of beryllium makes beryllium less prone to the cyclic temperature rise. Together with the higher threshold temperature $T_s(Be) = 224$ K this might explain the higher gradient performance of beryllium during the Modular Cavity tests.

Figure 4.27 also predicts better performance of aluminum compared to copper in external magnetic field.

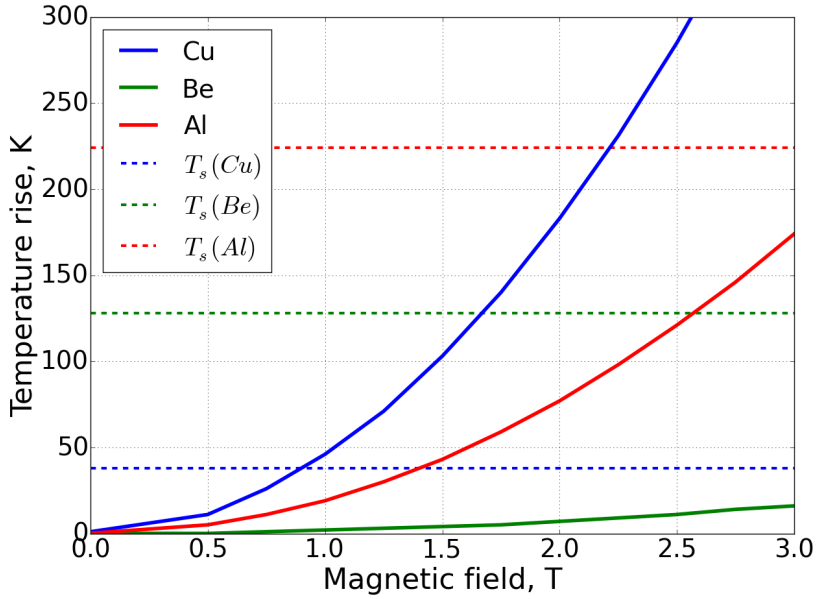

Figure 4.27: Surface temperature rise dependence on the external magnetic field for copper, beryllium and aluminum at 30 MV/m gradient. Dashed lines correspond to the threshold plastic deformation temperatures for three materials.

When radius of the impacting beam goes to zero, the temperature rise should approach the solution of the heat equation with delta function source term. This can be illustrated by imposing $B \longrightarrow \infty$, which corresponds to $R_{rms} \longrightarrow 0$, according to Equation 4.15. Figure 4.28 shows the asymptotic of the temperature rise behavior. As expected, the temperature rise plateaus when $B \longrightarrow \infty$. One can see that for 26 MV/m the temperature rise plateaus at around B = 10 tesla, and at around B = 5 tesla for 20 MV/m. Figure 4.28 suggests that magnetic fields above some threshold value does not lead to deterioration in the gradient performance of the material.

It is now possible to obtain the predictions for the threshold gradient in the external magnetic field for all three materials. The threshold gradient G_t is defined by the condition of the calculated local temperature rise ΔT not to exceed safe temperature T_s. Results for copper, beryllium and aluminum are shown in Figure 4.29. One can see that the predicted

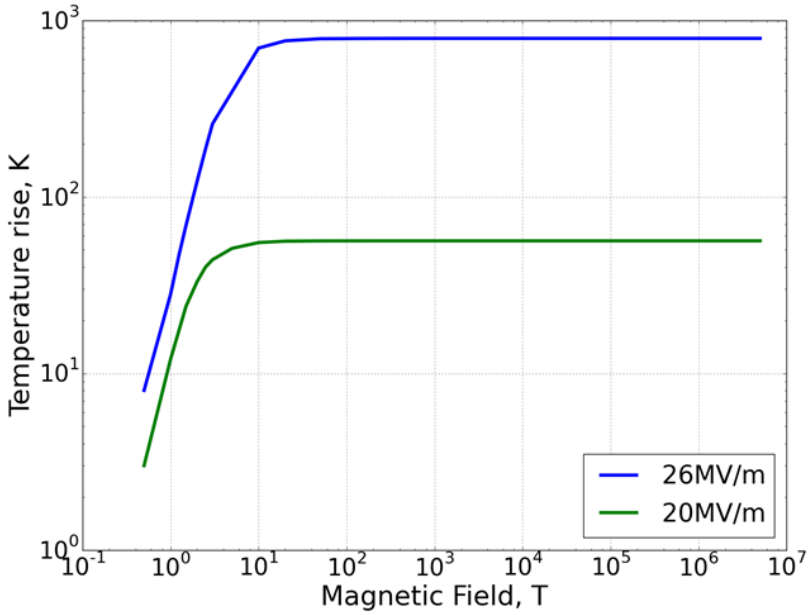

Figure 4.28: Asymptotic behavior for the temperature rise in copper with $B \longrightarrow \infty$ for two gradient values.

gradients for beryllium are significantly higher than for copper. It is important to compare the measured safe operating gradients during Modular Cavity's high power tests with the predictions of the pulsed heating model. However, the limited number of data points in Figure 4.29 does not allow for the comprehensive statistical analysis. The pulsed heating models assumes that dark current electrons, focused by magnetic field, play a significant part in the initiation stage of RF breakdown. However, when magnetic field is absent, corresponding temperature rise due to electron bombardment approaches zero (as can be seen in Figure 4.27). This implies that pulsed heating paradigm is relevant only for the conditions involving strong magnetic field. When B-field is zero, other breakdown mechanisms come into play; detailed study of these mechanisms is beyond the scope of this dissertation.

Measured safe operating gradient in 3 tesla for copper $G = 12.2$ MV/m is 37% lower than the predicted value $G_s = 19.5$ MV/m. This discrepancy can be explained by the severity of surface damage inflicted during three tesla operation. Observed melted pits with rough crater edges, small copper droplets and cracks in solidifying material indicate that

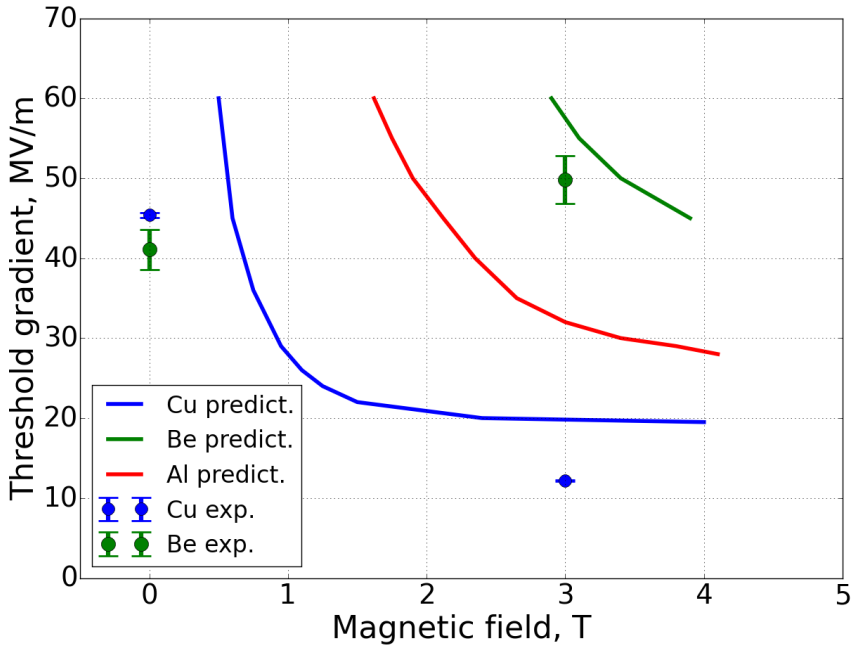

Figure 4.29: Threshold gradient predictions for copper, beryllium and aluminum by the pulsed heating model (colored lines). Points on the graph correspond to the measured gradients of copper and beryllium in Modular Cavity runs.

the field enhancement factor β might increase with more damage accumulating. Indeed, the deterioration of the operating gradient was observed during the high power test in three tesla (see Section 3.1).

Prediction for the three tesla gradient performance of beryllium $G_s = 56.5$ MV/m is 10% higher than the measured safe operation gradient of $G = 49.8$ MV/m. Importantly, the gradient predictions for beryllium are more than $> 100\%$ higher compared to copper at a given magnetic field value, the trend that is reflected in the experiment. Note that during the last high power test with beryllium, stable performance with limited breakdown rate was observed when operating at gradients up to 60 MV/m in external magnetic fields up to 3.5 tesla (see Section 3.1).

4.4.2 Pulsed heating model sensitivity to emitter's dimensions

Following formalism in [66], the model considers the prolate spheroidal emitter with the following dimensions: a = 1.77 μm, h = 62 μm. Corresponding field enhancement factor for this emitter is $\beta = 385$, which agrees with the dark current measurements in the 805 MHz multicell cavity experiment [49]. However, the same field enhancement factor can be achieved in the emitter of the same shape but different dimensions, with the constraint of keeping the $\frac{h}{a}$ constant. Figure 4.30 shows the comparison of the surface temperature rise predictions for the "full size" emitter and the "half size" emitter, for which a = 0.88 μm and h = 31 μm. Note that the factor of ~ 2 difference in the calculated temperature rise predictions between the two emitters translates to only $\sim 10\%$ difference in the threshold gradients.

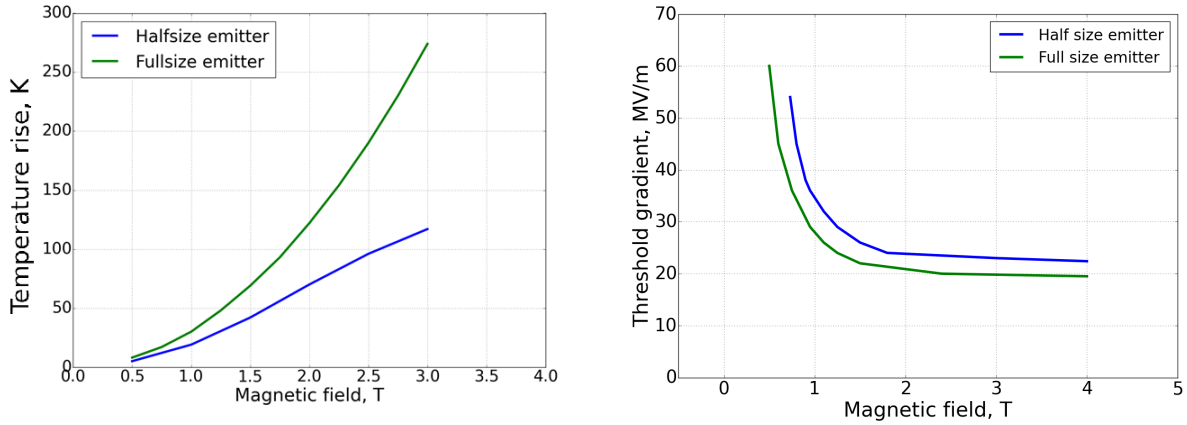

Figure 4.30: Left - surface temperature rise dependence on magnetic field for the "half size" emitter and "full size" emitter. Right - threshold gradient predictions for both emitters by the pulsed heating model.

CHAPTER 5

CONCLUSION

The experimental program of the Modular Cavity allowed for the detailed study of RF breakdown in external magnetic field. The modular design of the cavity enabled frequent inner surface inspections after the high power runs with fixed external magnetic field values. Addressing the goals outlined in Section 2.8.3, the following can be noted:

- Breakdown damage induced in high-power operation was observed only on the flat endwalls of the Modular Cavity, where electric fields are the highest by design. This allows to discuss the RF breakdown in the context of the defined surface gradients and trajectories of dark current electrons.

- Measurements of the safe operating gradient of the Modular Cavity's configurations with beryllium and copper endplates in zero and three tesla magnetic fields were performed. As copper and beryllium were tested in similar operating conditions, direct comparison of the materials' gradient performance is possible.

- Surface inspections after each high power test allowed for the characterization of the breakdown damage, observed on the beryllium and copper endplates at different values of the external magnetic field.

Muon ionization cooling channel designs require operating normal conducting RF cavities in multi-tesla external magnetic fields. The most recent designs require 22 MV/m operation of 805 MHz cavities in 3.5 tesla field [18]. The measured safe operating gradient of the Modular avity in 3 tesla magnetic field is 49.8 ± 3.0 MV/m. The cavity was also operated in 3.5 tesla and showed stable performance at the gradients exceeding 50 MV/m during 350k RF pulses of operation. Thereby, Modular Cavity demonstrated the feasibility of achieving the designed gradients in vacuum RF cavities for the muon ionization cooling channels.

The pulsed heating model of RF breakdown aims to quantify the gradient limitations on operating RF cavities in the strong focusing magnetic field. In this work, the model was developed to generate predictions for the Modular Cavity, tested in copper and beryllium configurations. Measured Safe Operating Gradient for copper in three tesla field is 12.2 MV/m, 37% lower than the predicted by the pulsed heating model 19.5 MV/m. Measured SOG for beryllium in three tesla field is 49.8 MV/m, 10% lower than predicted by the model 55 MV/m. Several factors might account for these discrepancies.

First, the notion of the safe operating gradient is an artificial construct. Threshold breakdown rate of 10^{-5} is dictated by the specific requirements of the muon ionization cooling channel. The pulsed heating model equates the safe operating gradient and the threshold gradient for plastic deformation, so it is implicitly dependent on the breakdown rate assumptions.

Second, the pulsed heating model assumes the prolate spheroidal shape of the asperity with the field enhancement factor of $\beta_e = 385$. Locations of the breakdown damage, induced in three tesla field on copper were observed to cover large surface area on the endplates. This suggests that RF breakdowns might be triggered by multiple surface defects, randomly activated at different times. It is reasonable to assume the variation within the shape of these defects. Moreover, damage induced in three tesla field in copper changes the morphological properties of the surface. In particular, the observed splashes of melted copper can contribute to the additional increase in the field enhancement factor by 2 - 5 times (see Section 3.2).

Third, the gradient predictions of the pulsed heating model are calculated through the estimation of the safe temperature for the metal's elastic limit ΔT_s, where the safe temperature is calculated using the mechanical properties of the material (see Equation 4.23). However, Kuzikov *et al.*, demonstrated that required temperature for surface fracture also depends on the operating conditions [111]. Equation 5.1 shows the expression of required temperature for copper surface fracture:

$$\Delta T_f = \left(\frac{1}{A\sqrt{\tau}}\right)^{1/2} \sqrt{\ln\left(\frac{1}{n}+1\right)} \tag{5.1}$$

where n is the number of accumulated RF pulses, τ is the pulse length, and A is constant. For the Modular Cavity's copper high power tests, $\tau = 30\ \mu s$, $n \approx 2\times10^7$, and Equation 5.1 gives $\Delta T_f \approx 76\ ^{o}$C. Similar analysis for the required temperature rise for the surface fracture in beryllium will be an interesting study in the future. Limited operation time allocated for the Modular Cavity program did not allow for studying the safe operating gradient dependence on the number of accumulated RF pulses. More breakdown statistics would enable separating the effects of surface conditioning and surface degradation, as well as improve the accuracy in the safe operating gradient measurements.

Resources of the Modular Cavity program did not allow for the detailed dark current studies. Thick 1.3 cm copper endplates absorb the impacting electrons, preventing them from passing through to the detectors. Operational time constraints did not allow for the imaging study of the dark current, passing through the thin 2 mm window in the beryllium endplates. Measurements of the electron current and the transverse size of the dark current beamlets would enable to estimate the surface emitters' dimensions and shape (see Section 4.1). Therefore, detailed dark current study would allow to improve the precision of the pulsed heating model.

Another possible test of the pulsed heating model is studying the effect of RF pulse length on the safe operating gradient. Figure 5.1 shows the simulated dependence of the local surface temperature rise on the length of RF pulse. Large values of the pulse length correspond to the steady state solution of the heat equation 4.17. That regime corresponds to the plateauing region in Figure 5.1. According to the model, decreasing the pulse length can mitigate the deteriorating effect of the pulsed heating.

Observed perfect one-to-one correspondence between the damage on the opposing plates suggests the connection between the opposing surfaces through the charged particles' trajectories. This provides an indirect evidence that the dark current beamlets, confined to

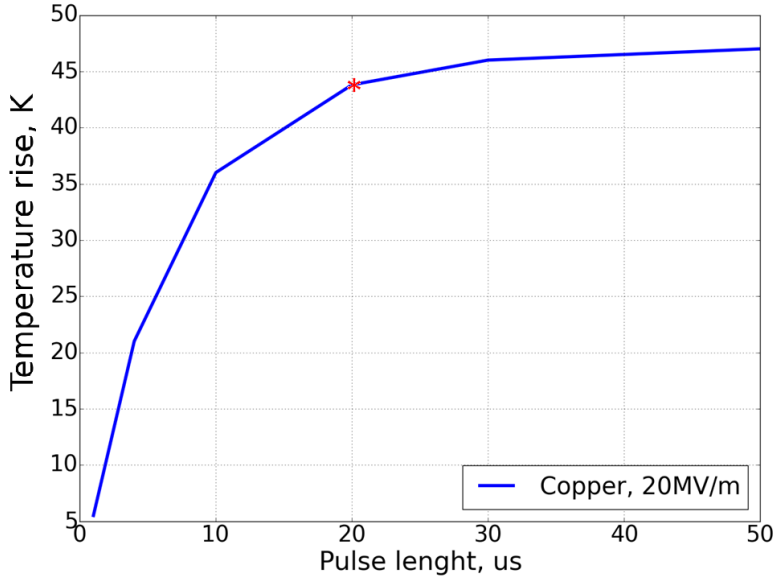

Figure 5.1: Simulated local temperature rise dependence on the RF pulse length for copper at operated 20 MV/m. Red asterisk marks the pulse length $\tau = 20\ \mu s$, used in the pulsed heating model calculations.

move along the straight-line trajectories in the focusing magnetic field, are influencing the RF breakdown mechanism. The disruptive nature of the damage incurred during three tesla copper operation indicates that the focusing effect of the magnetic field leads to higher energy density deposited near the metal surface.

Table 5.1: Radiation length for 1 MeV charged particles in copper and beryllium [112].

Particle	**Be radiation length, mm**	**Cu radiation length, mm**
Proton	0.016	0.007
Electron	2.95	0.71

Longer radiation length of protons and electrons in beryllium suggests that the kinetic energy of the impacting charged particles gets deposited deeper into material relative to copper. Table 5.1 shows the radiation length of 1 MeV electron and 1 MeV proton in copper and beryllium. 1 MeV is the typical impact energy of charged particle accelerated by the RF field in the Modular Cavity. One can see that the radiation length for both particles is shorter in copper. This might explain no observed microscopic damage on beryllium in three

tesla operation: charged particles penetrate deep into material and dissipate the energy in the form of heat further away from the surface.

Modular Cavity's experimental program shed light on the previously unknown aspects of RF breakdown in strong magnetic field. New revealed phenomena of breakdown damage matching and splashing of melted material in multi-tesla fields will benefit of more detailed study in the future. Gradient results and surface inspection findings provide the additional evidence in favor of the pulsed heating model. This work provides the motivation for the next steps in studying the phenomenon of RF breakdown in strong magnetic fields.

REFERENCES

REFERENCES

[1] V. Barger et al., "S-Channel Higgs boson production at a muon-muon collider", Phys. Rev. Lett. 75, 1462.

[2] D. Neuffer et al.,"A muon collider as a higgs factory", arXiv:1502.02042 .

[3] P. McIntyre et al., "Dynamics of decay electrons and synchrotron radiation in a TeV muon collider", proceedings of PAC 2001, Chicago, USA, RPPH314.

[4] J-P. Delahay et al., "Enabling intensity and energy frontier science with a muon accelerator facility in the U.S.: white paper", Fermilab-conf-13-307-APC.

[5] "A multi-TeV linear collider based on CLIC technology", CLIC Conceptual Design Report, Geneva 2012

[6] https://fcc.web.cern.ch/Pages/About.aspx

[7] "The International Linear Collider technical design report. Volume 1: Executive Summary", 2013.

[8] M.S. Zisman, "Neutrino factory downstream systems", Workshop on European Strategy for Future Neutrino Physics, CERN, Geneva, Switzerland, October 1-3, 2009.

[9] S. Goswami et al., "Testing non-unitarity of neutrino mixing matrices at neutrino factories", arXiv:0802.1434 [hep-ph].

[10] J. Marriner, "Stochastic cooling overview", arXiv:physics/0308044 [physics.acc-ph].

[11] A. Ruggiero, "A muon collider scenario based on stochastic cooling", Nuclear Instruments and Methods in Physics Research A 350 (1994) 45-52.

[12] R.V. Tumanian, "Resonant laser cooling of circular accelerator beams", arXiv:physics/0410009 [physics.acc-ph].

[13] G.I. Budker and A.N. Skrinski., "Electron cooling and new possibilities in elementary particle physics", 1978 Sov. Phys. Usp. 21 277.

[14] https://map.fnal.gov/muon-collider/graphics.shtml.

[15] A.N. Skrinsky and V.V. Parkhomchuk, Sov.J.Part.Nucl. 12, 1981.

[16] D. Neuffer, Introduction to Muon Cooling, Proc. ECOOL03, Nucl. Inst. and Meth. A 532, 26 (2004).

[17] S.Geer, "Muon Colliders and Neutrino Factories", Annu. Rev. Nucl. Part. Sci. 2009.59:347-365.

[18] D. Neuffer, "Comments on ionization cooling channels" 2017 JINST 12 T09004.

[19] D. Kaplan., "Muon cooling, muon colliders, and the mice experiment", arXiv: 1307.3891v1.

[20] M. Bogomilov, "Design and expected performance of the MICE demonstration of ionization cooling", arXiv:1701.06403v2.

[21] https://map.fnal.gov/.

[22] "Muon Accelerator R&D Issues, White paper", October 2014.

[23] J-P. Delahaye et al., "Enabling Intensity and Energy Frontier Science with a Muon Accelerator Facility in the U.S", MAP White paper, Fermilab-conf-13-307-APC.

[24] R.D. Ryne et al., "Design Concepts for muon-based accelerators", Proceedings of IPAC2015, Richmond, VA, USA, WEPWA057.

[25] J. D. Cockcroft and E. T. S. Walton, Experiments with High Velocity Positive Ions.(I) Further Developments in the Method of Obtaining High Velocity Positive Ions, Proceedings of the Royal Society A, vol. 136, pp. 619630, 1932.

[26] R. Widere "ber Ein Neues Prinzip Zur Herstellung Hoher Spannungen". Archiv fr Elektronik und bertragungstechnik. 21 (4): 387. doi:10.1007/BF01656341.

[27] H. Padamse, J. Knoblochm and T. Hays, "RF superconductivity for accelerators", Cornell University, Ithaca, New York.

[28] Y. Takahashi, "Two Hundred Years of Lichtenberg Figures", Journal of Electrostatics, Volume 6, Issue 1, 1979.

[29] D. Alpert et al., "Initiation of electrical breakdown in ultrahigh vacuum", J. Vac. Sci. Technol. 1, 35 (1964); doi: 10.1116/1.1491722.

[30] A. Degiovanni and W. Wuensch, "Comparison of the conditioning of high gradient accelerating structures", Phys. Rev. Accel. and Beam 19, 032001 (2016).

[31] V.A. Dolgashev et. al., "RF breakdown in normal conducting single-cell structures", proceedings of PAC2005, Knoxville, Tennessee.

[32] M.D. Karetnikov, "An origin of RF breakdown in vacuum", Particle Accelerators 1997, Vol 57, pp. 189-214.

[33] F. Schwirzke, "Unipolar arc model", Journal of Nuclear Materials 128/129 (1984) 609-612.

[34] P.B. Wilson, "A plasma model for RF breakdown in accelerator structures", eConf C00082 (2000) TUE05.

[35] Z. Insepov and J. Norem, "Can surface cracks and unipolar arcs explain breakdown and gradient limits?", J. Vac. Sci. Technol. A, Vol. 31, No. 1, 2013.

[36] M.J. Mulcahy and P.C. Bolin, "High voltage breakdown study", Technical report ECOM-00394-20, Burlington, MA, 1971.

[37] B. Seznec et al., "Dynamics of microparticles in vacuum breakdown: Crangerg's scenario updated by numerical modeling", Phys. Rev. Accel. and Beams 20, 073501 (2017).

[38] J. Norem et al., "Dark current, breakdown, and magnetic field effects in a multicell, 805MHz cavity", Phys. Rev. Accel. and Beams, vol. 6, 072001 (2003).

[39] M.D. Forno et al., "RF breakdown tests of mm-wave metallic accelerating structures", Phys. Rev. Accel. and Beams, vol. 19, 001301 (2016).

[40] S. Dobert, "Status of very high-gradient cavity tests", Proceedings of Linac2002, Gyeongju, Korea.

[41] W.D. Kilpatrick, "Criterion for vacuum sparking designed to include both rf and dc". Review of Scientific Instruments, 28 (10): 824826.

[42] X. Wu et al., "High-gradient breakdown studies of an X-band Compact Linear Collider prototype structure, Phys. Rev. Accel. and Beams, 20, 052001 (2017).

[43] J. Norem et al., "Effects of surface damage on rf cavity operation", Phys. Rev. ST Accel. Beams 9, 062001 (2006).

[44] A. Anders, "Cathodic arcs - from fractal spots to energetic condensation", ISSN: 1615-5653.

[45] D. Bowring et al., "Analysis of breakdown damage in an 805 MHz pillbox cavity for muon ionization cooling R&D", proceedings of IPAC'13, Shanghai.

[46] A. Grudiev et al., A New Local Field Quantity Describing the High Gradient Limit of Accelerating Structures, Phys.Rev.ST Accel. Beams 12, 102001 (2009).

[47] M.P ande and P. Singh, "Study of RF breakdown and multipacting in accelerator components", DOI: 10.1109/DEIV.2014.6961630.

[48] A. Moretti et al., "$\pi/2$ interleaved cavity developments for the muon collider cooling experiment", Conf.Proc. C980823 (1998).

[49] J. Norem et al., "Dark current, breakdown, and magnetic field effects in a multicell, 805 MHz cavity", Phys. Rev. Spec. Accel. and Beams, vol. 6, 072001 (2003).

[50] R.B. Palmer et al., "RF breakdown with and without external magnetic fields", arXiv:0809.1633v1 [physics.acc-ph], 2008.

[51] Y. Torun et al., "The Mucool Test area and RF program", proceedings of IPAC'10, Kyoto, Japan.

[52] B.T. Freemire et al., Beam Test of a Dielectric Loaded High Pressure RF Cavity for Use in Muon Cooling Channels, proceedings of IPAC'16, Busan, Korea, MOPMW031.

[53] Y. Torun , A. Moretti, "Grid window tests on an 805-MHz pilbox cavity", proceedings of IPAC2015, Richmond, VA, WEPTY054.

[54] D. Bowring et al., "Vacuum RF breakdown of accelerating cavities in multi-tesla magnetic fields", proceedings of IPAC2016, Busan, Korea, MOPMW025.

[55] M. Leonova et al. MICE Cavity Installation and Commissioning/Operation at MTA, WEPTY032, IPAC2015 proceedings, Richmond, VA, USA (2015).

[56] M. Alsharoa, Electromagnetic and Mechanical Design of Gridded Radio-Frequency Cavity Windows, Ph. D thesis, IIT, Chicago, 2004.

[57] G. Kazakevich et al., "Multi-purpose 805 MHz Pillbox RF Cavity for Muon Acceleration Studies", proceedings of PAC11, TUP092.

[58] A. Kochemirovskiy et al., "Breakdown characterization in 805MHz pillbox-like cavity in strong magnetic fields", proceedings of IPAC15, Richmond, USA, WEPTY030.

[59] . Y. Derbenev, R.P. Johnson, "Six-dimensional muon beam cooling using a homogeneous absorber: Concepts, beam dynamics, cooling decrements, and equilibrium emittances in a helical dipole channel", Phys. Rev. ST Accel. Beams 8, 041002.

[60] R.P. Johnson et al., "Muon Beam Helical Cooling Channel Design", Proceedings of COOL13, Murren, Switzerland, June 2013.

[61] B. Freemire et al., "The experimental program for high pressure gas filled radio frequency cavities for muon cooling channels", arXiv:1710.09810v2 [physics.acc-ph], 2017.

[62] Paschen, F. (1889). Annalen der Physik. 273 (5): 6996.

[63] . P. Hanlet et al., "High Pressure RF Cavities in Magnetic Fields", Proceedings of EPAC06, Edinburgh, Scotland, June 2006.

[64] T. Luo et al., Progress on the MICE 201 MHz cavities at LBNL, IPAC15 proceedings, Richmond, VA, USA, 2015, WEPTY046.

[65] Y. Torun et al., "Final commissioning of the MICE RF module prototype with production couplers", proceedings of IPAC2016, MOPMW034.

[66] D .Stratakis, J. Gallardo, R. Palmer, "Effects of external magnetic fields on the operation of high-gradient accelerating structures", Nuclear Instruments and Methods in Physics Research A 620 (2010) 147154.

[67] M. Forno et al., "RF breakdown measurements in electron beam driven 200 GHz copper and copper-silver accelerating structures", Phys. Rev. ST Accel. Beams 19, 111301 (2016).

[68] A. Moretti et al., "Effects of high solenoidal magnetic fields on rf accelerating cavities", Phys. Rev. ST Accel. Beams 10 (2005) 072001.

[69] Y. Torun et al., "Rectangular box cavity tests in magnetic field for muon cooling", proceedings of IPAC'10, Kyoto, Japan, THPEA054.

[70] D. Bowring et al., “RF breakdown of 805 MHz cavities in strong magnetic fields”, proceedings of IPAC2015, Richmond, VA, USA, MOAD2.

[71] T. Koseki et al., ”High-Power conditioning of an RF cavity for high brilliant synchrotron radiation source”, Particle Accelerator Conference, 1997.

[72] D. Bowring et al., “RF design and operation of a modular cavity for muon ionization cooling R&D”, proceedings of IPAC2014, Dresden, Germany, MOOCA02.

[73] D. Bowring et. al, “A Modular Cavity for Muon Ionization Cooling RD”, Proceedings of IPAC2013, Shanghai, China.

[74] R.F. Parodi, “Multipacting”, CERN-2011-007, pp. 447-458.

[75] W. Kaabi et al., “Titanium nitride coating as a multipactor suppressor”, proceedings of IPAC10, Kyoto, Japan, WEPEC002.

[76] V. Baglin et al., ”The secondary electron yield of technical materials and its variation with surface treatments”, European Particle Accelerator Conference Proceedings, Vienna, Austria, 2000

[77] Pimpec, Frederic Le, Paul Scherrer and Mauro Pivi. Summary of SLACS SEY Measurement On Flat Accelerator Wall Materials. (2007).

[78] https://confluence.slac.stanford.edu/display/AdvComp/ACE3P+-+Advanced+Computational+Electromagnetic+Simulation+Suite.

[79] P. Lane et al., “Acoustic breakdown localization in RF cavities”, proceedings of IPAC2015, Richmond, VA, USA, WEPWA067.

[80] . https://www.omega.com/pptst/RTD-2-1PT100K2515.html

[81] . https://ad-esh.fnal.gov/ad/adsp/ADSP-10-0101.pdf

[82] . D. Peterson, Y. Torun, "Fermilab MuCool test area cavity conditioning control using Labview", Fermilab-conf-13-167-AD.

[83] http://www.ni.com/en-us/shop/labview/labview-details.html

[84] https://www-bd.fnal.gov/controls/acnet.html

[85] Subbarao, M. Surya, "Depth from defocus: a spatial domain approach", G. Int J Comput Vision (1994) 13: 271.

[86] R. Palmer et al., "RF breakdown with external magnetic fields in 201 and 805 MHz cavities", Phys. Rev. ST Accel. Beams 12 (2009) 031002.

[87] A. Moretti et al., Phys.Rev. ST Accel. Beams 10 (2005) 072001.

[88] D. Summers, "Beryllium and aluminum cavities operating at high electrical gradients in high magnetic fields", presentation at MuCool RF Workshop III, 2007.

[89] . P.A. Demchenko et al., "Voprosy Atomnoy Nauki i Tekhniki", ser. Tekhika Phys. Experiment., 1984.

[90] A.S. Pohjonen et al., "Dislocation nucleation on a near surface void leading to surface protrusion growth under an external electric field", Journal of Applied Physics 114, 033519 (2013).

[91] V. Zadin et al., "Electrostatic-elastoplastic simulations of copper surface under high electric fields", Phys. Rev. ST Accel. Beams 17, 103501 (2014).

[92] V.G. Karpov, "Electrostatc theory of metal whiskers", Phys. Rev. Applied 1, 044001, 2014.

[93] https://www.wolfram.com/mathematica/.

[94] Richardson, O. W. (2003). "Thermionic Emission from Hot Bodies". Wexford College Press. p. 196. ISBN 978-1-929148-10-3

[95] . W. Smythe, “Static and Dynamic Electricity”, McGraw-Hill Book Company, New York, 1950.

[96] . A. Tollestrup, M. Chung, K. Yonehara, “Handbook for gas filled rf cavity aficionados”, Fermilab TM-2430-APC.

[97] H. E, Burgess and H. Kroemer, “Corrected Values of Fowler-Nordheim Field Emission Functions ”, PhysRev, 90, 515, (1953).

[98] F. Djurabekova et al., “Local changes of work function near rough features on Cu surfaces operated under high external electric field”, Journal of Applied Physics 114, 243302 (2013).

[99] https://cubit.sandia.gov/.

[100] https://confluence.slac.stanford.edu/display/AdvComp/Omega3P.

[101] https://www.paraview.org/.

[102] M. Ferrario et al., “Space charge effects”,CERN Yellow Report CERN-2014-009, pp.331-356.

[103] H. Bethe und J. Ashkin in ”Experimental Nuclear Physics, ed. E. Segr, J. Wiley, New York, 1953, p. 253.

[104] G.J. Lockwood et al., “Calorimetric measurement of electron energy deposition in extended media - theory vs experiment”, SAND79-0414, UC-34a, 1980.

[105] D. Stratakis et al., “Effect of external magnetic fields on the operation of RF cavities”, proceedings of PAC09, Vancouver, Canada, TU5PFP004.

[106] J. V. Beck et al., “Heat conduction using Greens Functions”, Hemisphere Publishing Corp, 1992, pp.236-238.

[107] D. P. Pritzkau et al., "Experimental study of rf pulsed heating on oxygen free electronic copper", Phys. Rev. ST Accel. Beams 5, 112002 (2002).

[108] H.M. Musal, "Laser induced damage in optical materials", NBS special publication 568, 1979.

[109] N.S. Ginzburg et al., "Experiment on pulse heating and surface degradation of a copper cavity powered by powerful 30 GHz free electron maser", Phys. Rev. ST Accel. Beams 14, 041002 (2011).

[110] M.A. Payrebrune, "Experimental Morphology of Lichtenberg Figures", McGill University, Montreal, Canada, 1979.

[111] S.V. Kuzikov, M.E. Plotkin, "Theory of thermal fatigue caused by RF pulsed heating", Int. J. Infrared Milli Waves (2008) 29:298-311.

[112] https://www.nist.gov/pml/stopping-power-range-tables-electrons-protons-and-helium-ions.